

1  
2  
3  
4 **Provenance of Thal Desert sand: focused erosion in the western**  
5  
6  
7  
8  
9  
10 **Himalayan syntaxis and foreland-basin deposition driven by latest**  
11 **Quaternary climate change**  
12  
13  
14  
15  
16  
17

18 Eduardo Garzanti<sup>1\*</sup>, Wendong Liang<sup>1\*</sup>, Sergio Andò<sup>1</sup>, Peter D. Clift<sup>2</sup>, Alberto  
19 Resentini<sup>1</sup>, Pieter Vermeesch<sup>3</sup>, Giovanni Vezzoli<sup>1</sup>.  
20  
21  
22  
23  
24

25 <sup>1</sup> Laboratory for Provenance Studies, Department of Earth and Environmental Sciences,  
26 University of Milano-Bicocca, Milano 20126, Italy

27 <sup>2</sup> Department of Geology and Geophysics, Louisiana State University, Baton Rouge, LA 70803,  
28 USA

29 <sup>3</sup> London Geochronology Centre, Department of Earth Sciences, University College London,  
30 London, C1E 6BT, UK

31 \* Corresponding authors (e-mail: [eduardo.garzanti@unimib.it](mailto:eduardo.garzanti@unimib.it) and [w.liang@campus.unimib.it](mailto:w.liang@campus.unimib.it))  
32  
33

34 **Keywords:** Sand petrography and geochemistry; Detrital-zircon geochronology; Variability of  
35  $\epsilon_{Nd}$  values; Focused erosion; Himalaya-Karakorum; Kohistan Arc; Indus River, Delta, and Fan.  
36  
37

38 **Highlights:**  
39

40  
41 The Thal Desert is an inland archive of Indus sand from the western Himalaya syntaxis  
42

43 Sand stored in the Thal dunefield reveals major detrital supply from the Kohistan arc  
44

45 High variability of  $\epsilon_{Nd}$  values is controlled by minimal changes in monazite content  
46  
47

48 The Thal Desert formed in a dry landscape between the LGM and the wet early Holocene  
49  
50  
51  
52  
53  
54  
55  
56  
57  
58  
59  
60  
61  
62  
63  
64  
65

**Abstract**

1  
2  
3  
4 As a latest Pleistocene repository of Indus River sand at the entry point to the Himalayan foreland  
5  
6 basin, the Thal dune field in northern Pakistan stores crucial information that can be used to  
7  
8 reconstruct the erosional evolution of the Himalayan-Karakorum orogen and the changes in the  
9  
10 foreland-basin landscape that took place between the Last Glacial Maximum and the early Holocene.  
11  
12 This comprehensive provenance study of Thal Desert sand integrates previously existing petrographic,  
13  
14 heavy-mineral, mineral-chemical, isotopic, and geochronological databases with original bulk-  
15  
16 sediment geochemistry, zircon-age, and Nd-isotope data. Dune sand is low in quartz and rich in  
17  
18 feldspars, volcanic, metavolcanic and metabasite grains, contains a very rich transparent heavy-  
19  
20 mineral suite including hypersthene and common zircon grains dated as Late Cretaceous to early  
21  
22 Paleogene, and is characterized by high Mg, Sc, V, Co, Ni, Cu concentrations and by  $\epsilon_{Nd}$  values as  
23  
24 high as -3.5. Together, these data indicate that ~40% of Thal dune sand was supplied by erosion of the  
25  
26 Kohistan arc, a proportion that far exceeds the one assessed for modern Upper Indus sand. Greater  
27  
28 detrital supply from the Kohistan arc indicates notably different conditions of sediment generation,  
29  
30 during a period in which the sediment-transport capacity of the Upper Indus in the dry lowlands was  
31  
32 reduced and volumes of sand were extensively reworked by wind and accumulated in dune fields  
33  
34 across the foreland basin. In the early Holocene, the renewed strength of the South Asian monsoon  
35  
36 and consequently markedly increased water and sediment discharge led to incision of the Thal and  
37  
38 Thar dune fields by the Indus River and its Punjab tributaries draining the Himalayan front directly hit  
39  
40 by heavy monsoonal rains.  
41  
42  
43  
44  
45  
46  
47  
48  
49  
50  
51  
52  
53  
54  
55  
56  
57  
58  
59  
60  
61  
62  
63  
64  
65

## 1. Introduction

The western Himalaya and Karakorum Ranges (in Sanskrit: *hima* = snow, *alayah* = abode; in Uyghur Turkic: *kara* = black, *korum* = gravel) drained by the Indus River provide a spectacular example of an orogenic belt produced by continental collision (Searle, 2013). Ongoing indentation between the Indian and Asian continents since 60-58 Ma (Garzanti et al., 1987; Beck et al., 1995; Hu et al., 2015; Najman et al., 2017) and accelerated rock uplift associated with ultra-rapid exhumation of crystalline basement rocks since the Neogene (Rolland et al., 2001; Zeitler et al., 2001) resulted in extreme relief and erosion rates around the western Himalayan syntaxis (Burbank et al., 1996a; Shroder and Bishop, 2000).

An important contribution to a better understanding of the tectonic growth and erosional evolution of such a complex orogenic region, where geological processes are so intense, is given by provenance analysis of detritus carried by the precursors of the Indus River and stored through time in adjacent sedimentary basins (Critelli et al., 1990; Garzanti et al., 1996; Qayyum et al., 1997; Clift et al., 2001). Numerous studies of Himalayan foreland-basin strata have been devoted to understanding how the Indus River system has formed and evolved (e.g., Cervený et al., 1989; Critelli and Garzanti, 1994; Najman et al., 2003; Downing and Lindsay 2005; Roddaz et al., 2011; Chirouze et al., 2015; Zhuang et al., 2015). Crucial information is stored in the thick sediment pile accumulated in the Indus Fan, cored so far around its southeastern and western edges during Ocean Drilling Program (ODP) Leg 23 in 1972 (Jipa and Kidd, 1974; Mallik, 1978; Suczek and Ingersoll, 1985) and more recently during International Ocean Discovery Program (IODP) Expedition 355 to the Laxmi Basin in 2014 (Clift et al., 2019). Turbidites of proven Himalayan provenance recovered from both ODP Leg 23 and IODP Expedition 355 are however mostly late Miocene or younger in age, and much thus remains to be understood regarding earlier phases of orogenic erosion (Pandey et al., 1996).

26 While plunging deeper in time, paleogeographic reconstructions have to face an increasing number  
1  
27 of unknowns, not only because of subsequent accretion and exhumation of diverse geological units  
3  
48 but also because repeated modifications of the drainage system have occurred even in the recent  
5  
69 past (e.g., [Burbank et al., 1996b](#); [Clift et al., 2012](#)). Moreover, the compositional fingerprints of  
7  
80 ancient siliciclastic strata reflect a distorted image of the lithological structure of source terranes  
9  
10  
11 because of selective diagenetic dissolution of less durable detrital components ([Garzanti, 2019a](#)).

12  
13  
14 The safest way to proceed is to start from the knowledge of the modern sediment-routing system,  
15  
163 where everything is in principle known or knowable ([Garzanti et al., 2005](#); [Alizai et al., 2011, 2016](#);  
17  
18  
194 [East et al., 2015](#); [Zhuang et al., 2018](#)) and to extend that knowledge to the recent and less recent  
20  
213 past ([Clift et al., 2010](#); [Garzanti et al., 2020](#)). In this regard, a particularly interesting repository of  
22  
2336 clastic sediments is represented by the Thal Desert, a small dune field occupying a dry area just  
24  
25  
267 south of the Salt Range, the Pliocene thrust belt representing the front of the Himalayan orogen in  
27  
2838 central northern Pakistan ([Fig. 1](#)).

29  
30  
3139 Thal Desert dunes consist of wind-reworked sediment entirely supplied by the Indus River upstream  
32  
3340 of the orogenic front (henceforth named “Upper Indus”) that provides us with a precise  
34  
35  
3641 compositional signature of detritus dominantly generated by the rapid erosion of the western  
37  
3842 Himalayan syntaxis in the latest Quaternary. The Jhelum River and other large left-bank tributaries  
39  
40  
4143 draining the southern flank of the Himalaya and flowing across the Punjab plains convey their  
42  
4344 sediments to the Indus River only downstream of the Thal Desert, and their contribution to this  
44  
4545 dune field is negligible, as documented by the peculiar compositional signatures of eolian sands  
46  
47  
4846 ([Liang et al., 2019](#)). On the contrary, it is the Thal dunes that, eroded all along the western side of  
49  
507 the desert, contribute sand to the Jhelum River and to the Panjnad River downstream ([Fig. 2](#);  
51  
52  
5348 [Garzanti et al., 2005](#)).

54  
5549 The Upper Indus compositional signature preserved in the Thal dune field is exempt from any  
56  
57  
5850 anthropic modification that had occurred in the region (e.g., Tarbela Dam) and can be compared  
59  
6051 with sand composition in the Lower Indus River, Delta, and Fan. This allows us to calculate the  
61  
62  
63  
64  
65

52 relative amount of sediment shed from diverse upstream sources around the syntaxis *versus* those  
 1  
 2  
 3  
 4  
 5  
 6  
 7  
 8  
 9  
 10  
 11  
 12  
 13  
 14  
 15  
 16  
 17  
 18  
 19  
 20  
 21  
 22  
 23  
 24  
 25  
 26  
 27  
 28  
 29  
 30  
 31  
 32  
 33  
 34  
 35  
 36  
 37  
 38  
 39  
 40  
 41  
 42  
 43  
 44  
 45  
 46  
 47  
 48  
 49  
 50  
 51  
 52  
 53  
 54  
 55  
 56  
 57  
 58  
 59  
 60  
 61  
 62  
 63  
 64  
 65

The aim of the present study is to document in detail the diverse compositional fingerprints of Thal  
 Desert sand by applying multiple analytical techniques, including high-resolution bulk-sediment  
 petrography and geochemistry, heavy minerals and heavy-mineral chemistry, detrital-zircon-  
 geochronology, and Nd isotopes. This integrated dataset is employed to discuss the erosional  
 evolution of the western Himalaya and the sedimentary evolution of the Indus River, Delta and Fan  
 through the latest Cenozoic.

## 2. The Thal Desert

Pakistan is an arid to semi-arid subtropical country including the large Thar Desert (~175,000 km<sup>2</sup>)  
 straddling the political border with India in the southeast (Singh et al., 1990; Enzel et al., 1999;  
 Singhvi and Kar, 2004; Singhvi et al., 2010; East et al., 2015). In the north, the much smaller and  
 much less well studied, 300 km-long and 100 km-wide Thal Desert is located between about 30°  
 and 32°30' N and between about 71° and 72° E (Fig. 1). This triangular-shaped desert occupies the  
 Thal or Sind-Sagar Doab (in Farsi: *do ab* = two waters, or land between two adjacent rivers), the  
 region extending between the course of the Indus River in the west and the Punjab plain in the east,  
 built by the Jhelum, Chenab, Ravi, and Beas-Sutlej Rivers (in Farsi: *punj ab* = five waters, or land  
 of the five rivers).

The Thal Desert, located between the Indus and Jhelum Rivers, is delimited by the Salt Range  
 foothills in the north, whereas the Indus floodplain is bounded by the Sulaiman Range in the west.  
 Exposed in the Salt Range are Neoproterozoic evaporites overlain by a fossiliferous Cambrian to  
 Cenozoic succession (Shah, 1977). The Sulaiman fold-thrust belt includes largely shelfal upper

79 Paleozoic to Eocene strata, Neogene molasse, and deep-water turbidites underlain by ophiolitic  
 80 complexes (Jadoon et al., 1994). The Punjab plains are underlain by up to 450 m of Quaternary  
 81 alluvium and eolian deposits lying over semiconsolidated Cenozoic rocks or directly over  
 82 Precambrian crystalline basement, which crops out in the Kirana Hills straddling the Chenab River  
 83 course and represents the topographic culmination of the NW/SE-trending Delhi-Sargodha ridge  
 84 (Greenman et al., 1967; Kadri, 1995).

## 85 2.1 Geomorphology

86 Different physiographic units can be distinguished in the Thal Desert, which lies at altitudes above  
 87 sea-level decreasing from ~200 m in the north to ~120 m in the south. The piedmont area  
 88 transitional to the Salt Range foothills hosts alluvial fans consisting of detritus reworked and  
 89 deposited during sheet floods, and fining downstream over distances of ~10 km. The desert area to  
 90 the south, covered by low sand dunes or rolling sand plains alternating with narrow valleys of  
 91 cultivable land, is underlain by Quaternary fluvial and eolian deposits more than 350 m-thick in  
 92 southern areas, but even thicker in the central part of the desert (Nickson et al., 2005). The recent  
 93 finding of Mesolithic artefacts at the top of sand dunes indicates that the accumulation of eolian  
 94 sand pre-dates the Holocene (Biagi et al., 2019). The last episode of dune growth may thus be  
 95 related to large sediment fluxes released during glacier retreat following the Last Glacial Maximum  
 96 (LGM) in the latest Pleistocene (Clift and Giosan, 2014).

97 The underlying alluvium mostly consists of laterally continuous bodies of fine to coarse sand, with  
 98 minor gravel and isolated mud lenses. Coarser deposits occur in the north closer to the Salt Range,  
 99 but otherwise the distribution of grain sizes is irregular, largely reflecting original deposition by the  
 100 constantly shifting paleo-Indus and/or adjacent tributaries. The presently active Indus River  
 101 floodplain reaches >20 km in width in the south. The abandoned floodplain is even wider and  
 102 includes areas of higher ground. These bar uplands are actively eroded by the Jhelum River in the

105 northeastern part of the desert, forming up to 10 m-high scarps facing the floodplain ([Greenman et](#)  
 106 [al., 1967](#)).

107

108

109

110

111

112

113

114

115

116

117

118

119

120

121

122

123

124

125

126

127

128

129

130

131

132

133

134

135

136

137

138

139

140

141

142

143

144

145

146

147

148

149

150

151

152

153

154

155

156

157

158

159

160

161

## 2.2. Climate

Summers are very hot in the Thal Desert with average temperatures around 35°C in June to July, dropping to ~10°C in December to January. Average annual temperatures increase from ~24°C in the north and west to ~28°C in the south. Most of the region receives less than 350 mm of rain per year. Annual rainfall progressively decreases from the northern (617 mm on average recorded from 1991 to 2013 in the Mianwali meteorological station; [Shah and Ahmad, 2015](#)) to the southern edges of the desert (150 mm; [Greenman et al., 1967](#)). Today, cold dry winds blow from the north in winter, whereas hot rain-bearing winds blow from the south in summer, with an average speed of several km per hour. Between March and April, hailstorms generated by air turbulence owing to the high temperature difference between the warm surface and the cold upper atmosphere may cause major damage to crop and buildings ([Gosal, 2004](#)). In the summer, dust storms are fostered by unsteady thermal conditions and north/south temperature gradients ([Hussain et al., 2005](#)).

162

163

164

165

166

167

168

169

170

171

172

173

174

175

176

177

178

179

180

181

182

183

184

185

186

187

188

189

## 2.3. Sediment flux

The upper course of the Indus River, sourced in the Tibetan Plateau ([Fig. 2](#)), drains the Ladakh arc and forearc basin together with the northern side of the Himalaya ([Garzanti and Van Haver, 1988](#); [Henderson et al., 2010](#); [Munack et al., 2014](#)). Next, it cuts a deep gorge through the Nanga Parbat crystalline massif and receives detritus from the Karakorum Range and Kohistan Arc ([Gaetani et al., 1990](#); [Treloar et al., 1996](#); [Searle et al., 1999](#); [DiPietro and Pogue, 2004](#); [Pêcher et al., 2008](#); [Burg, 2011](#)). Further downstream, it flows across the Himalayan belt and Potwar Plateau ([Khan et al., 1997a](#)), where it joins with the Kabul River draining the Hindukush Range ([Hildebrand et al., 2001](#)), crosses the Salt Range to eventually reach the lowlands where it flows southward confined between the front of the Sulaiman Range in the west and the Thal Desert in the east ([Fig. 1](#)). After closure of the Chashma Dam at the northwestern corner of the Thal Desert in 1971, and of the

134 Tarbela Dam ~200 km to the north in 1976, most of the sediment carried by the Indus River has  
 135 been trapped in artificial reservoirs. The suspended sediment flux upstream of Tarbela Dam was  
 136 gauged as between  $176\text{--}200 \cdot 10^6$  t/a (Tate and Farquharson, 2000; Ali and De Boer, 2007, 2008)  
 137 and 218, 235, or  $287 \cdot 10^6$  t/a (Rehman et al., 1997), whereas estimates of total sediment delivery to  
 138 the Arabian Sea before the Anthropocene range widely between  $100 \cdot 10^6$  t/a and  $675 \cdot 10^6$  t/a (Ali  
 139 and De Boer, 2007). Suspended load of the Kabul River was measured as  $36.6 \cdot 10^6$  t/a (i.e.  $17 \pm 3\%$   
 140 that of the Indus upstream of Tarbela Dam; Rehman et al., 1997)

141 The Thal Doab aquifer, consisting of Quaternary alluvial and eolian deposits with local mud lenses,  
 142 is recharged rapidly from river water and rainfall. The Indus River and its Punjab tributaries give  
 143 rise to one of the largest irrigation systems in the world, including the Chashma-Jhelum link canal  
 144 supplied with Indus waters and built between 1967 and 1971. A network of dams, barrages and  
 145 canals aims to convert the Thal Desert, where the water table lies between 9 and 0.5 m from ground  
 146 surface, into cultivable land (Shah and Ahmad, 2016; Hussain et al., 2017).

147 The main tributaries joining the Indus River downstream of the Thal Desert drain the Himalayan  
 148 belt (Fig. 2). Since the 1960 Indus Waters Treaty gave rights to the entire flow of the Indus, Jhelum,  
 149 and Chenab Rivers to Pakistan, and of the Ravi, Beas, and Sutlej Rivers to India, all Himalayan  
 150 tributaries of the Punjab have been dammed and linked by canals to irrigate the arid plains and  
 151 compensate for lost waters in eastern Pakistan. Water discharge dropped sharply from  $\geq 100$  km<sup>3</sup>/a  
 152 to  $\leq 60$  km<sup>3</sup>/a, and flow in the Ravi and Sutlej Rivers ceased except during monsoon floods. The  
 153 Mangla Dam, completed in 1967, has reduced sediment load of the Jhelum River from  $45 \cdot 10^6$  t/a  
 154 to  $< 0.5 \cdot 10^6$  t/a (Milliman et al., 1984; Meadows and Meadows, 1999; Giosan et al., 2006a). The  
 155 main right-bank (western) tributaries of the Indus River draining the Sulaiman Ranges are the  
 156 Gomal River (basin area 36,000 km<sup>2</sup>), characterized by extreme concentration of suspended solids  
 157 (42 g/l) and high sediment load ( $30 \cdot 10^6$  t/a), and the Kurram River ( $3 \cdot 10^6$  t/a; Rehman et al.,  
 158 1997). Other rivers are minor and mostly flow during flash floods.

### 3. Methods



161  
162  
2  
3  
163  
4  
5  
164  
6  
7  
165  
8  
9  
10  
166  
11  
12  
13  
167  
14  
15  
168  
16  
17  
169  
18  
19  
20  
170  
21  
22  
23  
24  
25  
26  
27  
28  
29  
30  
175  
31  
32  
176  
33  
34  
35  
36  
37  
38  
39  
179  
40  
41  
42  
43  
44  
45  
46  
47  
48  
49  
183  
50  
51  
52  
53  
54  
55  
56  
57  
58  
59  
60  
61  
62  
63  
64  
65

This study, focusing on fine-grained sand of eolian dunes sampled in February 2001 from the Thal Desert, provides geochemical and geochronological data on sand collected between 2001 and 2011 from active river bars in tributaries each draining a different geological domain around the western Himalayan syntaxis and on Upper Indus sand collected upstream of the Thal Desert (sampling locations indicated in [Appendix Table A1](#) and *Google Earth* file [Thal & Sources.kmz](#)). Geochemical data are also presented for sand from the Jhelum, Chenab, Ravi and Sutlej Rivers, and from the Lower Indus River and Delta. These new data integrate the extensive petrographic, heavy-mineral, and geochemical datasets built with the same analytical methods in the last 15 years ([Clift et al., 2002, 2010](#); [Garzanti et al., 2005](#); [Liang et al., 2019](#)).

### 3.1. Sand petrography and heavy minerals

A quartered aliquot of each bulk-sand sample of Thal Desert dunes was impregnated with araldite epoxy, cut into a standard thin section stained with alizarine red to distinguish dolomite and calcite, and analysed by counting 400 points by the Gazzi-Dickinson method ([Ingersoll et al., 1984](#)). Sand classification was based on the relative abundance of the three main groups of components (Q = quartz; F = feldspars; L = lithic fragments), considered where exceeding 10%QFL. According to standard use, the less abundant component goes first, the more abundant last (e.g., in a litho-feldspatho-quartzose sand  $Q > F > L > 10\%QFL$ ; [Garzanti, 2019b](#)). Metamorphic grains were classified by protolith composition and metamorphic rank; average rank of rock fragments in each sample was expressed by the metamorphic indices MI and MI\*, ranging respectively from 0 (detritus from sedimentary and volcanic rocks) or 100 (detritus from very low-grade metamorphic rocks) to 500 (detritus from high-grade metamorphic rocks; [Garzanti and Vezzoli, 2003](#)). Median grain size was determined in thin section by ranking the samples from coarsest to finest followed by visual comparison with in-house standards sieved at 0.25  $\phi$  interval.

187 Heavy minerals were separated in sodium polytungstate (density  $\sim 2.90 \text{ g/cm}^3$ ), using the 63-250  $\mu\text{m}$   
 188 fraction obtained by sieving and treated with oxalic and acetic acids. Analyses were carried out first  
 189 by counting 200-225 transparent heavy minerals on grain mounts by the area method ([Mange and](#)  
 190 [Maurer, 1992](#)). Next, in order to obtain an accurate estimate of volume percentages of each dense  
 191 detrital component ([Galehouse, 1971](#)), between 275 and 1300 dense grains per sample (700 on  
 192 average) were point-counted on a polished thin section by semi-automated analysis with a Raman  
 193 spectrometer ([Andò and Garzanti, 2014](#); [Lünsdorf et al., 2019](#)).

194 Transparent heavy-mineral assemblages, called for brevity “tHM suites” throughout the text, are  
 195 defined as the spectrum of detrital extrabasinal minerals with density  $> 2.90 \text{ g/cm}^3$  identifiable under  
 196 a transmitted-light microscope. According to the volume percentage of transparent heavy minerals  
 197 in the sample (tHMC), tHM suites are defined as “poor” (tHMC  $< 1$ ), “moderately poor” ( $1 \leq$   
 198 tHMC  $< 2$ ), “moderately rich” ( $2 \leq$  tHMC  $< 5$ ), “rich” ( $5 \leq$  tHMC  $< 10$ ), “very-rich” ( $10 \leq$  tHMC  $<$   
 199  $20$ ), or “extremely rich” ( $20 \leq$  tHMC  $< 50$ ) ([Garzanti and Andò, 2007, 2019](#)). The sum of zircon,  
 200 tourmaline and rutile over total transparent heavy minerals (ZTR index of [Hubert, 1962](#)) estimates  
 201 the durability of the tHM suite (i.e., extent of recycling; [Garzanti, 2017](#)). Detrital components are  
 202 listed in order of abundance (high to low) throughout the text. The complete petrographic and  
 203 heavy-mineral datasets are provided in [Appendix Tables A2, A3, A4, and A5](#). Further information  
 204 on the chemical composition of detrital amphiboles, garnets, epidote-group minerals, and pyroxenes  
 205 is provided in [Liang et al. \(2019\)](#).

### 207 *3.2. U-Pb zircon geochronology*

208 Detrital zircons were identified by Automated Phase Mapping ([Vermeesch et al., 2017](#)) with a  
 209 Renishaw inVia<sup>TM</sup> Raman microscope on the heavy-mineral separates of 14 samples (three from the  
 210 Thal Desert, two from the Upper Indus, and nine from diverse end-member sources). U-Pb zircon  
 211 ages were determined at the London Geochronology Centre using an Agilent 7700x LA-ICP-MS  
 212 (laser ablation-inductively coupled plasma-mass spectrometry) system, employing a NewWave  
 213

214 NWR193 Excimer Laser operated at 10 Hz with a 20  $\mu\text{m}$  spot size and  $\sim 2.5 \text{ J/cm}^2$  fluence. No  
 215 cathodo-luminescence imaging was done, and the laser spot was always placed “blindly” in the  
 216 middle of zircon grains in order to treat all samples equally and avoid bias in intersample  
 217 comparison (“blind-dating approach” as discussed in [Garzanti et al., 2018](#)). Data reduction was  
 218 performed using GLITTER 4.4.2 software ([Griffin et al., 2008](#)). We used  $^{206}\text{Pb}/^{238}\text{U}$  and  $^{207}\text{Pb}/^{206}\text{Pb}$   
 219 ages for zircons younger and older than 1100 Ma, respectively. No common Pb correction was  
 220 applied. Grains with  $> +5 / -15\%$  age discordance were discarded, and 1392 concordant ages were  
 221 obtained overall. The full geochronological dataset is provided in [Appendix B](#).

### 222 3.3. Bulk chemistry and Nd isotopes

223 Chemical analyses of 23 sand samples (four from the Thal Desert, eight from diverse end-member  
 224 sources, three from the Upper Indus, four from Punjab tributaries, and four from the Lower Indus  
 225 and Delta) were carried out at Bureau Veritas Mineral Laboratories (Vancouver) on a split aliquot of  
 226 the 63-2000  $\mu\text{m}$  fraction obtained by wet sieving. Major oxides were determined by ICP-ES and  
 227 trace elements by ICP-MS, following a lithium metaborate/tetraborate fusion and nitric acid  
 228 digestion. A separate split was digested in aqua regia and analysed for Mo, Cu, Ag, Au, Zn, Cd, Hg,  
 229 Tl, Pb, As, Sb, Bi and Se, but the concentration of these elements is generally underestimated  
 230 because of incomplete leaching of refractory minerals. For further information on adopted  
 231 procedures, geostandards used, and precision for various elements see <http://acmelab.com> (code  
 232 LF200). The geochemical dataset is provided in [Appendix Table A6](#).

233 For each of the four Thal Desert samples, several grams of the bulk sand were powdered to ensure a  
 234 good average composition. Samples were then dissolved, and the Nd separated using standard  
 235 column extraction techniques. Nd isotopic compositions were determined on VG354 mass  
 236 spectrometer at Woods Hole Oceanographic Institution.  $^{143}\text{Nd}/^{144}\text{Nd}$  values were normalized to  
 237  $^{146}\text{Nd}/^{144}\text{Nd} = 0.7219$  and relative to 0.511847 for the La Jolla standard. We calculated the parameter  
 238  $\epsilon_{\text{Nd}}$  ([DePaolo and Wasserburg, 1976](#)) using a  $^{143}\text{Nd}/^{144}\text{Nd}$  value of 0.512638 for the Chondritic

241 Uniform Reservoir ([Hamilton et al., 1983](#)). Original data and a compilation of literature data are  
 242 provided in [Appendix Tables A7](#) and [A8](#).

243

### 244 3.4. Statistical/graphical displays

245  
 246 Zircon-age data, plotted using the *provenance* package of [Vermeesch et al. \(2016\)](#), are visualized as  
 247 kernel density estimates (KDE) with a nominal bandwidth of 40 Ma ([Vermeesch, 2012](#)). Statistical  
 248 techniques used to illustrate our datasets also include the compositional biplot ([Gabriel, 1971](#)) and  
 249 multidimensional scaling (MDS; [Vermeesch, 2013](#); [Vermeesch and Garzanti, 2015](#)).

250 The biplot, drawn using *CoDaPack* software by [Comas-Cufí and Thió-Henestrosa \(2011\)](#), allows  
 251 discrimination among multivariate observations (points) while shedding light on the mutual  
 252 relationships among variables (rays). The length of each ray is proportional to the variance of the  
 253 corresponding variable in the dataset. If the angle between two rays is close to 0°, 90° or 180°, then  
 254 the corresponding variables are directly correlated, uncorrelated, or inversely correlated,  
 255 respectively.

256 MDS produces a map of points in which the distance among samples is approximately proportional  
 257 to the Kolmogorov-Smirnov dissimilarity of their compositional or chronological signatures. Closest  
 258 and second-closest neighbours are linked by solid and dashed lines, respectively, and the goodness  
 259 of fit is evaluated using the “stress” value of the configuration (0.2 = poor; 0.1 = fair; 0.05 = good;  
 260 [Kruskal, 1964](#); table 1 in [Vermeesch, 2013](#); [2018](#)).

261

## 262 4. Compositional fingerprints of Thal Desert sand

263

### 264 4.1. Petrography and heavy minerals

265  
 266 Three Thal dune samples are litho-feldspatho-quartzose sands and one is quartzo-feldspatho-lithic  
 267 (average composition Q37 F34 L29; [Fig. 3A](#)). Quartz is mostly monocrystalline. K-feldspar and  
 268 plagioclase occur in subequal amounts. The rock-fragment population includes metasedimentary  
 269 (paragneiss, schist, slate, calcschist, phyllite, metasandstone), metabasite (prasinite, chloritoschist,  
 270

271  
 272  
 273  
 274  
 275

270 amphibolite), carbonate (limestone, dolostone), other sedimentary (shale, siltstone, minor chert),  
 271 granitoid, felsic to mafic volcanic and metavolcanic, and minor ultramafic (serpentineschist, cellular  
 272 serpentinite) grains (MI 209-290, MI\* 273-317). A few muscovite and biotite flakes are present.  
 273 The very rich tHM suite is dominated by mainly blue-green amphiboles associated with epidote,  
 274 garnet, green to colourless clinopyroxene, and hypersthene. Titanite, staurolite, kyanite, zircon,  
 275 tourmaline, rutile, sillimanite, olivine, and chloritoid also occur ( $ZTR \leq 4$ ). Detrital amphiboles  
 276 include mainly hornblende, subordinate pargasite, actinolite, hastingsite, and minor tschermakite.  
 277 Detrital garnet is mostly almandine with minor grossular, pyrope, spessartine, and andradite (mostly  
 278 Bi grains with minor Ci, Bii, A, and a few D grains according to the classification of [Mange and](#)  
 279 [Morton, 2007](#)). Epidote-group minerals are mainly clinozoisite and epidote. Detrital pyroxene is  
 280 mainly diopside with common orthopyroxene and minor augite ([Liang et al., 2019](#)).

#### 282 4.2. Detrital-zircon geochronology

283  
 284 The three Thal samples analysed yielded 103 concordant ages overall, including early Miocene (22  
 285 Ma; n=3), Eocene (38-53 Ma; n=15), latest Cretaceous/Paleocene (61-84 Ma; n=19), mid-  
 286 Cretaceous (98-110 Ma; n=10), Orosirian (1.82-1.87 Ga; n=15), and earliest Paleoproterozoic  
 287 clusters (2.32-2.39 Ga; n=4). Other ages are spread in the Mesozoic (n=6), Paleozoic (n=6),  
 288 Neoproterozoic (n=13), late Mesoproterozoic (n=4), Paleoproterozoic (n=4), and earliest  
 289 Paleoproterozoic to late Neoproterozoic (n=4).

#### 290 4.3. Sand geochemistry

291  
 292 Despite their homogenous provenance, local selective-entrainment effects account for a difference  
 293 in heavy-mineral concentration by a factor of two in our Thal Desert sand samples. This  
 294 corresponds to a difference by factors of between 2.5 and 5 of elements preferentially hosted in the  
 295 densest rock-forming minerals such as opaque Fe-Ti-Cr oxides, monazite, zircon, and to a lesser  
 296 extent rutile and garnet (i.e., Fe, Ti, Mn, Y, REE, Th, U, Zr, Hf, V, Nb, Ta and Cr). The europium  
 297 anomaly  $Eu/Eu^*$  varies from 0.74 in the less heavy-mineral rich sample S1474 (Zr 106 ppm) to 0.46  
 298

299 in the sample richest in heavy minerals S1470 (Zr 524 ppm) and is 0.62-0.64 in the other two  
 300 samples S1462 and S1463 (Zr 195-213 ppm). The composition of Thal Desert sand compares  
 301 remarkably well with the Upper Continental Crust standard (UCC; [Taylor and McLennan, 1995](#);  
 302 [Rudnick and Gao, 2003](#)), but with twice as much Th and Cr, ~50% more Ca, Y, REE, and Zr, and  
 303 ~50% less K, Rb, and Ba, differences all largely accounted for by the strong local concentration of  
 304 densest minerals by selective-entrainment effects.

#### 305 4.4. Nd isotopes

306 Neodymium isotope ratios range widely in the studied Thal Desert sand samples. All four samples  
 307 are fine sands, but coarser samples characterized by higher heavy-mineral concentration and more  
 308 volcanic, metavolcanic, and metabasite rock fragments have less negative  $\epsilon_{Nd}$  (2.0-2.2  $\phi$ ; tHMC 18-  
 309 19;  $\epsilon_{Nd}$  -3.5 and -8.7) than finer-grained samples (2.3-2.7  $\phi$ ; tHMC 10-15;  $\epsilon_{Nd}$  -10.9 and -13.2).  
 310 Because their bulk-sediment mineralogy is homogeneous overall, indicating notably constant  
 311 provenance, such a marked variability is dominantly controlled by local factors including grain size  
 312 and concentration of densest minerals by selective entrainment of less dense grains by wind  
 313 deflation.

## 314 5. Compositional fingerprints of sand sources

315 All geological domains drained by the Upper Indus, including the Ladakh and Kohistan arcs, the  
 316 Karakorum and Hindukush Ranges, the Himalayan belt, and the Nanga Parbat massif are detrital  
 317 sources of Thal Desert dunes ([Fig. 4](#)). The mineralogical signatures of modern sand carried by  
 318 tributaries draining each geological domain, summarized here below, are illustrated in detail in  
 319 [Garzanti et al. \(2005\)](#) and [Liang et al. \(2019\)](#).

### 320 5.1. Petrography and heavy minerals

327 Indus tributaries draining the Ladakh arc carry quartzo-feldspathic to feldspar-rich feldspatho-  
 328 quartzose plutoniclastic sand with a rich to very rich tHM suite dominated by amphibole (mostly  
 329 hornblende), with minor epidote, titanite, apatite, and clinopyroxene (mainly diopside).  
 330 Hypersthene or allanite are found locally.

331 River sand from the Kohistan arc ranges in composition from feldspatho-quartzo-lithic to litho-  
 332 quartzo-feldspathic metamorphiclastic with common prasinite and epidote-amphibolite grains and a  
 333 very rich to extremely rich tHM suite dominated by amphibole (mainly hornblende or pargasite  
 334 associated with actinolite or hastingsite and rare tschermakite). Epidote-group minerals (mostly  
 335 clinozoisite) and pyroxene (diopside, pigeonite, augite, and hypersthene) are common, whereas  
 336 mostly Ca-rich or Mg-rich garnet is rare.

337 Indus tributaries draining the Karakorum carry sand ranging in composition from quartzo-  
 338 feldspatho-lithic sedimentaelastic (North Karakorum) to quartzo-feldspathic plutoniclastic (Central  
 339 Karakorum) or litho-feldspatho-quartzose metamorphiclastic with marble grains (South  
 340 Karakorum). Mainly moderately rich tHM suites include mostly amphibole (mainly hornblende  
 341 with pargasite, hastingsite, or actinolite), epidote-group minerals (epidote, clinozoisite, and  
 342 allanite), mostly Bi-type garnet, titanite, mostly diopsidic clinopyroxene, and minor kyanite,  
 343 staurolite and sillimanite. A similar composition characterizes feldspatho-quartzo-lithic  
 344 sedimentaelastic sand of the Kabul River upstream of the Swat confluence.

345 Detritus from the Greater Himalaya, contributed by the Zanskar River and by minor rivers in  
 346 northern Pakistan, is litho-feldspatho-quartzose metamorphiclastic with a moderately rich tHM suite  
 347 including amphibole (pargasite and hornblende with minor hastingsite), mostly Bi-type garnet,  
 348 fibrolitic sillimanite, kyanite, epidote-group minerals (epidote, clinozoisite, minor allanite), and  
 349 pyroxene (diopside, augite, and locally hypersthene).

350 Sand supplied by tributaries draining the Nanga Parbat massif is mainly feldspar-rich feldspatho-  
 351 quartzose with an up to very rich tHM suite dominated by amphibole (mainly hornblende with

352  
353  
354  
355  
356  
357  
358  
359  
360  
361  
362  
363  
364  
365

352 common tschermakite and minor pargasite). Garnet (mainly Ci and minor Bii types), pyroxene  
 353 (diopside with rare augite), epidote, clinozoisite, and sillimanite occur.

354 The Soan River, mostly recycling Cenozoic foreland-basin strata, carries feldspatho-litho-quartzose  
 355 sedimentaelastic sand with a moderately rich, epidote-dominated tHM suite with garnet,  
 356 hornblende, and tourmaline.

357 As far as REE-rich minerals are concerned, allanite is invariably common (2-3 tHM%) in sand  
 358 carried by the Hushe, Braldu, Hispar, and Hunza Rivers draining the Karakorum Range.  
 359 Karakorum-derived sand contains two to five times more allanite than sand shed by the Greater  
 360 Himalaya and Nanga Parbat, and one order of magnitude more allanite than sand shed by the  
 361 Ladakh and Kohistan arcs. Monazite is rarer and was detected in sand derived from the Karakorum  
 362 and in Zanskar sand.

## 364 5.2. Detrital-zircon geochronology

### 366 5.2.1. Ladakh and Kohistan arcs

367 Modern river sand derived from the Transhimalayan arcs yielded simple zircon-age spectra (Fig. 5),  
 368 reflecting peaks of magmatic activity in the Ladakh (50-70 Ma, [Weinberg and Dunlap, 2000](#); 58-60  
 369 Ma, [Singh et al., 2007](#); 50-67 Ma, [Ravikant et al., 2009](#); 47-58 Ma, [St-Onge et al., 2010](#)) and  
 370 Kohistan arc (82-99 Ma, [Schaltegger et al., 2002](#); 42-85 Ma, [Jagoutz et al., 2009](#)).

371 Sand of the Domkar stream draining the Ladakh arc shows a dominant Eocene-Paleocene peak (49-  
 372 65 Ma; n=34) with a younger age at 46 Ma and a Late Cretaceous cluster (78-87 Ma; n=7). Kandia  
 373 and Swat sands derived from the Kohistan arc display a Late Cretaceous peak (73-95 Ma; n=54)  
 374 with two younger ages at 56 Ma and 69 Ma and three older ages at 716 Ma, 1086 Ma, and 2545 Ma.  
 375 A younger spectrum, very similar to Domkar sand, was obtained by [Zhuang et al. \(2018\)](#) from Dir  
 376 River sand, which displays a prominent Eocene-Paleocene peak (43-65 Ma; n=76), several  
 377 Cretaceous aged grains (76-118 Ma; n=14), and a few older grains (196-821 Ma; n= 4).

### 380 5.2.2. Karakorum Range



381 The four samples of Karakorum river sand yielded 576 concordant ages overall (Fig. 5), including  
 382  
 383 prominent peaks in the early Miocene/latest Oligocene (16-26 Ma; n=19), late Eocene (35-43 Ma;  
 384 n=51), Paleocene (57-66 Ma; n=10), and mid-Cretaceous (99-130 Ma; n=184), with sparse ages in  
 385 the Rupelian (31 Ma), early Eocene (48 Ma), Campanian (73 Ma and 76 Ma), and Turonian (91-92  
 386 Ma; n=4). Older ages are irregularly spread between the earliest Cretaceous and the Ordovician  
 387 (134-484 Ma; n=47), form a broad cluster ranging between the Cambrian and the latest  
 388 Mesoproterozoic (490-1026 Ma; n=201), are again sparsely spread through the Mesoproterozoic  
 389 and Paleoproterozoic (1050-2448 Ma; n=34), and form a cluster straddling the Proterozoic/Archean  
 390 boundary (2468-2535 Ma; n=15) with a few older Archean grains (2553-3568 Ma; n=7). Most ages  
 391 from our Upper Hunza River sample combined with that from the same site analysed by Zhuang et  
 392 al. (2018) outline two dominant young clusters at 48-74 Ma (n=51) and 101-122 Ma (n=81) with  
 393 other sparse ages at 44 Ma, 82-93 Ma (n=4), 126-130 Ma (n=3), and 239 Ma. All older ages (377-  
 394 893 Ma; n=7) are from our sample.

395 Zircon ages in Karakorum-derived sand correspond closely with the ages of igneous and  
 396 metamorphic rocks exposed in the range. The early Miocene peak found in zircons from Hushe (19-  
 397 26 Ma; n=9/55) and Braldu (16-25 Ma; n=10/124) sands reflects the age of high-grade  
 398 metamorphism, crustal melting and emplacement of the Baltoro granite (21-26 Ma; Schärer, et al.,  
 399 1990; 13-26 Ma, Searle et al., 2010; 15-26 Ma, Mahar et al., 2014). The Eocene peak found in  
 400 Hispar sand (35-42 Ma; n=48/359) reflects the age of upper-amphibolite-facies metamorphism in  
 401 the South Karakorum belt (44-64 Ma, Fraser et al., 2001; 37-55 Ma, Rolland et al., 2001). The  
 402 Lower Cretaceous peak is prominent in all samples (100-125 Ma; n=120/359 in Hispar sand,  
 403 n=29/124 in Braldu sand, and n=15/55 in Hushe sand) and reflects the emplacement age of the  
 404 central Karakorum batholith (95-110 Ma, Debon et al., 1987; 95-115 Ma, Crawford and Searle,  
 405 1992). Whereas earliest Cretaceous to Silurian zircons are few and possibly recycled from  
 406 sedimentary and low-grade metasedimentary rocks, ages between the Ordovician and the latest  
 407 Mesoproterozoic are common in all samples, and reflect the Pan-African orogenic event widely

408 detected in the Himalayas ([Garzanti et al., 1986](#); [DeCelles et al., 2000](#); [Miller et al., 2001](#); [Gehrels](#)  
 409 [et al., 2003](#)). Older zircons, mostly represented in Hispar and Braldu sands with ages clustering  
 410 around 2.5 Ga, may be largely recycled from sedimentary and metasedimentary units.

### 411 5.2.3. Hindukush Range and Kabul River

412 In a sand sample analysed by [Zhuang et al. \(2018\)](#) from the Chitral-Kunar River, which drains both  
 413 Hindukush and Karakorum Ranges, half of the zircon ages are spread between the Cambrian and  
 414 the Tonian (486-976 Ma; n=61/126), whereas minor clusters are documented at 62-70 Ma (n=8),  
 415 102-114 Ma (n=16), 1851-1891 Ma (n=6), and 2467-2515 Ma (n=4).

416 The zircon age-spectrum obtained by [Zhuang et al. \(2018\)](#) on a sand sample from the Kabul River  
 417 downstream is notably different, with a younger peak at 31-38 Ma (n=12), a Cretaceous cluster at  
 418 75-113 Ma (n=39), a small peak at 191-204 Ma (n=10) – a Cimmerian age characteristic of  
 419 Hindukush igneous and metamorphic rocks ([Hildebrand et al., 2001](#)) –, a broad Cambrian-Tonian  
 420 spread (495-986 Ma; n=28), and a few Orosirian (1841-1847 Ma; n=3) and older ages (2074-2592  
 421 Ma; n=7). Ages were recorded also at 46-71 Ma (n=3), 123-179 Ma (n=7), 211-482 Ma (n=7), and  
 422 1011-1419 Ma (n=4).

### 423 5.2.4. Nanga Parbat

424 The Astor River sand derived from the Nanga Parbat massif yielded a unimodal earliest Statherian-  
 425 Orosirian peak at 1787-1941 Ma (n=98) consistent with the age of the gneissic basement (~1850  
 426 Ma; [Zeitler et al., 1993](#); [Whittington et al., 2000](#); [Schneider et al., 2001](#)). This major episode of  
 427 crustal growth is widely recognized in the Lesser Himalaya (e.g., [Miller et al., 2000](#); [Singh et al.,](#)  
 428 [2009](#); [Gehrels et al., 2011](#); “Ulleri-Wangtu” event of [Prasad et al., 2011](#)). Older Paleoproterozoic  
 429 ages (1964-2494 Ma; n=14) and one latest Carboniferous age also occur ([Fig. 5](#)). No grain younger  
 430 than 47 Ma was found, and the few early Eocene to Late Cretaceous zircons (47-88 Ma; n=7) may  
 431 be derived from the Ladakh arc drained in the upper course.

### 432 5.2.5. Greater Himalaya

438  
 439 Nandihar River sand derived from the Greater Himalaya in Pakistan yielded mainly early-middle  
 440 Neoproterozoic ages (740-989 Ma; n=20), with sparse Carboniferous to Ediacaran ages (345-547  
 441 Ma; n=11) and a few younger (105 Ma and 216 Ma) and older grains (1700 Ma, 1803 Ma, and 2400  
 442 Ma) (Fig. 5). A similar spectrum was obtained by Jonell et al. (2017a) from Zanskar River sand,  
 443 with better defined Cryogenian-Tonian (751-856 Ma; n= 44) and Carboniferous-Ordovician clusters  
 444 (337-476 Ma; n=27), and sparse younger (58 Ma, 246 Ma, and 301 Ma) and older ages (1040-3117  
 445 Ma; n=17)

### 446 5.3. Sand geochemistry

447 The provenance-discrimination power of bulk-sediment geochemistry is limited, because the same  
 448 chemical elements are hosted in different minerals found in a wide range of rocks and because  
 449 element concentrations are severely affected by grain-size and hydraulic-sorting effects (Garzanti,  
 450 2016). Nevertheless, some remarkable differences are noted among sands derived from different  
 451 geological domains surrounding the western Himalayan syntaxis (Fig. 6A).

452 Sand derived from the Kohistan arc is enriched 1.5-2 times in Fe, Mg, Ca, Sc, Ti, V and Cr  
 453 relatively to the UCC standard, and depleted by ~50% or more in K, Rb, Ba, LREE, Th, U, Zr, Hf,  
 454 Nb, Ta and Sn, reflecting the mainly intermediate to mafic character of calc-alkaline magmatic  
 455 source-rocks. Domkar sand derived from the Ladakh arc is notably different and much closer to the  
 456 UCC standard, although depleted by 50% or more in Mg, Nb, Ta, Cr and Co, which reflects the  
 457 more felsic character of the largely granodioritic calc-alkaline source rocks.

458 Hispar River sand derived from the Central and South Karakorum is enriched by factors of 2-3  
 459 relative to the UCC standard in REE, U, Zr and Hf, and by factors of 5-10 in Th, W and As. This  
 460 may be ascribed to selective entrainment of less dense detrital components in the river channel and  
 461 consequent concentration of densest minerals probably including monazite and scheelite. Elements  
 462 most depleted relative to the UCC are Mg, V, Co and Ni.

465 Himalayan-derived sand displays overall homogeneous character. Most elements – excepting Si,  
 1  
 466 Ca, LREE and Th – are slightly depleted relatively to the UCC standard, which is typical of sand  
 3  
 467 including detritus recycled from sedimentary and metasedimentary rocks. Large differences in Ca  
 5  
 468 and to a lesser extent Sr reflect varying amounts of carbonate detritus, which is particularly  
 8  
 469 abundant in sand of the Zanskar River cutting across the Tethys Himalaya zone (Blöthe et al., 2014;  
 10  
 470 Jonell et al., 2017a). Zanskar and Astor sands are the closest to UCC composition: Zanskar sand is  
 13  
 471 markedly depleted in V, Cr, Co and Ni, and Astor sand slight enriched in Rb and Th and markedly  
 15  
 472 depleted in Nb, Ta and Ni. Soan sand is more depleted (by ~50%) in Na and other mobile alkalic  
 17  
 473 and alkaline-earth metals excepting Ca and Sr, suggesting weathering inherited from recycling of  
 20  
 474 Cenozoic Himalayan molasse exposed within and around the Potwar Plateau (Garzanti and  
 22  
 475 Resentini, 2016).

#### 476 5.4. Nd isotopes

477 The  $^{143}\text{Nd}/^{144}\text{Nd}$  isotopic ratio provides a useful means to discriminate among different source-rock  
 29  
 478 domains in the Himalayan-Karakorum orogen (e.g., Clift et al., 2002; Chirouze et al., 2015; Zhuang  
 31  
 479 et al., 2015) (Appendix Tables A7 and A8). Juvenile values characterize the Ladakh and Kohistan  
 33  
 480 arcs ( $\epsilon_{\text{Nd}}$  mostly from 0 to +8; Petterson et al., 1993; Khan et al., 1997b; Rolland et al., 2002;  
 35  
 481 Jagoutz et al., 2019), whereas the most radiogenic values identify the gneissic basement of the  
 37  
 482 Nanga Parbat massif ( $\epsilon_{\text{Nd}}$  from -18 to -30; Whittington et al., 1999; Argles et al., 2003). Values are  
 39  
 483 very negative also in Lesser Himalayan rocks ( $\epsilon_{\text{Nd}}$  mainly from -19 to -26), but less negative for the  
 41  
 484 Tethyan and Greater Himalaya ( $\epsilon_{\text{Nd}}$  mainly from -13 to -20; Parrish and Hodges, 1996; Whittington  
 43  
 485 et al., 1999; Ahmad et al., 2000). Values intermediate between the Himalayan belt and  
 45  
 486 Transhimalayan arcs characterize the Karakorum ( $\epsilon_{\text{Nd}}$  mainly from -6 to -12; Schärer et al., 1990;  
 47  
 487 Mahéo et al., 2009).

## 6. Compositional fingerprints of Indus sand from the mountains to the deep sea

### 6.1. Petrography and heavy minerals

The modern Upper Indus River carries feldspatho-litho-quartzose sand to the foreland basin, including a variety of sedimentary and metamorphic rock fragments, and a rich hornblende-dominated tHM suite with epidote, garnet, and minor clinopyroxene, hypersthene, staurolite, titanite, kyanite, and sillimanite (Fig. 3B). In the mid-Miocene, the Burdigalian-Langhian (18-14 Ma) Kamli Formation, exposed in the Potwar Plateau and inferred to have been largely deposited by a paleo-Indus River, contains feldspatho-quartzo-lithic sandstones including sedimentary as well as volcanic, metavolcanic, and metabasite rock fragments (Najman et al., 2003). This may represent the time when a drainage system similar to the present one was first established. The existence and compositional fingerprints of a paleo-Indus at older times remain loosely constrained (Clift et al., 2000; Roddaz et al., 2011; Zhuang et al., 2015).

Himalayan tributaries in the Punjab region carry feldspatho-litho-quartzose sand with varied sedimentary and metamorphic rock fragments and mainly moderately rich epidote-amphibole-garnet tHM suites including dravitic tourmaline, kyanite, fibrolitic sillimanite, and staurolite (Fig. 3C). Right-bank tributaries draining the sedimentary succession of the Sulaiman-Kirthar Ranges – as well as Indian basement rocks of the Spinghar Crystalline (Badhsah et al., 2000) and the Waziristan, Zhob and Muslimbagh ophiolites (Gnos et al., 1997) – carry feldspatho-quartzo-lithic sedimentary to lithic carbonaticlastic sand yielding very poor to moderately rich tHM suites with epidote, amphibole, clinopyroxene, and garnet. Minor ophiolitic detritus includes serpentinite grains, enstatite, olivine, and Cr-spinel.

The Lower Indus River carries feldspatho-litho-quartzose sand with mostly sedimentary and metamorphic rock fragments, and a rich amphibole-epidote-garnet tHM suite with minor clinopyroxene, titanite, tourmaline, kyanite, staurolite, hypersthene, and sillimanite (Fig. 3D). LGM to Holocene Delta sand has a very similar composition (Clift et al., 2010), with differences mostly

518 accounted for by hydraulic-sorting effects (more micas, less heavy minerals, and especially less  
 519 high-density garnet; [Fig. 3E](#)).

520 Plio-Quaternary Indus Fan turbidites reported from ODP Sites 221 and 222 are more feldspathic  
 521 (Q49 F31 L20; [Suczek and Ingersoll, 1985](#)) than modern Lower Indus River (Q48 F21 L31;  
 522 [Garzanti et al., 2005](#)) and LGM to Holocene Delta sands (Q49 F26 L25; [Clift et al., 2010](#)). Recent  
 523 data from upper Miocene to lower Pleistocene Indus Fan turbidites (Q52 F24 L25; [Garzanti et al.,](#)  
 524 [2020](#)), however, indicate that their main composition is quite similar to that of the modern Lower  
 525 Indus River and LGM to Holocene Delta sands ([Fig. 3F](#)), only with more abundant micas in finer-  
 526 grained overbank deposits ([Andò et al., 2019](#)).

## 527 6.2. Detrital-zircon geochronology

528 Zircon ages from two Upper Indus samples collected between the Kabul confluence and the Salt  
 529 Range front, combined with data from one sample analysed by [Zhuang et al. \(2018\)](#), cluster mainly  
 530 between 33 and 124 Ma (n=248). The youngest cluster occurs at 17-21 Ma (n=5) with another  
 531 young age at 30 Ma and older ages spread in the Early Cretaceous to Jurassic (127-170 Ma; n=14),  
 532 Triassic to Permian (205-290 Ma; n=16), and Carboniferous to Ordovician (302-482 Ma; n=17).  
 533 Zircon grains yielded common Cambrian to Neoproterozoic (485-1000 Ma; n=139) and earliest  
 534 Statherian-Orosirian ages (1788-1948; n=39), and fewer Mesoproterozoic to late Statherian (1008-  
 535 1669 Ma; n=24) and earliest Orosirian to late Siderian ages (2018-2441 Ma; n=20). The oldest  
 536 cluster occurs at 2449-2491 Ma (n=9) and several Archean ages were also obtained (2520-3508;  
 537 n=11). Such a composite age spectrum reflects the many distinct geological events that affected the  
 538 diverse source-rock domains. Age spectra do not change significantly downstream of the  
 539 confluence with the Soan River, a minor tributary largely recycling Himalayan molasse exposed  
 540 within and around the Potwar Plateau ([Critelli and Garzanti, 1994](#); [Critelli and Ingersoll, 1994](#)).

541 Sand carried by the Himalayan tributaries of the Punjab (Jhelum, Chenab, Ravi, Beas, and Sutlej  
 542 samples combined; data after [Alizai et al., 2011](#)) include only a few young grains (1 late Oligocene,  
 543

545 7 Lutetian-Ypresian, 13 Mesozoic, 1 Carboniferous) and common mid-early Paleozoic (9 Devonian,  
546 13 Silurian, 48 Ordovician, 25 Cambrian) and Neoproterozoic zircons (18 Ediacaran, 32  
547 Cryogenian, 116 Tonian). Mesoproterozoic zircons are much less common (26 Stenian, 7 Ectasian,  
548 9 Calymmian) than Paleoproterozoic zircons (28 Statherian, 110 Orosirian, 22 Rhyacian, 14  
549 Siderian), and 15 Neoproterozoic, 4 Mesoarchean, and 3 Paleoproterozoic grains also occur ([Appendix  
550 Table A9](#)).

551 Sands in the Lower Indus River, Delta, and Fan display complex zircon-age distributions that reflect  
552 all components present in the huge catchment. The age spectrum obtained by combining data on  
553 eight modern fluvial and LGM to Holocene deltaic sands (n=766; [Clift et al., 2004, 2008, 2010](#))  
554 reveals a marked change in age proportions relative to modern Upper Indus sand. The percentage of  
555 Eocene-Cretaceous ages is notably lower, whereas a few more Miocene-Oligocene ages and many  
556 more Silurian-Ordovician, Tonian-Stenian, and mid-Paleoproterozoic ages occur. The age spectrum  
557 obtained by combining data on five Plio-Quaternary Indus Fan sands (n=624; [Clift et al., 2019](#)) is  
558 quite similar, with an even lower percentage of Eocene-Cretaceous ages ([Appendix Table A9](#)).

559 Sand in the Indus Delta and Fan contains zircons as young as 11.3-11.7 Ma ([Clift et al., 2010,  
560 2019](#)), which are notably younger than the youngest zircon grain found so far in the Upper Indus  
561 catchment (i.e., 15.9 Ma in Braldu sand). Zircon grains even as young as 4.4 Ma have been detected  
562 in the Indus Canyon ([Li et al., 2019](#)). In this regard, it is noteworthy that such very young grains are  
563 found only in silt samples with modal grain size  $\leq 40 \mu\text{m}$ , whereas the youngest zircon in the only  
564 sand sample analysed so far is dated as 14.2 Ma. Because such young ages were never obtained  
565 from the core of sand-sized zircon grains, it is likely that they correspond to small fragments  
566 chipped off the rim of zircon grains with an older core. In the same way, the notably greater  
567 abundance of relatively young lower Mesozoic to upper Paleozoic ages in Indus Canyon samples  
568 might reflect the greater frequency of zircon rims recording thermal events that followed the Pan-  
569 African orogeny. The other peculiar features of Indus Canyon zircons (spectrum of 988 ages  
570 combined from ten medium silts to fine sands deposited in the last 50 ka; [Li et al., 2019](#)) are the



571 much smaller population of Orosirian aged grains and the disappearance of the minor cluster around  
572 2.5 Ga, which also may be explained by a greater frequency of analysed small grains, originally  
573 representing younger rims surrounding older crystal cores.

### 574 6.3. Sand geochemistry

576 Upper Indus sand is similar to the UCC standard, apart from a moderate enrichment in elements  
577 preferentially concentrated in densest minerals such as zircon and monazite (Zr 254-323 ppm,  
578 Eu/Eu\* 0.51-0.61) and a depletion in Na, K, Rb and Ba preferentially hosted in alkali feldspars.

579 In sand carried by the Himalayan tributaries of the Punjab, most elements – except Si, and Ca in  
580 Jhelum and Sutlej sands – are depleted relatively to the UCC standard (Fig. 6B), which is typical of  
581 sand including detritus recycled from sedimentary and metasedimentary rocks. Elements  
582 preferentially hosted in densest minerals are slightly enriched in the Sutlej (Zr 281 ppm, Eu/Eu\*  
583 0.43) and Jhelum samples (Zr 230 ppm, Eu/Eu\* 0.60) and slightly depleted in the Chenab sample  
584 (Zr 123 ppm, Eu/Eu\* 0.72) owing to local differences in heavy-mineral concentration possibly  
585 caused by moderate selective-entrainment processes.

586 Relatively to Upper Indus sand, Lower Indus sand is depleted in most elements except Si, Ca, and  
587 P. This reflects major additional contribution from metamorphic and siliciclastic rocks richer in  
588 quartz. Relatively to Lower Indus River sand, LGM to Holocene deltaic sediments are instead  
589 enriched in most elements but Si, Y, REE, Zr and Hf, and especially in Al, Fe, Mg, K, Rb, V, Co,  
590 Ni, Cu, and loss on ignition (Fig. 6B), which is chiefly ascribed to their finer average grain size and  
591 higher phyllosilicate content.

### 594 6.4. Nd isotopes

596 In modern Indus sand,  $\epsilon_{Nd}$  values have been shown to decrease progressively from -8.4 upstream of  
597 the western syntaxis to -10.8 upstream of Tarbela Dam, and to -15.0 upstream of the delta,  
598 documenting a progressive dilution of less radiogenic and unradiogenic sediment generated in the



599 Karakorum and Transhimalayan arcs by more radiogenic sediment derived from the Nanga Parbat  
600 massif and Himalayan belt (Clift et al., 2002). In LGM to Holocene sand of the Indus Delta,  $\epsilon_{Nd}$   
601 varies between -11 and -15 (Clift et al., 2010; Jonell et al., 2018), whereas in turbidites of the Indus  
602 Fan  $\epsilon_{Nd}$  values remained mostly between -8.5 and -11.5 until 5.7 Ma, after which they declined to  
603 between -9 and -12 until 3 Ma and finally to between -11 and -14 thereafter (Clift et al., 2019).

## 605 7. Provenance of Thal Desert sand

606  
607 Based on the detailed compositional information on end-member sources illustrated above, the  
608 relative contributions from each geological domain to eolian sand of the Thal Desert can be  
609 calculated by forward mixing models according to the method illustrated in Garzanti et al. (2012)  
610 and Resentini et al. (2017). These calculations are non-unique and uncertain, being affected by  
611 various sources of error including the imprecise assessment of end-member sources owing to a  
612 limited number of samples and locally significant hydraulic-sorting effects. The calculations also  
613 depend on a variety of premises that are never strictly verified, including the assumption that  
614 selective mechanical or chemical breakdown of detrital components is negligible. The accuracy of  
615 the results thus needs to be increased by performing several independent tests according to different  
616 criteria for each dataset (i.e., petrography and heavy minerals, geochemistry, zircon age spectra, and  
617 Nd isotopes), keeping in mind that each estimate thus obtained refers only to the investigated set of  
618 components and grain-size range (i.e., sand, transparent heavy minerals, zircon, and Nd-rich phases;  
619 Garzanti, 2016). Extrapolating such diverse and not necessarily identical or even similar provenance  
620 budgets to the entire sediment flux, which is a necessary step to calculate sediment yields and  
621 erosion rates in different parts of the catchment, is a challenging endeavour fraught with  
622 uncertainties, which requires careful consideration of mineral fertilities in each source-rock domain  
623 (Malusà et al., 2016).

### 625 7.1. Petrography and heavy minerals

627 The provenance budget based on integrated petrographic and heavy-mineral data from the Upper  
628 Indus catchment and obtained after numerous sets of independent calculations indicated that  
629 bedload sand upstream of Tarbela Dam is predominantly derived from the Karakorum Range  
630 ( $60\pm 6\%$ ), with subordinate and subequal contributions from the Transhimalayan arcs ( $6\pm 4\%$  from  
631 the Ladakh Arc and South Tibet;  $14\pm 4\%$  from the Kohistan Arc) and Himalayan units (Nanga  
632 Parbat  $13\pm 3\%$ ; Tethyan and Greater Himalaya  $6\pm 3\%$ ) (Garzanti et al., 2005 p.296). Sand-budget  
633 estimates are far less precise downstream of Tarbela Dam, because sediment discharge has been  
634 profoundly modified by human activities. Because of effective sediment sequestration in the  
635 Tarbela reservoir, the composition of Indus sand downstream of the Kabul confluence is very close  
636 to Kabul sand, and modern sand at the Salt Range front was estimated to be derived in significant  
637 proportions from the Kabul ( $33\pm 2\%$ ) and Soan Rivers ( $11\pm 2\%$ ) (Garzanti et al., 2005 p.297).  
638 Compared to modern Upper Indus sand, Thal Desert dunes are notably poorer in quartz and  
639 sedimentary to low-rank metasedimentary rock fragments, and richer in feldspars, volcanic,  
640 metavolcanic and metabasite rock fragments, heavy minerals and especially hypersthene,  
641 documenting a significantly greater contribution from the Kohistan arc (Fig. 4). Although precise  
642 estimates are hard to obtain because of strong local selective-entrainment effects caused by wind  
643 deflation and partial overlap among end members, detrital modes of Thal dune sand can be  
644 satisfactorily reproduced as a 36:64 mixture of Kohistan and Upper Indus sand. Thal dune sand is  
645 thus assessed to be derived from the Transhimalayan arcs (40-45%, predominantly from the  
646 Kohistan arc), the Karakorum-Hindukush Ranges (40-50%, at least a third of which *via* the Kabul  
647 River according to suspended-load data of Rehman et al., 1997), the Nanga Parbat massif (< 10%),  
648 and the Himalayan belt (<10%, including detritus recycled by the Soan River).  
649 Further clues are obtained from electron-microprobe mineral-chemical data, which showed that the  
650 Kohistan arc played the principal role as a source of the most common groups of transparent heavy  
651 minerals, especially pyroxene and epidote (Fig. 7). The South Karakorum gneiss domes undergoing  
652 fast exhumation, and to a lesser extent the Nanga Parbat massif, represent important additional

653 sources of amphibole, garnet and zircon, whereas the contribution from other Himalayan domains is  
 654 major only for Lower Indus sand downstream of the Thal Desert (Lee et al., 2003; Alizai et al.,  
 655 2016).

## 656 657 7.2. Detrital-zircon geochronology

658  
659 In the Upper Indus catchment, Miocene grains were found only in sand of the Braldu and Hushe  
 660 Rivers draining the Baltoro granite. The youngest age population found in Thal Desert (22 Ma; 3%  
 661 of total zircons) and Upper Indus sand (17-21 Ma; 1% of total zircons) are thus most likely derived  
 662 from the Karakorum. Oligocene to Aptian grains (46% of total zircons in both Thal Desert and  
 663 Upper Indus sand) are predominantly derived from the Karakorum Range (peaks at 24-43 Ma and  
 664 99-130 Ma) and Transhimalayan arcs (43-96 Ma). Paleozoic and Neoproterozoic grains (18% and  
 665 30% of total zircons in Thal dunes and Upper Indus sand) are contributed by both Karakorum and  
 666 Himalayan sources, whereas Orosirian grains (peak at 1.85-1.86 Ga; 16% and 7% of total zircons in  
 667 Thal dunes and Upper Indus sand) are chiefly derived from the Nanga Parbat massif (Fig. 5).

668 A set of simple forward mixing calculations based on age groups defined by different criteria and  
 669 choosing different bandwidths indicate that zircons in Thal dune sand are largely derived from the  
 670 Transhimalayan arcs (34-40%), Karakorum-Hindukush Ranges (28-34%), Nanga Parbat massif (20-  
 671 21%), and Himalayan belt (11-12%) (Fig. 8A). Instead, zircon grains in modern Upper Indus sand  
 672 are mostly derived from the Karakorum-Hindukush Ranges (60-66%) and Transhimalayan arcs (17-  
 673 24%), with minor contributions from the Nanga Parbat massif (9%) and the Himalayan belt (7-8%).  
 674 The percentages of zircon grains supplied *via* the Kabul River draining both the Karakorum-  
 675 Hindukush Ranges and the Kohistan arc cannot be estimated accurately, but is most probably  
 676 significant (10-20%), as revealed by the greater percentage of Jurassic/Triassic ages in both Upper  
 677 Indus and Thal Desert sands than in any studied catchment upstream of Tarbela Dam.

## 678 679 7.3. Sand geochemistry

680  
681  
682  
683  
684  
685

681 The composition of Thal Desert sand compares well with that of modern Upper Indus sand (Fig.  
 682 6A), confirming that they share the same provenance with insignificant supply from the Jhelum  
 683 River or other Himalayan tributaries of the Punjab. Approximate forward mixing calculations based  
 684 on bulk-sediment geochemistry suggest that ~50% of the sand in the Thal dune field may be derived  
 685 from the Karakorum Range, 40% from the Kohistan arc, and only 10% from diverse Himalayan  
 686 sources. This indicates that the Kohistan arc contributed more at those times, and the Himalayan  
 687 belt less, than at present.

#### 689 7.4. Nd isotopes

690 The great intersample variability of  $\epsilon_{Nd}$  values observed in Thal Desert sand – even in samples  
 691 collected less than 30 km apart in the middle of the dune field – cannot be explained by differences  
 692 in provenance. This is thus an exemplary case that highlights the difficulties of decoding the  
 693 provenance signal carried by Nd isotopes, which requires full understanding of the detrital  
 694 components that control the Nd budget as well as of hydraulic-sorting processes (Garçon et al.,  
 695 2014). Moreover, if detritus is derived from multiple tectonic domains with overlapping signatures,  
 696 as it is the case in a large river system such as the Indus draining a complex orogenic belt, then the  
 697 same isotopic ratio can be produced by several different combinations of detrital sources and is  
 698 therefore unable to provide an unequivocal answer (Garzanti, 2016).

699 Based on bulk-sand provenance budgets discussed above in subsections 7.1 and 7.3 and on average  
 700  $\epsilon_{Nd}$  values given in Zhuang et al. (2015) for the Karakorum (-9.6), Ladakh-Kohistan arc (+4.9),  
 701 Greater Himalaya (-14.7) and Nanga Parbat massif (-25; Clift et al., 2002), the expected  $\epsilon_{Nd}$  in Thal  
 702 sand would range between -3.5 and -5.5 (*versus* observed values between -3.5 and -13.2), whereas  
 703 that of Indus sand upstream of Tarbela Dam would be close to -9 (*versus* an observed value of -  
 704 10.8; Clift et al., 2002). Observed values more negative than expected – outside the  $\pm 1$   $\epsilon_{Nd}$   
 705 uncertainty estimated by Jonell et al. (2018) – call for an explanation.

707 Studies of sand generated in the Himalayan orogen have shown that 80-90% of their Nd is  
708 contained in transparent heavy minerals, mostly in allanite and monazite and subordinately in  
709 titanite, apatite, other epidote-group minerals, and amphibole (Garzanti et al., 2010, 2011). The Nd  
710 isotopic signature of orogenic sediment is thus markedly affected by the presence of REE-rich  
711 monazite and allanite grains even where their concentration is very low (Garçon et al., 2014; Jonell  
712 et al., 2018; Garzanti et al., 2019).

713 High-resolution heavy-mineral data obtained with semi-automated Raman spectroscopy (Appendix  
714 Table A4) indicate that REE-rich allanite is most abundant by far in Karakorum-derived sand,  
715 minor in sand from the Greater Himalaya, and rare in sand from the Transhimalayan arcs and  
716 Nanga Parbat massif (Liang et al., 2019), whereas monazite was detected only in sand generated in  
717 the Karakorum and Greater Himalaya. The average  $\epsilon_{Nd}$  value carried by monazite grains is therefore  
718 predicted to be more negative than that carried by allanite. This is corroborated by semi-automated  
719 Raman-point-counting heavy-mineral analysis, which detected significant monazite (0.3 tHM%)  
720 and a little allanite (0.1 tHM%) in sample S1462 yielding the most strongly negative  $\epsilon_{Nd}$  value (-  
721 13.2), a little monazite (0.1 tHM%) and no allanite in sample S1474 yielding the other strongly  
722 negative  $\epsilon_{Nd}$  value (-10.9), and some allanite (0.1 and 0.6 tHM%) but no monazite in samples  
723 S1470 and S1463 yielding the least negative  $\epsilon_{Nd}$  values (-8.7 and -3.5).

724 The results of heavy-mineral point-counting cannot be very precise in this regard, because the  
725 amount of monazite in our sand samples is exceedingly small. Moreover, Nd-bearing minerals may  
726 be present as undetected tiny inclusions in other detrital grains. Nevertheless, because every 100  
727 ppm of monazite hosting  $\sim 10^5$  ppm of Nd contributes  $\sim 10$  ppm of Nd to the bulk sand, our results  
728 suggest that most of the Nd in sample S1462 (containing 30 ppm of Nd overall) and much of the Nd  
729 in sample S1474 (containing only 19 ppm overall) may well be provided by monazite of Greater  
730 Himalayan provenance with an  $\epsilon_{Nd}$  value of  $\sim 15$  (Cottle et al., 2019), thus resulting in unexpectedly  
731 low bulk-sand  $\epsilon_{Nd}$  values of -13.2 and -10.9. A few monazite (or allanite) grains from the Nanga

732 Parbat massif may also be responsible for such a sharp local drop in  $\epsilon_{Nd}$  values. These observations  
 1  
 733 indicate that REE-rich monazite (or allanite) grains carrying a strongly negative  $\epsilon_{Nd}$  fingerprint,  
 3  
 4  
 734 even in amounts so small that seriously challenge the resolution power of current analytical  
 6  
 735 methods, can produce an unexpectedly strong local decrease in  $\epsilon_{Nd}$  values. The uncertainties of  
 8  
 9  
 106 provenance budgets based on bulk-sand Nd isotopes are consequently increased.

## 138 **8. Provenance of Lower Indus, Indus Delta, and Indus Fan sand**

### 140 *8.1. Petrography and heavy minerals*

142 In the Lower Indus catchment, where the sediment flux has been profoundly modified by man,  
 22  
 23  
 243 sediment-budget calculations are affected by large uncertainties. Big dams and link canals, built  
 25  
 264 along both the trunk river and Punjab tributaries since Pakistan's independence in 1947 and  
 27  
 28  
 295 especially after the Indus Waters Treaty in 1960, have greatly hampered sediment transit across the  
 30  
 3146 Punjab plains. The entire water discharge of the Ravi and Sutlej Rivers has been retained upstream  
 32  
 33  
 347 in India except during monsoon floods, triggering sediment reworking and erratic mixing and  
 34  
 35  
 368 blurring of provenance signals in Pakistan downstream. All along the eastern edge of the Thal  
 37  
 38  
 399 Desert, changes in composition observed in sand of the Jhelum River and downstream of the  
 39  
 40  
 410 Jhelum–Chenab confluence reveal fluvial reworking of Thal dune sand, which may locally  
 42  
 43  
 445 represent up to more than 20% of river bedload (Garzanti et al., 2005 p.297). Forward mixing  
 44  
 45  
 462 calculations based on the integrated petrographic and mineralogical dataset tentatively indicated a  
 47  
 483 39±4% contribution from the Himalayan tributaries of the Punjab to Lower Indus sand of (15±6%  
 49  
 50  
 514 of which from the Jhelum, 33±7% from the Chenab, 4±4% from the Ravi, 40±8% from the Sutlej,  
 51  
 52  
 535 and 9±3% from reworking of Thal dunes; Garzanti et al., 2005 p.297-298).

54  
 5556 Provenance budgets thus suggest relative supply from the Upper Indus and Himalayan tributaries of  
 56  
 57  
 587 the Punjab in proportion 60:40, with very minor additional detritus from the Sulaiman-Kirthar  
 59  
 6058 Ranges in the west. These figures are notably similar to what is observed on the eastern side of  
 61  
 62  
 63  
 64  
 65

759 peninsular India, where sediments in the Bengal Delta and Bengal Fan are assessed to be derived  $\geq$   
 760 60% from the Brahmaputra River draining the eastern Himalayan syntaxis and  $\leq$  40% from the  
 761 Ganga River chiefly draining the Himalayan belt, with very minor additional detritus from the Indo-  
 762 Burman Ranges in the east (Lupker et al., 2013; Borromeo et al., 2019; Garzanti et al., 2019). A  
 763 remarkable symmetry in the proportion of sediment generated from the Himalayan belt and carried  
 764 by rivers draining the Himalaya exclusively or dominantly (e.g., Punjab rivers and Ganga) *versus*  
 765 rivers sourced in Tibet and cutting across the western and eastern syntaxes (e.g., Indus and  
 766 Brahmaputra) is thus observed on opposite sides of the India-Asia collision system (figure 5 in  
 767 Garzanti et al., 2005).

768 Given the overall similarity in composition (Fig. 9A), sand budgets based on petrographic and  
 769 heavy-mineral data are not drastically different for the modern Lower Indus, the LGM to Holocene  
 770 Delta, and the early Pleistocene Indus Fan. However, a subtle compositional shift in detrital modes  
 771 from Miocene-Pleistocene deep-sea-fan turbidites to Holocene and modern fluvio-deltaic sands  
 772 points to progressively increasing relative supply from the Himalayan belt (light grey arrow in Fig.  
 773 9B), which is consistent with decreasing  $\epsilon_{Nd}$  values and increasing relative abundance of zircon  
 774 grains older than 300 Ma observed in Indus Fan turbidites since the latest Miocene (Clift et al.,  
 775 2019). At even earlier, mid-Miocene times (18-14 Ma), a sudden influx of volcanic detritus to the  
 776 foreland basin testifies to the onset of rapid exhumation of the Kohistan arc in the western Himalaya  
 777 syntaxis (Kamlial Formation in Fig. 9A; Najman et al., 2003), which is consistent with increasing  
 778  $\epsilon_{Nd}$  values recorded by Indus Fan turbidites from 17 Ma to 9.5 Ma (Clift et al., 2019).

## 8.2. Detrital-zircon geochronology

780 Data from Clift et al. (2004, 2008, 2019) show that zircon grains younger than 125 Ma – which  
 781 account for 47-49% of the zircon population in Upper Indus and Thal Desert sands – are still  
 782 common in LGM to Holocene sand of the Indus Delta (34%) downstream. Young grains are also  
 783 found in the Plio-Quaternary Indus Fan (17%), although they are few in sand carried by Himalayan



786 tributaries of the Punjab (~3%). This indicates that detrital zircon in the modern Lower Indus River,  
 787 LGM to Holocene Delta, and Plio-Quaternary Fan is derived from the Upper Indus and Punjab  
 788 tributaries in roughly similar proportions (Fig. 8B), with notable short-term variations in space and  
 789 time (Clift et al., 2008, 2019; Li et al., 2019). Despite a zircon-age dataset that has been rapidly  
 790 expanded in the last decade, estimates of zircon contributions from various parts of the catchment  
 791 still vary widely. Alizai et al. (2011, their table 7 and figure 12A) estimated that two-thirds of zircon  
 792 grains in the modern delta are supplied by the Himalayan tributaries of the Punjab (two-thirds of  
 793 which by the Sutlej River), which is largely explained by the high zircon fertility of Himalayan  
 794 rocks. Our set of forward mixing calculations, based on age groups defined by diverse criteria,  
 795 suggest that the Upper Indus may have supplied on average 45-48% of detrital zircon to the Plio-  
 796 Quaternary Fan and up to 55-67% of detrital zircon to the LGM-Holocene Delta. Similar, but less  
 797 robust estimates are obtained from Indus Canyon zircon-age data (Li et al., 2019), which is largely  
 798 ascribed to the finer grain-size of the analysed zircons and short timescale variability. The different  
 799 proportions of original cores and rims of zircon grains in samples of markedly different grain size  
 800 may explain the notable variability observed even at the centennial to millennial time scale, which  
 801 may be at least partly caused by the variable grain size of the studied samples rather than by  
 802 provenance changes.

### 8.3. Sand geochemistry

803  
 804 The geochemical composition of modern Lower Indus sand indicates a much higher percentage of  
 805 Himalayan detritus than in Thal Desert and Upper Indus River sands (Fig. 6B). Forward mixing  
 806 calculations, affected by the same uncertainties discussed for the petrographic-mineralogical sand  
 807 budget illustrated in subsection 8.1 above, suggest that the Upper Indus and the Himalayan  
 808 tributaries of the Punjab provide sand in roughly equal amounts to the Lower Indus and LGM to  
 809 Holocene Delta ( $50\pm 8\%$  each).

### 8.4. Nd isotopes



814  
 815 Nd isotopes have long been used to identify sediment sources and to trace erosion patterns in the  
 816 huge Indus drainage basin. In modern Indus River sand, the sharp decrease in  $\epsilon_{Nd}$  values across the  
 817 foreland basin documents the progressive dilution of detritus shed from more juvenile Karakorum  
 818 and Transhimalayan arc sources by more radiogenic Himalayan detritus supplied by the Punjab  
 819 tributaries in the lower course (Clift et al., 2002). Values as negative as -15.4 in the modern delta  
 820 contrast with less negative values measured from Pleistocene Indus Fan sediments cored at ODP  
 821 Site 720 ( $\epsilon_{Nd}$  -12.5 and -14.0; Clift et al., 2001) and IODP Sites U1456 and U1457 ( $\epsilon_{Nd}$  -9.5 and -  
 822 13.0; Clift et al., 2019; Yu et al., 2019). Although this discrepancy may partly result from reduced  
 823 sediment flux from the Upper Indus after the closure of the Tarbela Dam, Indus Delta sediments do  
 824 document a progressive increase of detrital supply from the radiogenic Lesser Himalaya since the  
 825 Last Glacial Maximum (LGM), with relatively reduced contributions from Transhimalayan and  
 826 Karakorum sources. The  $\epsilon_{Nd}$  values decreased from -11 to -12 between the LGM and the beginning  
 827 of the Younger Dryas (~12.7 ka), to reach -15 around -8.7 ka, a change ascribed to enhanced  
 828 erosion along the southern Himalayan front caused by the increasing intensity of summer monsoon  
 829 rains (Clift et al., 2008, 2010).  
 830 Upper Miocene to Pleistocene Indus Fan sediments recently drilled by IODP Expedition 355 to the  
 831 Laxmi Basin also show less radiogenic  $\epsilon_{Nd}$  values than recent sediments in the Indus Delta, with a  
 832 pronounced decline throughout the Pliocene ascribed to an accelerated exhumation of the Lesser  
 833 Himalaya and, to a lesser extent, of the Nanga Parbat massif (Clift et al., 2019). Laxmi Basin  
 834 sediments deposited during the last 600 ka yielded less radiogenic  $\epsilon_{Nd}$  values mostly between -9.5  
 835 and -13.0, which however reflects mixing of sediment supplied not only by the Indus River but also  
 836 by rivers draining Deccan Trap basalts in Peninsular India (Yu et al., 2019), as independently  
 837 documented by heavy-mineral data (Garzanti et al., 2020).

## 9. Climatic control on latest Quaternary erosion patterns

840  
841  
2  
842  
4  
5  
843  
7  
844  
9  
10  
845  
11  
12  
846  
14  
15  
847  
16  
17  
848  
19  
20  
849  
21  
22  
850  
24  
25  
851  
26  
27  
852  
28  
29  
853  
31  
32  
854  
33  
34  
855  
36  
37  
856  
38  
39  
857  
41  
42  
858  
43  
44  
859  
46  
47  
860  
48  
49  
861  
51  
52  
862  
53  
54  
863  
55  
56  
864  
58  
59  
865  
60  
61  
62  
63  
64  
65

In provenance studies, each one of the many different possible approaches adds useful complementary information but hardly ever provides a sharp univocal response. Among bulk-sediment methods, petrographic analysis applies to bedload sand only and geochemistry has limited discrimination power with the notable exception of mafic source rocks. Heavy-mineral suites are strongly affected by hydraulic sorting and selective chemical dissolution during the successive stages of a sedimentary cycle. Age spectra of detrital zircon are strongly distorted by fertility effects and heavily biased in favour of felsic igneous and metaigneous sources; moreover, grains recycled even several times from siliciclastic covers cannot be distinguished from first-cycle grains derived directly from basement rocks. Nd isotopic ratios suffer from overlap among the fingerprints of diverse source-rock domains, are strongly influenced by grain size and hydraulic-sorting effects, and are highly dependent on rare minerals very rich in REE such as monazite, which can control the Nd budget even if present in amounts so small that can hardly be assessed precisely enough by current techniques.

Nevertheless, the evidence provided by these different methods combined, as illustrated in [Sections 4, 5 and 6](#) and discussed in [Sections 7 and 8](#), indicates robustly enough that the Thal dune field was fed entirely by the paleo-Upper Indus at a time when erosion was focused to the north of the Himalayan belt, and specifically in the Kohistan arc and Karakorum Range. All provenance budgets based on integrated petrographic-mineralogical data, bulk-sediment geochemistry, age spectra of detrital zircon, and Nd isotope ratio converge to indicate that Thal Desert sand was originally derived ~40% from erosion of the Kohistan arc, up to 50% from the Karakorum Range, and only in minor amount from diverse Himalayan sources. Instead, ~60% of modern Indus sand upstream of Tarbela Dam is assessed to be derived from the Karakorum, the rest being supplied in subequal amounts by the Transhimalayan arcs and the Himalayan belt.

In Thal Desert sand, the low abundance of quartz and high abundance of feldspars and volcanic, metavolcanic and metabasite rock fragments, the very rich tHM suites including common

866 hypersthene, the common zircon grains of Late Cretaceous to early Paleogene age, and the  $\epsilon_{Nd}$   
 1  
 867 values less negative than those of Upper Indus sand and as high as -3.5 are all clear evidence of  
 3  
 868 major contribution from the Kohistan arc. Notably greater detrital supply from juvenile sources  
 4  
 5  
 6  
 869 lying to the north of the Himalayan belt than in the modern Upper Indus system indicates markedly  
 8  
 870 different conditions of sediment generation at a time when the paleo-Upper Indus delivered to the  
 10  
 11  
 871 foreland basin volumes of sand to be subsequently reworked by wind and accumulated in the Thal  
 12  
 13  
 872 dune field.

### 16 17 18 9.1. Eolian sedimentation in the dry latest Pleistocene

19  
 20  
 21 216 A precise chronology of the evolution of the Thal Desert has not been established yet, whereas  
 22  
 23  
 24  
 25  
 26  
 27  
 28  
 29  
 30  
 31  
 32  
 33  
 34  
 35  
 36  
 37  
 38  
 39  
 40  
 41  
 42  
 43  
 44  
 45  
 46  
 47  
 48  
 49  
 50  
 51  
 52  
 53  
 54  
 55  
 56  
 57  
 58  
 59  
 60  
 61  
 62  
 63  
 64  
 65

217 thermoluminescence dating of eolian sediments in the Thar Desert of southern Pakistan has  
 218 revealed multistep phases of dune accretion through the last 200 ka alternating with precession-  
 219 driven interludes of wetter climate (Singhvi et al., 2010). The last major phase of dune growth in the  
 220 eastern Thar Desert took place under a transitional climate, when SW monsoon winds were being  
 221 re-established following a peak in aridity during the LGM characterized by a very weak SW  
 222 monsoon. Sand aggradation in the eastern desert took place between 17 ka and 14 ka and lasted  
 223 until 9 ka, at the onset of the early Holocene wet stage (Dhir et al., 2010; Singhvi et al., 2010). In  
 224 contrast, the western Thar Desert has been supplied by sediment from the Indus Delta since the  
 225 onset of the wetter Holocene and expanded further west as the climate dried after the mid-Holocene  
 226 (East et al., 2015). The recent finding of Mesolithic artefacts dated as the first millennia of the  
 227 Holocene on top of sand dunes of both Thar and Thal Deserts (Biagi et al., 2019), suggests that a  
 228 chronology similar to the eastern Thar Desert may be extrapolated to the Thal Desert.

229 The compositional fingerprints of Thal dunes indicate that detritus was largely generated by erosion  
 230 in the high Karakorum and Kohistan Ranges in the northern part of the western Himalayan syntaxis  
 231 (Fig. 9A). During deglaciation following the LGM, sediment fluxes were augmented by incision of  
 232 moraines and fluvial terraces in the mountains (Clift and Giosan, 2014; Blöthe et al., 2014; Jonell et

893 [al., 2017b](#)). In this latest Pleistocene period of weak summer monsoonal rains, meltwater fluxes  
 894 from shrinking mountain glaciers were insufficient to guarantee a constant full sediment-transport  
 895 capacity to the paleo-Upper Indus River, fluvial sediments were dumped and extensively reworked  
 896 by wind in the lowlands, and sand blown by progressively strengthening winds accumulated in dune  
 897 fields all across the dry foreland basin ([Fig. 10A](#)).

898 In the Indus Delta, a ravinement surface formed at this time of sea-level rise, as documented by a  
 899 hiatus separating sand deposited during the LGM (radiocarbon ages 28.7 ka and 38.9 ka) from the  
 900 overlying sediments deposited since ~15 ka and documenting sustained progradation since ~12 ka  
 901 ([Clift et al., 2008, 2010](#)). Sediments deposited during and immediately after the LGM carry a  
 902 notably less negative isotopic signature ( $\epsilon_{Nd}$  -11 to -12) than more recent deposits, which confirms a  
 903 greater contribution from juvenile Transhimalayan sources at those times ([Fig. 8B](#)). The  $\epsilon_{Nd}$  values  
 904 started to decrease with the beginning of the Younger Dryas, a consequence of increasingly  
 905 focalized erosion along the southern Himalayan front ([Clift et al., 2010](#)). Changing climatic  
 906 conditions since the LGM have certainly contributed to such a prominent shift in erosion patterns  
 907 and accelerated erosional denudation of the Himalayan belt ([Clift et al., 2008, 2019](#)).

## 909 *9.2. Changing landscapes in the Holocene*

910 Global warming and intensification of the South Asian monsoon led to much wetter conditions in  
 911 the early Holocene, when water and sediment discharge from the Himalayan orogen very markedly  
 912 increased, fuelled by heavier monsoonal rains. This is documented by notably enhanced freshwater  
 913 influx peaking around 10.8 ka, as recorded by low  $\delta^{18}O$  in foraminifera off the coast of Pakistan  
 914 ([Staubwasser et al., 2002](#)) and by progradation of the Indus Delta even at a time of rapid sea-level  
 915 rise, fostered by augmented sediment delivery between 13 ka and 9.5 ka ([Giosan et al., 2006b](#)). On  
 916 the opposite side of Peninsular India, the strengthened early Holocene monsoon is held responsible  
 917 for greatly increased sediment supply to the Bengal Delta between ~11 ka and 7 ka ([Goodbred and](#)  
 918 [Kuehl, 2000](#)). This wet period fostered the formation of lakes in the Thar Desert from ~7 ka to ~5

920 ka (Enzel et al. 1999; Roy et al., 2009). Lakes desiccated at the onset of a new arid phase at ~4 ka  
 1  
 921 (Giosan et al., 2012; Dixit et al., 2014), which was followed by several other wet events of shorter  
 3  
 922 duration and smaller magnitude (Prasad and Enzel, 2006).

6  
 923 The Thal Desert, therefore, testifies to the markedly different landscape that preceded the wet early  
 8  
 924 Holocene, when strongly enhanced water discharge led to incision and reworking of the Thal and  
 10  
 925 Thar dune fields by the Indus and its Punjab tributaries draining the Himalayan front, directly and  
 13  
 926 most strongly hit by the heavy rains brought in by the renewed strength of the South Asian  
 15  
 927 monsoon (Fig. 10B).

## 928 20 929 **10. Conclusions**

22  
 930  
 24  
 931 The distinctive petrographic, heavy-mineral, mineral-chemical, U-Pb zircon-age, geochemical, and  
 25  
 26  
 932 Nd-isotope fingerprints of Thal Desert sand reveal that this dune field was fed entirely by the paleo-  
 28  
 933 Upper Indus at a time when erosion was focused in the Kohistan arc and Karakorum Range to the  
 30  
 934 north of the Himalayan belt. Thermoluminescence chronology and artefacts dated at the first  
 32  
 33  
 935 millennia of the Holocene found on top of sand dunes of both Thal and Thar Deserts indicate that  
 35  
 936 these dune fields expanded in semi-dry climate during the latest Pleistocene. In this period, global  
 37  
 937 warming and glacial retreat following the Last Glacial Maximum fostered enhanced detrital supply  
 40  
 938 from the high Kohistan and Karakorum Ranges of the western Himalayan syntaxis. When  
 42  
 43  
 939 meltwater fluxes from shrinking mountain glaciers were reduced, at a time of weak monsoonal  
 45  
 940 rains, the sediment-transport capacity of the paleo-Upper Indus River was also reduced. Fluvial  
 47  
 941 sediments were dumped and extensively reworked by wind in the lowlands, and sand accumulated  
 50  
 942 in dune fields across the dry foreland basin. Sand stored in the Thal dune field thus testifies to a  
 52  
 943 major change in Himalayan landscape and erosion patterns that took place at a time of rapid  
 54  
 944 climatic transition from dry periglacial settings during the Last Glacial Maximum to wet conditions  
 57  
 945 in the early Holocene, when markedly enhanced river water and sediment discharge was fuelled by  
 59  
 946 intensified monsoonal rainfall.

60  
 61  
 62  
 63  
 64  
 65

947  
948  
949  
950  
951  
952  
953  
954  
955  
956  
957  
958  
959  
960  
961  
962  
963  
964  
965  
966  
967  
968  
969  
970  
971  
972  
973  
974  
975  
976  
977  
978  
979  
980  
981  
982  
983  
984  
985  
986  
987  
988  
989  
990  
991  
992  
993  
994  
995  
996  
997  
998  
999

## ACKNOWLEDGMENTS

Heartfelt thanks to Giacomo Ghielmi and Filippo Lazzati, who collected sand samples in the Thal Desert and around the western Himalayan syntaxis, and to Henry Munack and Jan Blöthe who provided samples from Ladakh. The Braldu and Hushe samples were collected and kindly provided by Mike Searle. Guido Pastore helped with several geochronological analyses. This study was supported financially by Projects MIUR-PRIN 2015EC9PJ5 “The subduction and exhumation of the continental lithosphere: their effects on the structure and evolution of the orogens” and MIUR – Dipartimenti di Eccellenza 2018–2022, Department of Earth and Environmental Sciences, University of Milano-Bicocca. We warmly thank ESR Editor Chris Fielding and an anonymous reviewer for their useful comments and constructive advice.

## SUPPLEMENTARY MATERIALS

Supplementary data associated with this article, to be found in the online version at [http://dx.doi.\\_\\_\\_\\_\\_](http://dx.doi._____), include information on sampling sites (Table A1), together with the complete datasets on sand petrography (Table A2), heavy minerals (Table A3), heavy-mineral point-counting by semi-automated Raman spectroscopy (Table A4), percentages of amphibole, garnet, epidote, and pyroxene varieties in each source-rock domain (Table A5), sand geochemistry (Table A6), and Nd isotopes (Table A7). A compilation of Nd isotope values from bedrocks and sediments from the Himalayan-Karakorum orogen is shown in Table A8 and original and literature data on zircon-age distributions are summarized in Table A9, whereas the full original detrital-zircon geochronology dataset is illustrated in Appendix B. The Google-Earth™ map of sampling sites [Thal Review.kmz](#) is also provided.

## 973 FIGURE CAPTIONS

974  
975

976

977

978

979

980

981

982

983

984

985

986

987

988

989

990

991

992

993

994

995

996

997

998

999

1000

1001

1002

1003

1004

1005

1006

1007

1008

1009

1010

1011

1012

1013

1014

1015

1016

1017

1018

1019

1020

1021

1022

1023

1024

1025

1026

1027

1028

1029

1030

1031

1032

1033

1034

1035

1036

1037

1038

**Figure 1.** The Thal Desert is situated where the Upper Indus reaches the foreland basin to the south of the western Himalayan syntaxis (WHS) and to the west of the Punjab plain. Location of the four studied Thal dune samples is indicated by orange stars. Inset shows area enlarged in the Google Earth™ image; the white circle indicates the Indus Canyon, and the white star the location of the Laxmi Basin targeted by IODP Expedition 355. Ga and Br = Ganga and Brahmaputra Rivers.

**Figure 2.** Geological map of the Indus catchment (mod. after [Garzanti et al., 2005](#)) indicating the studied Indus tributaries and sampling sites. Blue stars in the Indus Delta indicate location of the Thatta (T), Jati (J), and Ketu Bandar (K) cores.

**Figure 3.** Sand petrography. Thal Desert sand is enriched in plagioclase, volcanic to metabasite rock fragments, and pyroxenes (**A**; S1462) relative to Upper Indus sand (**B**; S1447). Sand supplied by Punjab tributaries downstream of the Thal Desert includes abundant metasedimentary detritus from the Himalaya (**C**; S1424). Sands in the Lower Indus River (**D**; S1487), Holocene Delta (**E**; sample TH10\_8 in [Clift et al., 2010](#)) and lower Pleistocene Fan (**F**; sample U1456 39F1W130/132, collected during IODP Expedition 355; [Pandey et al., 2016](#)) are notably poorer in feldspars and richer in quartz, metasedimentary rock fragments and micas relatively to Thal dunes. All samples with crossed polarizers; blue bar for scale = 100 μm.

**Figure 4.** Detrital modes of Thal Desert dunes compared with sand carried by the Upper Indus and its tributaries draining the diverse geological domains of the western Himalayan syntaxis (QFL and LmLvLs diagrams after [Ingersoll et al., 1984](#)). Thal dune sand contains more feldspars, more volcanic, metavolcanic, and metabasite rock fragments, more heavy minerals, and more hypersthene than modern Upper Indus sand, indicating greater contribution from the Kohistan arc.



999 Q = quartz; F = feldspar; L = lithic grains (Lm = metamorphic; Lv = volcanic; Ls = sedimentary);  
 1000 other parameters as in [Table 1](#). Data in the LmLvLs and heavy-mineral triangular diagrams are  
 1001 centered to allow better visualization ([von Eynatten et al., 2002](#)).

1002  
 1003 **Figure 5.** U-Pb age spectra of detrital zircons in Thal dunes and in sands carried by the Upper Indus  
 1004 and its tributaries. Zanskar data after [Jonell et al. \(2017a\)](#); Dir and most Upper Hunza ages after  
 1005 [Zhuang et al. \(2018\)](#). Main events of crustal growth in the western Himalayas are indicated. The  
 1006 multimodal spectrum of Thal sand indicates dominant zircon supply from the western Himalayan  
 1007 syntaxis, including the Karakorum Range (Baltoro granite, South Karakorum gneiss domes, and  
 1008 central batholith) and Transhimalayan arcs (ages from 20 to 130 Ma), together with the Nanga  
 1009 Parbat massif (sharp 1.85 Ga peak). Contribution from the Greater and Tethys Himalaya is  
 1010 subordinate (mostly Neoproterozoic ages).

1011  
 1012 **Figure 6.** Sedimentary geochemistry. Elements are arranged following the periodic table group by  
 1013 group and data are normalized to the median composition of average Upper Indus (A) and Lower  
 1014 Indus sand (B) ([Appendix Table A6](#)). **A)** Note: i) similar composition of Thal Desert and Upper  
 1015 Indus sands, which have higher concentration in most chemical elements relatively to Himalayan-  
 1016 derived sand; ii) peculiar composition of Kohistan sand, with high Mg, Sc, V, Co, Ni and Cu, and  
 1017 low Th, U Nb, Ta, and Eu anomaly; iii) low Cr and Ni in Ladakh sand; iv) heavy-mineral  
 1018 enrichment and strongly negative Eu anomaly in Hispar sand, owing to a local selective-  
 1019 entrainment effect. **B)** Note: i) both Thal Desert and Upper Indus sands have higher concentration in  
 1020 most chemical elements than Himalayan-derived sand of Punjab tributaries; ii) high K, Rb, V, Ni  
 1021 and Cu in finer-grained sediments of the LGM to Holocene Indus Delta (data after [Clift et al.,](#)  
 1022 [2010](#)); iii) markedly variable Eu anomaly in both Thal Desert and Punjab tributary sands chiefly  
 1023 controlled by local selective-entrainment effects ([Garzanti et al., 2010](#)).



**Figure 7.** MDS maps based on electron-microprobe chemical analyses of amphibole, garnet, epidote, and pyroxene (mod. after figure 7 in [Liang et al., 2019](#)). The Kohistan arc is indicated as the main supplier of epidote (**A**) and pyroxene (**B**), whereas amphibole (**C**) and garnet (**D**) were largely derived from the Karakorum Range (Hispar River), Nanga Parbat massif, and Himalayan belt.

**Figure 8.** MDS maps based on U-Pb age spectra of detrital zircons highlight focused erosion of the western Himalayan syntaxis at LGM times and increasing contributions from the Himalayan belt in the Holocene. **A**) Thal dunes show a greater affinity with Transhimalayan arcs than Upper Indus sand. Zanskar data after [Jonell et al. \(2017a\)](#); Dir, Kabul, and most Upper Hunza ages after [Zhuang et al. \(2018\)](#). **B**) Sands of the Lower Indus, Thar dunes, and Pleistocene Fan plot close to Himalayan tributaries of the Punjab, showing strong Himalayan influence. Instead, Holocene and especially LGM Delta sands display closer affinity to sands of the Upper Indus, Thal dunes, and Transhimalayan arcs. Data sources: Punjab tributaries and Thar Desert ([Alizai et al., 2011](#)); Lower Indus River ([Clift et al., 2004](#)); LGM to Holocene Indus Delta ([Clift et al., 2008, 2010](#); 4 samples combined from Thatta, Jati, and Keti Bandar cores, age 6.6-9.7 ka, n=288; 2 samples combined from Keti Bandar core, age 28.7 ka, n=229); Indus Canyon ([Li et al., 2019](#); 6 samples combined, age 0.4-6.7 ka, n=507); Indus Fan ([Clift et al., 2019](#); sample U1456A-11H-6 60/69, age 0.9 ka). Eastern Karakorum: Hushe + Braldu samples; western Karakorum: Upper Hunza + Hispar samples.

**Figure 9.** Petrography and heavy minerals in Indus River sands, from the western Himalayan syntaxis to the deep sea. **A**) Quartz increases downstream of the Thal Desert because of major supply from Punjab tributaries draining the Himalayan belt. Rock fragments are dominantly sedimentary in sand from the Kirthar Range but locally include volcanic/metavolcanic and ultramafic types shed by the Waziristan and Zhob ophiolites in sand from the Sulaiman Range. Otherwise, modern sand in the Indus sedimentary system includes a variety of sedimentary and

1051 metamorphic grains with subordinate volcanic/metavolcanic types. Volcanic rock fragments are  
 1052 most abundant in the Kamliyal Formation, reflecting incipient dissection of the Kohistan arc at mid-  
 1053 Miocene times (Najman et al., 2003). **B)** A progressive shift in detrital modes indicates increasing  
 1054 contribution from Himalayan tributaries of the Punjab from Miocene-Pleistocene fan turbidites to  
 1055 Holocene deltaic and modern Lower Indus fluvio-deltaic sands (light grey arrow). Q = quartz; F =  
 1056 feldspar; L = lithic grains; Ky = kyanite; Sil = sillimanite; Sp = Cr-spinel; St = staurolite; other  
 1057 parameters as in Table 1. Data sources: modern sand (Garzanti et al., 2005), LGM to Holocene  
 1058 Delta (Clift et al., 2010), Upper Miocene-Pleistocene Fan, IODP sites U1456 and U1457 (Garzanti  
 1059 et al., 2020).

**Figure 10.** Drastically changing landscapes in the western Himalayan foreland basin driven by  
 latest Quaternary climate change. Pictures in rectangles aim at representing natural sceneries and  
 life conditions at the time, from mountain highlands to the coastal plain. Circles represent rough  
 proportions of detritus contributed by the Upper Indus (orange dots) *versus* the Himalayan  
 tributaries of the Punjab (blue dots). A) In the dry latest Pleistocene, during deglaciation following  
 the LGM, sediment fluxes were largely generated by incision of moraines and fluvial terraces in the  
 high Kohistan and Karakorum Ranges surrounding the western Himalayan syntaxis. B) In the wet  
 early Holocene, water and sediment fluxes were instead largely fuelled by heavy rainfall along the  
 southern front of the Himalayan belt directly hit by humid air masses brought in by the intensified  
 summer monsoon.

**Table 1.** Petrographic and heavy-mineral signatures of Thal Desert sand compared with sands  
 carried by the Indus River and its tributaries draining different source-rock domains. Data sources:  
 Miocene Kamliyal Formation (Najman et al., 2003); Indus Delta cores (Clift et al., 2010); modern  
 Indus sands and Neogene Indus Fan turbidites (Garzanti et al., 2005, 2020). Q = quartz; F =  
 feldspars (KF = K-feldspar; P = plagioclase; L= lithic grains (Lvm = volcanic and metavolcanic; Lc

1077 = carbonate and metacarbonate; Lh = chert; Lsm = shale, siltstone, slate, and metasiltstone; Lmf =  
 1078 felsic metamorphic; Lmb = metabasite; Lu = ultramafic); HM = heavy minerals; MI\* =  
 1079 Metamorphic Index; tHMC = transparent heavy-mineral concentration. ZTR = zircon + tourmaline  
 1080 + rutile; Ttn = titanite; Ep = epidote-group minerals; Grt = garnet; SKS = staurolite + kyanite +  
 1081 sillimanite; Amp = amphibole; Px = pyroxene (Cpx = clinopyroxene; Opx = orthopyroxene, mostly  
 1082 hypersthene); &tHM = other transparent heavy minerals (apatite, chloritoid, Cr-spinel, olivine,  
 1083 prehnite, pumpellyite, brookite, andalusite, barite).

## 1085 REFERENCES

- 1086 Ahmad, T., Harris, N., Bickle, M., Chapman, H., Bunbury, J., Prince, C., 2000. Isotopic constraints  
1087 on the structural relationships between the Lesser Himalayan Series and the High Himalayan  
1088 Crystalline Series, Garhwal Himalaya. *Geological Society of America Bulletin*, 112, 467-477.
- 1089 Ali, K.F., De Boer, D.H., 2007. Spatial patterns and variation of suspended sediment yield in the  
1090 upper Indus River basin, northern Pakistan. *Journal of Hydrology*, 334, 368-387.
- 1091 Ali, K.F., De Boer, D.H., 2008. Factors controlling specific sediment yield in the upper Indus River  
1092 basin, northern Pakistan. *Hydrological Processes*, 22, 3102-3114.
- 1093 Alizai, A., Carter, A., Clift, P.D., Van Laningham, S., Williams, J.C., Kumar, R., 2011. Sediment  
1094 provenance, reworking and transport processes in the Indus River by U–Pb dating of detrital zircon  
1095 grains. *Global and Planetary Change*, 76, 33-55.
- 1096 Alizai, A., Clift, P.D., Still, J., 2016. Indus Basin sediment provenance constrained using garnet  
1097 geochemistry. *Journal of Asian Earth Sciences*, 126, 29-57.
- 1098 Andò, S., Garzanti, E., 2014. Raman spectroscopy in heavy-mineral studies. In: Scott, R.A., Smyth,  
1099 H.R., Morton, A.C., Richardson, N. (Eds.), *Sediment Provenance Studies in Hydrocarbon  
1100 Exploration and Production*. Geological Society: London, UK, Special Publication 386, pp. 395-  
1101 412.
- 1102 Andò, S., Aharonovich, S., Hahn, A., George, S.C., Clift, P.D., Garzanti, E., 2019. Integrating  
1103 heavy-mineral, geochemical, and biomarker analyses of Plio-Pleistocene sandy and silty turbidites:  
1104 a novel approach for provenance studies (Indus Fan, IODP Expedition 355). *Geological Magazine*,  
1105 <https://doi.org/10.1017/S0016756819000773>
- 1106 Argles, T., Foster, G., Whittington, A., Harris, N., George, M., 2003. Isotope studies reveal a  
1107 complete Himalayan section in the Nanga Parbat syntaxis. *Geology*, 31(12), 1109-1112.
- 1108 Badshah, M.S., Gnos, E., Jan, M.Q., Afridi, M.I., 2000. Stratigraphic and tectonic evolution of the  
1109 northwestern Indian plate and Kabul Block. Geological Society, London, Special Publications,  
1110 170, 467-476.
- 1111 Beck, R.A., Burbank, D.W., Sercombe, W.J., Riley, G.W., Barndt, J.K., Berry, J.R., Afzal, J.,  
1112 Khan, A.M., Jurgen, H., Metje, J., Cheema, A., Shafique, N.A., Lawrence, R.D., Khan, M.A.,  
1113 1995. Stratigraphic evidence for an early collision between Northwest India and Asia. *Nature*,  
1114 373 (6509), 55-58.

- 1115 Biagi, P., Starnini, E., Ghauri, Z.S., 2019. Mahi Wala 1 (MW-1): a Mesolithic site in the Thal desert  
 1116 of Punjab (Pakistan). *Asian Archaeology*, <https://doi.org/10.1007/s41826-019-00024-z>.  
 1117
- 1118 Blöthe, J.H., Munack, H., Korup, O., Fülling, A., Garzanti, E., Resentini, A., Kubik, P.W., 2014.  
 1119 Late Quaternary valley infill and dissection in the Indus River, western Tibetan Plateau margin.  
 1120 *Quaternary Science Reviews*, 94, 102-119.  
 1121
- 1122 Borromeo, L., Andò, S., France-Lanord, C., Coletti, G., Hahn, A., Garzanti, E., 2019. Provenance  
 1123 of Bengal Shelf Sediments: 1. Mineralogy and Geochemistry of Silt. *Minerals*, 9, 640,  
 1124 doi:10.3390/min9100640.  
 1125
- 1126 Burbank, D.W., Leland, J., Fielding, E., Anderson, R.S., Brozovic, N., Reid, M.R., Duncan, C.,  
 1127 1996a. Bedrock incision, rock uplift and threshold hillslopes in the northwestern Himalayas.  
 1128 *Nature*, 379, 505-510.  
 1129
- 1130 Burbank, D.W., Beck, R.A., Mulder, T., 1996b. The Himalayan foreland basin. In: Yin, A.,  
 1131 Harrison, T.M. (Eds.), *The Tectonic Evolution of Asia (World and regional geology)*. Cambridge  
 1132 University Press, Cambridge, UK, pp.149-188.  
 1133
- 1134 Burg, J.P., 2011. The Asia–Kohistan–India collision: review and discussion. In: Brown, D., Ryan,  
 1135 P.D. (Eds.), *Arc-Continent Collision, Frontiers in Earth Sciences*, Springer Berlin Heidelberg,  
 1136 pp. 279-309.  
 1137
- 1138 Cervený, P.F., Johnson, N.M., Tahirkheli, R.A.K., Bonis, N.R., 1989. Tectonic and geomorphic  
 1139 implications of Siwalik group heavy minerals, Potwar plateau, Pakistan. In: Malinconico, L.L.,  
 1140 Lillie, R.J. (Eds.), *Tectonics of the Western Himalayas*. Geological Society of America, Special  
 1141 Papers, 232, pp. 129-136.  
 1142
- 1143 Chirouze, F., Huyghe, P., Chauvel, C., van der Beek, P., Bernet, M., Mugnier, J.-L., 2015. Stable  
 1144 drainage pattern and variable exhumation in the Western Himalaya since the Middle Miocene.  
 1145 *The Journal of Geology*, 123, 1-20, doi.org/10.1086/679305.  
 1146
- 1147 Clift, P.D., 2017. Cenozoic sedimentary records of climate-tectonic coupling in the Western  
 1148 Himalaya. *Progress in Earth and Planetary Science*, 4, 39, doi10.1186/s40645-017-0151-8.  
 1149
- 1150 Clift, P.D., Giosan, L., 2014. Sediment fluxes and buffering in the post-glacial Indus Basin. *Basin  
 1151 Research*, 26, 369-386, doi:10.1111/bre.12038.  
 1152

- 1143 Clift, P., Shimizu, N., Layne, G., Gaedicke, C., Schlter, H.U., Clark, M., Amjad, S., 2000. Fifty-five  
1144 million years of Tibetan evolution recorded in the Indus Fan. *Eos, Transactions American*  
1145 *Geophysical Union*, 81, 277-281.  
1146  
1147 Clift, P.D., Shimizu, N., Layne, G., Blusztajn, J.S., Gaedicke, C., Schluter, H.-U., Clark, M.K.,  
1148 Amjad, S., 2001. Development of the Indus Fan and its significance for the erosional history of  
1149 the Western Himalaya and Karakoram. *Geological Society of America Bulletin*, 113, 1039-1051.  
1150  
1151 Clift, P.D., Lee, J.I., Hildebrand, P., Shimizu, N., Layne, G.D., Blusztajn, J., Blum, J.D., Garzanti,  
1152 E., Khan, A.A., 2002. Nd and Pb isotope variability in the Indus River System: implications for  
1153 sediment provenance and crustal heterogeneity in the Western Himalaya. *Earth and Planetary*  
1154 *Science Letters*, 200(1-2), 91-106.  
1155  
1156 Clift, P.D., Campbell, I.H., Pringle, M.S., Carter, A., Zhang, X., Hodges, K.V., Khan, A.A., Allen,  
1157 C.M., 2004. Thermochronology of the modern Indus River bedload: New insight into the  
1158 controls on the marine stratigraphic record. *Tectonics*, 23(5), doi:10.1029/2003TC001559.  
1159  
1160 Clift, P., Giosan, L., Blusztajn, J., Campbell, I.H., Allen, C., Pringle, M., Tabrez, A.R., Danish, M.,  
1161 Rabbani, M.M., Alizai, A., Carter, A., Lückge, A., 2008. Holocene erosion of the Lesser  
1162 Himalaya triggered by intensified summer monsoon. *Geology*, 36, 79-82, doi:  
1163 10.1130/G24315A.1.  
1164  
1165 Clift P.D., Giosan L., Carter A., Garzanti E., Galy V., Tabrez A.R., Pringle M., Campbell I.H.,  
1166 France-Lanord C., Blusztajn J., Allen C., Alizai A., Lückge A., Danish M., Rabbani M.M.,  
1167 2010. Monsoon control over erosion patterns in the Western Himalaya: possible feed-backs into  
1168 the tectonic evolution. In: Clift P.D., Tada R. and Zheng H. (Eds.), *Monsoon evolution and*  
1169 *tectonic-climate linkage in Asia*, Geological Society London, Special Publication 342, pp. 185-  
1170 218.  
1171  
1172 Clift, P.D., Carter, A., Giosan, L., Durcan, J., Duller, G.A., Macklin, M.G., Alizai, A., Tabrez, A.R.,  
1173 Danish, M., Van Laningham, S., Fuller, D.Q., 2012. U-Pb zircon dating evidence for a  
1174 Pleistocene Sarasvati River and capture of the Yamuna River. *Geology*, 40(3), 211-214.  
1175  
1176 Clift, P.D., Zhou, P., Stockli, D.F., Blusztajn, J., 2019. Regional Pliocene exhumation of the Lesser  
1177 Himalaya in the Indus drainage. *Solid Earth*, 10, 647-661.  
1178  
1179 Comas-Cufí, M., Thió-Henestrosa, F.S., 2011. CoDaPack 2.0: a stand-alone, multi-platform  
1180 compositional software.

- 1173 Cottle, J., Lederer, G., Larson, K., 2019. The monazite record of pluton assembly: Mapping  
 1174 Manaslu using petrochronology, *Chemical Geology*, 530, 119309,  
 1175 <https://doi.org/10.1016/j.chemgeo.2019.119309>.  
 1176  
 1177 Crawford, M.B., Searle, M.P., 1992. Field relationships and geochemistry of pre-collisional (India-  
 1178 Asia) granitoid magmatism in the central Karakoram, northern Pakistan. *Tectonophysics*, 206,  
 1179 171-192.  
 1180 Critelli, S., Garzanti, E., 1994. Provenance of the Lower Tertiary Murree redbeds (Hazara-Kashmir  
 1181 syntaxis, Pakistan) and initial rising of the Himalayas. *Sedimentary Geology*, 89, 265-284.  
 1182 Critelli, S., Ingersoll, R.V., 1994. Sandstone petrology and provenance of the Siwalik Group  
 1183 (northwestern Pakistan and western-southeastern Nepal). *Journal of Sedimentary Research*, A64,  
 1184 815-823.  
 1185 Critelli, S., De Rosa, R., Platt, J.P., 1990. Sandstone detrital modes in the Makran accretionary  
 1186 wedge, southwest Pakistan: Implications for tectonic setting and long-distance turbidite  
 1187 transportation. *Sedimentary Geology*, 68, 241-260.  
 1188 Debon, F., Le Fort, P., Dautel, D., Sonet, J., Zimmermann, J.L., 1987. Granites of western  
 1189 Karakorum and northern Kohistan (Pakistan): A composite Mid-Cretaceous to upper Cenozoic  
 1190 magmatism. *Lithos*, 20(1), 19-40.  
 1191 DeCelles, P., Gehrels, G.E., Quade, J., LaReau, B., Spurlin, M., 2000. Tectonic implications of U-  
 1192 Pb zircon ages of the Himalayan orogenic belt in Nepal. *Science*, 288, 497-499, doi:  
 1193 10.1126/science.288.5465.497.  
 1194 DePaolo, D.J., Wasserburg, G.J., 1976. Nd isotopic variations and petrogenetic models.  
 1195 *Geophysical Research Letters*, 3, 249-252.  
 1196 DiPietro, J.A., Pogue, K.R., 2004. Tectonostratigraphic subdivisions of the Himalaya: A view from  
 1197 the west. *Tectonics*, 23, TC5001, doi:10.1029/2003TC001554.  
 1198 Dixit, Y., Hodell, D.A., Petrie, C.A., 2014. Abrupt weakening of the summer monsoon in northwest  
 1199 India ~4100 yr ago. *Geology*, 42(4), 339-342, doi:10.1130/G35236.1.  
 1200 Dhir, R.P., Singhvi, A.K., Andrews, J.E., Kar, A., Sareen, B.K., Tandon, S.K., Kailath, A., Thomas,  
 1201 J.V., 2010. Multiple episodes of aggradation and calcrete formation in late Quaternary aeolian  
 sands, central Thar Desert, Rajasthan, India. *Journal of Asian Earth Sciences*, 37, 10-16.



- 1202 Downing, K.F., Lindsay, E.H., 2005. Relationship of Chitarwata Formation paleodrainage and  
1203 paleoenvironments to Himalayan tectonics and Indus River paleogeography. *Palaeontologia*  
1204 *Electronica*, 8, 1; 20A, 12 p.  
4
- 1205 East, A.E., Clift, P.D., Carter, A., Alizai, A., Van Laningham, S., 2015. Fluvial-eolian interactions  
1206 in sediment routing and sedimentary signal buffering: an example from the Indus Basin and Thar  
1207 Desert. *Journal of Sedimentary Research*, 85, 715-728.  
7
- 1208 Enzel, Y., Ely, L.L., Mishra, S., Ramesh, R., Amit, R., Lazar, B., Rajaguru, S.N., Baker, V.R.,  
1209 Sandler, A., 1999. High-resolution Holocene environmental changes in the Thar Desert,  
1210 northwestern India. *Science*, 284, 125-128.  
15
- 1211 Fraser, J.E., Searle, M.P., Parrish, R.R., Noble, S.R., 2001. Chronology of deformation,  
1212 metamorphism, and magmatism in the southern Karakoram Mountains. *Geological Society of*  
1213 *America Bulletin*, 113 (11), 1443-1455-  
23
- 1214 Gabriel, K.R., 1971. The biplot graphic display of matrices with application to principal component  
1215 analysis. *Biometrika*, 58, 453-467.  
27
- 1216 Gaetani, M., Garzanti, E., Jadoul, F., Nicora, A., Tintori, A., Pasini, M., Kanwar, S.A.K., 1990, The  
1217 north Karakorum side of the Central Asia geopuzzle. *Geological Society of America Bulletin*,  
1218 102, 54-62.  
34
- 1219 Galehouse, J.S., 1971. Point counting, In: Carver, R.E. (ed.), *Procedures in sedimentary petrology*,  
1220 New York, Wiley, pp. 385-407.  
38
- 1221 Garçon, M., Chauvel, C., France-Lanord, C., Limonta, M., Garzanti, E., 2014. Which minerals  
1222 control the Nd-Hf-Sr-Pb isotopic compositions of river sediments? *Chemical Geology*, 364, 42-  
1223 55.  
45
- 1224 Garzanti, E., 2016. From static to dynamic provenance analysis—Sedimentary petrology upgraded.  
1225 *Sedimentary Geology*, 336, 3-13.  
49
- 1226 Garzanti, E., 2017, The maturity myth in sedimentology and provenance analysis. *Journal of*  
1227 *Sedimentary Research*, 87, 353-365.  
54
- 1228 Garzanti, E., 2019a. The Himalayan foreland basin from collision onset to the present: a  
1229 sedimentary-petrology perspective. In: Treloar, P., Searle, M.P. (Eds.), *Himalayan tectonics: a*  
1230 *modern synthesis*. Geological Society London, Special Publication 483, 65-122, doi.org:  
1231 10.1144/SP483.17  
60

- 1232 Garzanti, E., 2019b. Petrographic classification of sand and sandstone. *Earth-Science Reviews*, 192,  
1233 545-563.  
2
- 1234 Garzanti, E., Andò, S., 2019. Heavy Minerals for Junior Woodchucks. *Minerals*, 9, 148,  
1235 <https://doi.org/10.3390/min9030148>.  
3  
4  
5  
6  
7
- 1236 Garzanti, E., Resentini, A., 2016. Provenance control on chemical indices of weathering (Taiwan  
1237 river sands). *Sedimentary Geology*, 336, 81-95.  
8  
9  
10  
11
- 1238 Garzanti, E., Van Haver, T., 1988. The Indus clastics: forearc basin sedimentation in the Ladakh  
1239 Himalaya (India). *Sedimentary Geology*, 59(3-4), 237-249.  
12  
13  
14  
15  
16
- 1240 Garzanti, E., Vezzoli, G., 2003. A classification of metamorphic grains in sands based on their  
1241 composition and grade *Journal of Sedimentary Research*, 73, 830-837.  
17  
18  
19  
20  
21
- 1242 Garzanti, E., Casnedi, R., Jadoul, F., 1986. Sedimentary evidence of a Cambro-Ordovician orogenic  
1243 event in the northwestern Himalaya. *Sedimentary Geology*, 48, 237-265.  
22  
23  
24  
25
- 1244 Garzanti, E., Baud, A., Mascle, G., 1987. Sedimentary record of the northward flight of India and  
1245 its collision with Eurasia (Ladakh Himalaya, India). *Geodinamica Acta*, 1, 297-312.  
26  
27  
28  
29  
30
- 1246 Garzanti, E., Critelli, S., Ingersoll, R.V., 1996. Paleogeographic and paleotectonic evolution of the  
1247 Himalayan Range as reflected by detrital modes of Tertiary sandstones and modern sands (Indus  
1248 transect, India and Pakistan). *Geological Society of America Bulletin*, 108, 631-642.  
31  
32  
33  
34  
35  
36
- 1249 Garzanti, E., Vezzoli, G., Andò, S., Paparella, P., Clift, P.D., 2005. Petrology of Indus River sands:  
1250 a key to interpret erosion history of the Western Himalayan Syntaxis. *Earth and Planetary  
1251 Science Letters*, 229, 287-302.  
37  
38  
39  
40  
41  
42
- 1252 Garzanti, E., Andò, S., France-Lanord, C., Vezzoli, G., Najman, Y., 2010. Mineralogical and  
1253 chemical variability of fluvial sediments. 1. Bedload sand (Ganga-Brahmaputra, Bangladesh).  
1254 *Earth Planetary Science Letters*, 299, 368-381.  
43  
44  
45  
46  
47  
48  
49
- 1255 Garzanti, E., Andò, S., France-Lanord, C., Galy, V., Censi, P., Vignola, P., 2011. Mineralogical and  
1256 chemical variability of fluvial sediments. 2. Suspended-load silt (Ganga-Brahmaputra,  
1257 Bangladesh). *Earth and Planetary Science Letters*, 302, 107-120.  
50  
51  
52  
53  
54  
55
- 1258 Garzanti, E., Resentini, A., Vezzoli, G., Andò, S., Malusà, M., Padoan, M., 2012. Forward  
1259 compositional modelling of Alpine orogenic sediments. *Sedimentary Geology*, 280, 149-164.  
56  
57  
58  
59  
60  
61  
62  
63  
64  
65

- 1260 Garzanti, E., Vermeesch, P., Rittner, M. and Simmons, M., 2018. The zircon story of the Nile:  
 1261 Time- structure maps of source rocks and discontinuous propagation of detrital signals. *Basin*  
 1262 *Research*, 30(6), 1098-1117.
- 1263 Garzanti, E., Andò, S., France-Lanord, C., Limonta, M., Borromeo, L., Vezzoli, G., 2019.  
 1264 Provenance of Bengal Shelf Sediments. 2. Petrology of sand. *Minerals*, 9, 642;  
 1265 doi:10.3390/min9100642.
- 1266 Garzanti, E., Andò, S., Vezzoli, G., 2020. Provenance of Cenozoic Indus Fan sediments (IODP  
 1267 Sites U1456 and U1457). *Journal of Sedimentary Research*, in press.
- 1268 Gehrels, G.E., DeCelles, P.G., Martin, A., Ojha, T.P., Pinhassi, G., Upreti, B.N., 2003. Initiation of  
 1269 the Himalayan Orogen as an early Paleozoic thin-skinned thrust belt. *GSA Today*, 13(9), 4-9.
- 1270 Gehrels, G., Kapp, P., DeCelles, P., Pullen, A., Blakey, R., Weislogel, A., Ding, L., Guynn, J.,  
 1271 Martin, A., McQuarrie, N., Yin, A., 2011. Detrital zircon geochronology of pre- Tertiary strata  
 1272 in the Tibetan- Himalayan orogen. *Tectonics*, 30, TC5016, doi:10.1029/2011TC002868.
- 1273 Giosan, L., Constantinescu, S., Clift, P.D., Tabrez, A.R., Danish, M., Inam, A., 2006a. Recent  
 1274 morphodynamics of the Indus delta shore and shelf. *Continental Shelf Research*, 26, 1668-1684.
- 1275 Giosan, L., Clift, P.D., Blusztajn, J., Tabrez, A., Constantinescu, S., Filip, F., 2006b. On the control  
 1276 of climate- and human-modulated fluvial sediment delivery on river delta development: The  
 1277 Indus. *Eos, Transactions, American Geophysical Union*, 87, AGU Fall Meeting Abstracts,  
 1278 OS14A-04.
- 1279 Giosan, L., Clift, P.D., Macklin, M.G., Fuller, D.Q., Constantinescu, S., Durcan, J.A., Stevens, T.,  
 1280 Duller, G.A.T., Tabrez, A.R., Gangal, K., Adhikari, R., Alizai, A., Filip, F., Van Laningham, S.,  
 1281 Syvitski, J.P.M., 2012. Fluvial landscapes of the Harappan civilization. *Proceedings of the*  
 1282 *National Academy of Sciences*, 109, 1688-1694, doi/10.1073/pnas.1112743109.
- 1283 Gnos, E., Immenhauser, A., Peters, T.J., 1997. Late Cretaceous/early Tertiary convergence between  
 1284 the Indian and Arabian plates recorded in ophiolites and related sediments. *Tectonophysics*, 271,  
 1285 1-19.
- 1286 Goodbred, S.L., Kuehl, S.A., 2000. Enormous Ganges-Brahmaputra sediment discharge during  
 1287 strengthened early Holocene monsoon. *Geology*, 28, 1083-1086.
- 1288 Gosal, G., 2004. Physical geography of the Punjab. *Journal of Punjab Studies*, 11, 19-37.

- 1289 Greenman, D.W., Swarzenski, W.V., Bennett, G.D., 1967. Ground-water hydrology of the Punjab,  
 1290 West Pakistan, with emphasis on problems caused by canal irrigation. United States Government  
 2  
 1291 Printing Office, Washington, United States Geological Survey, Water-supply paper 1608H, 1-  
 4  
 1292 66.  
 6
- 1293 Griffin, W.L., Powell, W.J., Pearson, N.J., O'Reilly, S.Y., 2008. GLITTER: data reduction software  
 8  
 1294 for laser ablation ICP–MS. In: Sylvester, P. (Ed.), Laser ablation–ICP–MS in the earth sciences:  
 10  
 1295 current practices and outstanding issues. Mineralogical Association of Canada, Short Course 40,  
 12  
 1296 pp. 204-207.  
 14
- 1297 Hamilton, P.J., O'Nions, R.K., Bridgwater, D., Nutman, A.P., 1983. Sm-Nd studies of Archaean  
 16  
 1298 metasediments and metavolcanics from west Greenland and their implications for the Earth's  
 18  
 1299 early history. *Earth and Planetary Science Letters*, 62, 263-272.  
 20
- 1300 Henderson, A.L., Najman, Y., Parrish, R., BouDagher- Fadel, M., Barford, D., Garzanti, E., Andò,  
 23  
 1301 S., 2010. Geology of the Cenozoic Indus Basin sedimentary rocks: Paleoenvironmental  
 25  
 1302 interpretation of sedimentation from the western Himalaya during the early phases of  
 26  
 1303 India- Eurasia collision. *Tectonics*, 29(6), TC6015, doi:10.1029/2009TC002651.  
 28
- 1304 Hildebrand, P.R., Noble, S.R., Searle, M.P., Waters, D.J., Parrish, R.R., 2001. Old origin for an  
 31  
 1305 active mountain range: Geology and geochronology of the eastern Hindu Kush, Pakistan.  
 33  
 1306 *Geological Society of America Bulletin*, 113, 625-639.  
 35
- 1307 Hu, X., Garzanti, E., Moore, T., Raffi, I., 2015. Direct stratigraphic dating of India-Asia collision  
 37  
 1308 onset at the Selandian (middle Paleocene, 59±1 Ma). *Geology*, 43(10), 859-862.  
 39
- 1309 Hubert, J.F., 1962. A zircon–tourmaline–rutile maturity index and the interdependence of the  
 42  
 1310 composition of heavy minerals assemblages with the gross composition and texture of  
 44  
 1311 sandstones. *Journal of Sedimentary Petrology*, 32, 440-450.  
 46
- 1312 Hussain, A., Mir, H., Afzal, M., 2005. Analysis of dust storms frequency over Pakistan during  
 48  
 1313 1961-2000. *Pakistan Journal of Meteorology*, 2, 49-68.  
 50
- 1314 Hussain, Y., Ullah, S.F., Hussain, M.B., Aslam, A.Q., Akhter, G., Martinez-Carvajal, H., Cárdenas-  
 53  
 1315 Soto, M., 2017. Modelling the vulnerability of groundwater to contamination in an unconfined  
 55  
 1316 alluvial aquifer in Pakistan. *Environmental Earth Sciences*, 76, 84, doi:10.1007/s12665-017-  
 56  
 1317 6391-5.  
 58
- 59  
 60  
 61  
 62  
 63  
 64  
 65

- 1318 Ingersoll, R.V., Bullard, T.F., Ford, R.L., Grimm, J.P., Pickle, J.D., Sares, S.W., 1984. The effect of  
 1319 grain size on detrital modes: a test of the Gazzi-Dickinson point-counting method. *Journal of*  
 1320 *Sedimentary Petrology*, 54, 103-116.  
 1321
- 1321 Jadoon, I.A., Lawrence, R.D., Lillie, R.J., 1994. Seismic data, geometry, evolution, and shortening  
 1322 in the active Sulaiman fold-and-thrust belt of Pakistan, southwest of the Himalayas. *American*  
 1323 *Association of Petroleum Geologists Bulletin*, 78, 758-774.  
 1324
- 1324 Jagoutz, O.E., Burg, J.P., Hussain, S., Dawood, H., Pettke, T., Iizuka, T., Maruyama, S., 2009.  
 1325 Construction of the granitoid crust of an island arc part I: geochronological and geochemical  
 1326 constraints from the plutonic Kohistan (NW Pakistan). *Contributions to Mineralogy and*  
 1327 *Petrology*, 158, 739-755.  
 1328
- 1328 Jagoutz, O., Bouilhol, P., Schaltegger, U., Müntener, O., 2019. The isotopic evolution of the  
 1329 Kohistan Ladakh arc from subduction initiation to continent arc collision. In: Treloar, P.J.,  
 1330 Searle, M.P. (Eds.), *Himalayan Tectonics: A Modern Synthesis*. Geological Society, London,  
 1331 *Special Publications*, 483, 165-182.  
 1332
- 1332 Jipa, D., Kidd, R.B., 1974. Sedimentation of coarser grained interbeds in the Arabian Sea and  
 1333 sedimentation processes of the Indus Cone. In: Whitmarsh, R.B., Weser, O.E., Ross, D.A., et  
 1334 al. (Eds.), *Initial Report of the Deep Sea Drilling Project 219-230*. Washington, D.C., US  
 1335 *Government Printing Office*, pp. 471-495.  
 1336
- 1336 Jonell, T.N., Carter, A., Böning, P., Pahnke, K., Clift, P.D., 2017a. Climatic and glacial impact on  
 1337 erosion patterns and sediment provenance in the Himalayan rain shadow, Zaskar River, NW  
 1338 India. *Geological Society of America Bulletin*, 129, 820-836.  
 1339
- 1339 Jonell, T.N., Owen, L.A., Carter, A., Schwenniger, J. L., Clift, P.D., 2017b. Quantifying episodic  
 1340 erosion and transient storage on the western margin of the Tibetan Plateau, upper Indus River.  
 1341 *Quaternary Research*, 89(1), 281-306.  
 1342
- 1342 Jonell, T.N., Li, Y., Blusztajn, J., Giosan, L., Clift, P.D., 2018. Signal or noise? Isolating grain size  
 1343 effects on Nd and Sr isotope variability in Indus delta sediment provenance. *Chemical Geology*,  
 1344 485, 56-73.  
 1345
- 1345 Kadri, I.B., 1995. *Petroleum Geology of Pakistan*. Pakistan Petroleum Limited (275 pp.).  
 1346
- 1346 Khan, I.A., Bridge, J.S., Kappelman, J., Wilson, R., 1997a. Evolution of Miocene fluvial  
 1347 environments, eastern Potwar plateau, northern Pakistan. *Sedimentology*, 44, 221-251.  
 1348  
 1349  
 1350  
 1351  
 1352  
 1353  
 1354  
 1355  
 1356  
 1357  
 1358  
 1359  
 1360  
 1361  
 1362  
 1363  
 1364  
 1365

- 1348 Khan, M.A., Stern, R.J., Gribble, R.F., Windley, B.F., 1997b. Geochemical and isotopic constraints  
 1349 on subduction polarity, magma sources and palaeogeography of the Kohistan intra-oceanic arc,  
 1350 northern Pakistan Himalayas. *Journal of the Geological Society, London*, 154, 935-946.  
 1351  
 1352 Kruskal, J., 1964. Multidimensional scaling by optimizing goodness of fit to a nonmetric  
 1353 hypothesis. *Psychometrika*, 29, 1-27.  
 1354  
 1355 Lee, J.I., Clift, P.D., Layne, G., Blum, J., Khan, A.A., 2003. Sediment flux in the modern Indus  
 1356 River inferred from the trace element composition of detrital amphibole grains. *Sedimentary  
 1357 Geology*, 160, 243-257.  
 1358  
 1359 Li, Y., Clift, P.D., O'Sullivan, P., 2019. Millennial and centennial variations in zircon U- Pb ages in  
 1360 the Quaternary Indus submarine canyon. *Basin Research*, 31, 155-170.  
 1361  
 1362 Liang, W., Garzanti, E., Andò, S., Gentile, P., Resentini, A., 2019. Multimineral fingerprinting of  
 1363 Transhimalayan and Himalayan sources to Indus-derived Thal Desert sand (central Pakistan).  
 1364 *Minerals*, 9, 457, doi:10.3390/min9080457.  
 1365  
 1366 Lünsdorf, N.K., Kalies, J., Ahlers, P., Dunkl, I., von Eynatten, H., 2019. Semi-automated heavy-  
 1367 mineral analysis by Raman spectroscopy. *Minerals*, 9, 385, doi.org/10.3390/min9070385.  
 1368  
 1369 Lupker, M., France-Lanord, C., Galy, V., Lavé, J., Kudrass, H., 2013. Increasing chemical  
 1370 weathering in the Himalayan system since the Last Glacial Maximum. *Earth and Planetary  
 1371 Science Letters*, 365, 243-252.  
 1372  
 1373 Mahar, M.A., Mahéo, G., Goodell, P.C., Pavlis, T.L., 2014. Age and origin of post collision Baltoro  
 1374 granites, south Karakoram, North Pakistan: Insights from in-situ U–Pb, Hf and oxygen isotopic  
 1375 record of zircons. *Lithos*, 205, 341-358.  
 1376  
 1377 Mahéo, G., Blichert-Toft, J., Pin, C., Guillot, S., Pêcher, A., 2009. Partial melting of mantle and  
 1378 crustal sources beneath South Karakorum, Pakistan: Implications for the Miocene geodynamic  
 1379 evolution of the India–Asia convergence zone. *Journal of Petrology*, 50, 427-449.  
 1380  
 1381 Mallik, T.K., 1978, Mineralogy of deep-sea sands of the Indian Ocean. *Marine Geology*, 27, 161-  
 1382 176.  
 1383  
 1384 Malusà, M.G., Resentini, A., Garzanti, E., 2016. Hydraulic sorting and mineral fertility bias in  
 1385 detrital geochronology. *Gondwana Research*, 31, 1-19.  
 1386  
 1387 Mange, M.A., Maurer, H.F.W., 1992, Heavy minerals in colour. Chapman and Hall, London. (147  
 1388 pp.).

- 1378 Mange, M.A., Morton, A.C., 2007. Geochemistry of heavy minerals. In: Mange, M.A., Wright,  
 1379 D.T. (Eds.), *Heavy Minerals in Use*. Elsevier, Amsterdam, *Developments in Sedimentology*, 58,  
 1380 pp. 345-391.  
 1381
- 1381 Meadows, A., Meadows, P., 1999. *The Indus River: Biodiversity, Resources, Humankind*. Oxford  
 1382 University Press (441 pp.).  
 1383
- 1383 Miller, C., Klötzli, U., Frank, W., Thöni, M., Grasemann, B., 2000. Proterozoic crustal evolution in  
 1384 the NW Himalaya (India) as recorded by circa 1.80 Ga mafic and 1.84 Ga granitic magmatism.  
 1385 *Precambrian Research*, 103(3-4), 191-206.  
 1386
- 1386 Miller, C., Thöni, M., Frank, W., Grasemann, B., Klötzli, U., Guntli, P., Draganits, E., 2001. The  
 1387 early Palaeozoic magmatic event in the Northwest Himalaya, India: source, tectonic setting and  
 1388 age of emplacement. *Geological Magazine*, 138(3), 237-251.  
 1389
- 1389 Milliman, J.D., Quraishee, G.S. Beg, M.A.A., 1984. Sediment discharge from the Indus River to the  
 1390 ocean: past, present, and future. In: Haq, B.U., Milliman, J.D. (Eds.), *Marine Geology and*  
 1391 *Oceanography of the Arabian Sea and Coastal Pakistan*. Van Nostrand Reynolds, New York, pp.  
 1392 65-70.  
 1393
- 1393 Munack, H., Korup, O., Resentini, A., Limonta, M., Garzanti, E., Blöthe, J.H., Scherler, D.,  
 1394 Wittmann, H., Kubik, P.W., 2014. Postglacial denudation of western Tibetan Plateau margin  
 1395 outpaced by long-term exhumation. *Geological Society of America Bulletin*, 126, 1580-1594.  
 1396
- 1396 Najman, Y., Garzanti, E., Pringle, M., Bickle, M., Stix, J., Khan, I., 2003. Early-Middle Miocene  
 1397 paleodrainage and tectonics in the Pakistan Himalaya. *Geological Society of America Bulletin*,  
 1398 115, 1265-1277.  
 1399
- 1399 Nickson, R.T., McArthur, J.M., Shrestha, B., Kyaw-Myint, T.O., Lowry, D., 2005. Arsenic and  
 1400 other drinking water quality issues, Muzaffargarh District, Pakistan. *Applied Geochemistry*, 20,  
 1401 55-68.  
 1402
- 1402 Pandey, D.K., Clift, P.D., Kulhanek, D.K. & Expedition 355 Scientists, 2016. Expedition 355  
 1403 summary. *Arabian Sea Monsoon*. In: Pandey, D.K., Clift, P.D., Kulhanek, D.K. & Expedition  
 1404 355 Scientists (Eds.), *Expedition 355 Scientific Prospectus: Arabian Sea Monsoon*. Proceedings  
 1405 of the International Ocean Discovery Program, Volume 355. International Ocean Discovery  
 1406 Program, College Station, TX, 1-32, <https://doi.org/10.14379/iodp.proc.355.101.2016>.



- 1407 Parrish, R.R., Hodges, V., 1996. Isotopic constraints on the age and provenance of the Lesser and  
 1408 Greater Himalayan sequences, Nepalese Himalaya. *Geological Society of America Bulletin*, 108,  
 1409 904-911.  
 1410
- 1410 Pêcher, A., Seeber, L., Guillot, S., Jouanne, F., Kausar, A., Latif, M., Majid, A., Mahéo, G.,  
 1411 Mugnier, J.L., Rolland, Y., van der Beek, P., Van Melle, J., 2008. Stress field evolution in the  
 1412 northwest Himalayan syntaxis, northern Pakistan. *Tectonics*, 27, TC6005,  
 1413 doi:10.1029/2007TC002252.  
 1414
- 1414 Petterson, M.G., M.B. Crawford, B.F. Windley, 1993. Petrogenetic implications of neodymium  
 1415 isotope data from the Kohistan Batholith, North Pakistan, *Journal of the Geological Society*,  
 1416 London, 150, 125-129.  
 1417
- 1417 Prasad, B.R., Klemperer, S.L., Rao, V.V., Tewari, H.C., Khare, P., 2011. Crustal structure beneath  
 1418 the Sub-Himalayan fold–thrust belt, Kangra recess, northwest India, from seismic reflection  
 1419 profiling: Implications for Late Paleoproterozoic orogenesis and modern earthquake hazard.  
 1420 *Earth and Planetary Science Letters*, 308(1-2), 218-228.  
 1421
- 1421 Prasad, S., Enzel, Y., 2006. Holocene palaeoclimates of India. *Quaternary Research*, 66, 442-453.  
 1422
- 1422 Qayyum, M., Lawrence, R.D., Niem, A.R., 1997. Discovery of the palaeo-Indus delta-fan complex.  
 1423 *Journal of the Geological Society London*, 154, 753-756, doi: 10.1144/gsjgs.154.5.0753.  
 1424
- 1424 Ravikant, V., Wu, F.Y., Ji, W.Q., 2009. Zircon U–Pb and Hf isotopic constraints on petrogenesis of  
 1425 the Cretaceous–Tertiary granites in eastern Karakoram and Ladakh, India. *Lithos*, 110(1-4), 153-  
 1426 166.  
 1427
- 1427 Rehman, S.S., Sabir, M.A., Khan, J., 1997. Discharge characteristics and suspended load from  
 1428 rivers of Northern Indus Basin, Pakistan. *Geological Bulletin University of Peshawar*, 30, 325-  
 1429 336.  
 1430
- 1430 Resentini, A., Goren, L., Castelltort, S., Garzanti, E., 2017. Partitioning the sediment flux by  
 1431 provenance and tracing erosion patterns in Taiwan. *Journal Geophysical Research - Earth  
 1432 Surface*, 122, 1430-1454, doi:10.1002/2016JF004026.  
 1433
- 1433 Roddaz, M., Said, A., Guillot, S., Antoine, P.O., Montel, J.M., Martin, F., Darrozes, J., 2011.  
 1434 Provenance of Cenozoic sedimentary rocks from the Sulaiman fold and thrust belt, Pakistan:  
 1435 implications for the palaeogeography of the Indus drainage system. *Journal of the Geological  
 1436 Society*, 168, 499-516.  
 1437

- 1437 Rolland, Y., Mahéo, G., Guillot, S., Pêcher, A., 2001. Tectono-metamorphic evolution of the  
1438 Karakorum metamorphic complex (Dassu-Askole area, NE Pakistan): exhumation of mid-crustal  
2 HT–MP gneisses in a convergent context. *Journal of Metamorphic Geology*, 19, 717-737.  
1439  
4
- 1440 Rolland, Y., Picard, C., Pêcher, A., Lapierre, H., Bosch, D., Keller, F., 2002. The Cretaceous  
1441 Ladakh arc of NW Himalaya—slab melting and melt-mantle interaction during fast northward  
7 drift of Indian Plate. *Chemical Geology*, 182, 139-178.  
1442  
10
- 1443 Roy, P.D., Nagar, Y.C., Juyal, N., Smykatz-Kloss, W., Singhvi, A.K., 2009. Geochemical  
1444 signatures of Late Holocene paleohydrological changes from Phulera and Pokharan saline playas  
13 near the eastern and western margins of the Thar Desert, India. *Journal of Asian Earth Sciences*  
1445 34, 275-286.  
1446  
18
- 1447 Rudnick, R.L., Gao, S., 2003. Composition of the continental crust. In: Rudnick, R.L., Holland,  
21 H.D., Turekian, K.K. (Eds.), *Treatise on Geochemistry, The Crust*. Elsevier Pergamon, Oxford,  
22 UK, Vol. 3, pp. 1–64.  
23  
24
- 1450 Schärer, U., Copeland, P., Harrison, T. M., Searle, M.P., 1990. Age, cooling history, and origin of  
27 post-collisional leucogranites in the Karakoram Batholith; a multi-system isotope study. *The  
1451 Journal of Geology*, 98(2), 233-251.  
29  
30
- 1453 Schaltegger, U., Zeilinger, G., Frank, M., Burg, J.P., 2002. Multiple mantle sources during island  
34 arc magmatism: U–Pb and Hf isotopic evidence from the Kohistan arc complex, Pakistan. *Terra  
1454 Nova*, 14(6), 461-468.  
35  
36
- 1456 Schneider, D.A., Zeitler, P.K., Kidd, W.S.F., Edwards, M.A., 2001. Geochronologic constraints on  
40 the tectonic evolution and exhumation of Nanga Parbat, western Himalaya syntaxis, revisited.  
1457 *The Journal of Geology*, 109, 563-583.  
42  
43
- 1459 Searle, M.P., 2013. *Colliding continents: a geological exploration of the Himalaya, Karakoram, and  
46 Tibet*. Oxford University Press, Oxford UK, 438 p.  
47  
48
- 1461 Searle, M.P., Khan, M.A., Fraser, J.E., Gough, S.J., Jan, M.Q., 1999. The tectonic evolution of the  
51 Kohistan- Karakoram collision belt along the Karakoram Highway transect, north Pakistan.  
1462 *Tectonics*, 18, 929-949.  
53  
54
- 1464 Searle, M.P., Parrish, R.R., Thow, A.V., Noble, S.R., Phillips, R.J., Waters, D.J., 2010. Anatomy,  
57 age and evolution of a collisional mountain belt: the Baltoro granite batholith and Karakoram  
1465  
59  
60  
61  
62  
63  
64  
65

- 1466 Metamorphic Complex, Pakistani Karakoram. *Journal of the Geological Society London*, 167,  
1467 183-202.  
2  
3
- 1468 Shah, S.M.I., 1977. Stratigraphy of Pakistan. Geological Survey of Pakistan, Memoir, 12, 138 p.  
4  
5
- 1469 Shah, Z.U.H., Ahmad, Z., 2015. Hydrochemical mapping of the Upper Thal Doab (Pakistan) using  
6  
7 the geographic information system. *Environmental Earth Sciences*, 74, 2757-2773.  
8  
9
- 1470  
10  
1471 Shah, Z.U.H., Ahmad, Z., 2016. Hydrogeology and hydrochemistry of the Upper Thal Doab  
11  
12 (Pakistan). *Environmental Earth Sciences*, 75(6), 527, doi: 10.1007/s12665-015-5211-z.  
13  
14
- 1473 Shroder, J.F., Bishop, M.P., 2000. Unroofing of Nanga Parbat Himalaya. In: Khan M.A., Treloar  
15  
16 P.J., Searle M.P., Jan M.Q. (Eds.), *Tectonics of the Nanga Parbat Syntaxis and the Western  
17  
18 Himalaya*. Geological Society, London, Special Publication, 170, pp. 163-179.  
19  
20
- 1475  
21  
1476 Singh, G., Wasson, R.J., Agrawal, D.P., 1990. Vegetational and seasonal climatic changes since the  
22  
23 last full glacial in the Thar Desert, northwestern India. *Review of Palaeobotany and  
24  
25 Palynology*, 64(1-4), 351-358.  
26  
27
- 1479 Singh, S., Kumar, R., Barley, M.E., Jain, A.K., 2007. SHRIMP U–Pb ages and depth of  
28  
29 emplacement of Ladakh Batholith, Eastern Ladakh, India. *Journal of Asian Earth Sciences*, 30(3-  
30  
31 4), 490-503.  
32  
33
- 1482 Singh, S., Jain, A.K., Barley, M.E., 2009. SHRIMP U-Pb c.1860 Ma anorogenic magmatic  
34  
35 signatures from the NW Himalaya: implications for Palaeoproterozoic assembly of the Columbia  
36  
37 Supercontinent. In: Reddy, S.M., Mazumder, R., Evans, D.A.D., Collins, A.S. (Eds.),  
38  
39 *Palaeoproterozoic Supercontinents and Global Evolution*. Geological Society, London, Special  
40  
41 Publications, 323, 283-300.  
42  
43
- 1484  
44  
1487 Singhvi, A. K., Kar, A., 2004. The aeolian sedimentation record of the Thar Desert. *Journal of Earth  
45  
46 System Science*, 113, 371-401.  
47  
48
- 1489 Singhvi, A.K., Williams, M.A.J., Rajaguru, S.N., Misra, V.N., Chawla, S., Stokes, S., Chauhan, N.,  
49  
50 Francis, T., Ganjoo, R.K., Humphreys, G.S., 2010. A ~200 ka record of climatic change and  
51  
52 dune activity in the Thar Desert, India. *Quaternary Science Reviews*, 29, 3095-3105.  
53  
54
- 1492 Staubwasser, M., Sirocko, F., Grootes, P.M., Erlenkeuser, H., 2002. South Asian monsoon climate  
55  
56 change and radiocarbon in the Arabian Sea during early and middle Holocene.  
57  
58 *Paleoceanography*, 17(4), 1063, doi:10.1029/2000PA000608.  
59  
60  
61  
62  
63  
64  
65

- 1495 St-Onge, M.R., Rayner, N., Searle, M.P., 2010. Zircon age determinations for the Ladakh batholith  
1496 at Chumathang (Northwest India): Implications for the age of the India–Asia collision in the  
1497 Ladakh Himalaya. *Tectonophysics*, 495(3-4), 171-183.
- 1498 Suczek, C.A., Ingersoll, R.V., 1985. Petrology and provenance of Cenozoic sand from the Indus  
1499 Cone and the Arabian Basin, DSDP sites 221, 222, and 224. *Journal of Sedimentary  
1500 Petrology*, 55(3), 340-346.
- 1501 Tate, E.L., Farquharson, F.K., 2000. Simulating reservoir management under the threat of  
1502 sedimentation: The case of Tarbela Dam on the River Indus. *Water Resources Management*, 14  
1503 191-208.
- 1504 Taylor, S.R., McLennan, S.M., 1995. The geochemical evolution of the continental crust. *Review of  
1505 Geophysics*, 33, 241–265.
- 1506 Treloar, P.J., Petterson, M.G., Jan, M.Q., Sullivan, M.A., 1996. A re-evaluation of the stratigraphy  
1507 and evolution of the Kohistan arc sequence, Pakistan Himalaya: implications for magmatic and  
1508 tectonic arc-building processes. *Journal of the Geological Society London*, 153, 681-693.
- 1509 Vermeesch, P., 2012. On the visualisation of detrital age distributions. *Chemical Geology*, 312,  
1510 190-194.
- 1511 Vermeesch, P., 2013. Multi-sample comparison of detrital age distributions. *Chemical Geology*,  
1512 341, 140-146.
- 1513 Vermeesch, P., 2018. Dissimilarity measures in detrital geochronology. *Earth-Science Reviews*,  
1514 178, 310-321.
- 1515 Vermeesch, P., Garzanti, E., 2015. Making geological sense of ‘Big Data’ in sedimentary  
1516 provenance analysis. *Chemical Geology*, 409, 20-27.
- 1517 Vermeesch, P., Resentini, A., Garzanti, E., 2016. An R package for statistical provenance analysis.  
1518 *Sedimentary Geology*, 336, 14-25.
- 1519 Vermeesch, P., Rittner, M., Petrou, E., Omma, J., Mattinson, C., Garzanti, E., 2017. High  
1520 throughput petrochronology and sedimentary provenance analysis by automated phase mapping  
1521 and LAICPMS. *Geochemistry, Geophysics, Geosystems*, 18, 4096-4109, doi:  
1522 10.1002/2017GC007109.

- 1523 Von Eynatten, H., Pawlowsky-Glahn, V., Egozcue, J.J., 2002. Understanding perturbation on the  
 1524 simplex: A simple method to better visualize and interpret compositional data in ternary  
 2  
 1525 diagrams. *Mathematical Geology*, 34(3), 249-257.  
 4
- 1526 Weinberg, R.F., Dunlap, W.J., 2000. Growth and deformation of the Ladakh Batholith, Northwest  
 5  
 1527 Himalayas: implications for timing of continental collision and origin of calc-alkaline batholiths.  
 6  
 7  
 8  
 1528 *The Journal of Geology*, 108, 303-320.  
 10
- 1529 Whittington, A., Foster, G., Harris, N., Vance, D., Ayres, M., 1999. Lithostratigraphic correlations  
 11  
 1530 in the western Himalaya; an isotopic approach. *Geology* 27, 585-588.  
 12  
 13  
 14  
 15
- 1531 Whittington, A., Harris, N.B.W., Ayres, M.W., Foster, G., 2000. Tracing the origins of the western  
 16  
 1532 Himalaya: an isotopic comparison of the Nanga Parbat massif and Zaskar Himalaya. In: Khan,  
 17  
 18  
 19  
 20  
 21  
 22  
 23  
 24  
 25  
 26  
 27  
 28  
 29  
 30  
 31  
 32
- 1533 M.A., Treloar, P.J., Searle, M.P., Jan, M.Q. (Eds.), *Tectonics of the Nanga Parbat Syntaxis and  
 33  
 34  
 35  
 36  
 37  
 38  
 39  
 40  
 41  
 42  
 43  
 44  
 45  
 46  
 47  
 48  
 49  
 50  
 51  
 52  
 53  
 54  
 55  
 56  
 57  
 58  
 59  
 60  
 61  
 62  
 63  
 64  
 65*
- 1539 Zeidler, P.K., Chamberlain, C.P., Smith, H.A., 1993. Synchronous anatexis, metamorphism, and  
 34  
 35  
 36  
 37  
 38  
 39  
 40  
 41  
 42  
 43  
 44  
 45  
 46  
 47  
 48  
 49  
 50  
 51  
 52  
 53  
 54  
 55  
 56  
 57  
 58  
 59  
 60  
 61  
 62  
 63  
 64  
 65
- 1540 rapid denudation at Nanga Parbat (Pakistan Himalaya). *Geology*, 21, 347-350.
- 1541 Zeidler, P.K., Meltzer, A.S., Koons, P.O., Craw, D., Hallet, B., Chamberlain, C.P., Kidd, W.S.,  
 37  
 38  
 39  
 40  
 41  
 42  
 43  
 44  
 45  
 46  
 47  
 48  
 49  
 50  
 51  
 52  
 53  
 54  
 55  
 56  
 57  
 58  
 59  
 60  
 61  
 62  
 63  
 64  
 65
- 1542 Park, S.K., Seeber, L., Bishop, M., Shroder, J., 2001. Erosion, Himalayan geodynamics, and the  
 40  
 41  
 42  
 43  
 44  
 45  
 46  
 47  
 48  
 49  
 50  
 51  
 52  
 53  
 54  
 55  
 56  
 57  
 58  
 59  
 60  
 61  
 62  
 63  
 64  
 65
- 1543 geomorphology of metamorphism. *GSA Today*, 11, 4-9.
- 1544 Zhuang, G., Najman, Y., Guillot, S., Roddaz, M., Antoine, P.O., Métais, G., Carter, A., Marivaux,  
 43  
 44  
 45  
 46  
 47  
 48  
 49  
 50  
 51  
 52  
 53  
 54  
 55  
 56  
 57  
 58  
 59  
 60  
 61  
 62  
 63  
 64  
 65
- 1545 L., Solangi, S.H., 2015. Constraints on the collision and the pre-collision tectonic configuration  
 45  
 46  
 47  
 48  
 49  
 50  
 51  
 52  
 53  
 54  
 55  
 56  
 57  
 58  
 59  
 60  
 61  
 62  
 63  
 64  
 65
- 1546 between India and Asia from detrital geochronology, thermochronology, and geochemistry  
 47  
 48  
 49  
 50  
 51  
 52  
 53  
 54  
 55  
 56  
 57  
 58  
 59  
 60  
 61  
 62  
 63  
 64  
 65
- 1547 studies in the lower Indus basin, Pakistan. *Earth and Planetary Science Letters*, 432, 363-373.  
 50  
 51  
 52  
 53  
 54  
 55  
 56  
 57  
 58  
 59  
 60  
 61  
 62  
 63  
 64  
 65
- 1548 Zhuang, G., Najman, Y., Tian, Y., Carter, A., Gemignani, L., Wijbrans, J., Jan, M.Q., Khan, M.A.,  
 51  
 52  
 53  
 54  
 55  
 56  
 57  
 58  
 59  
 60  
 61  
 62  
 63  
 64  
 65
- 1549 2018. Insights into the evolution of the Hindu Kush–Kohistan–Karakoram from modern river  
 53  
 54  
 55  
 56  
 57  
 58  
 59  
 60  
 61  
 62  
 63  
 64  
 65
- 1550 sand detrital geo- and thermochronological studies. *Journal of the Geological Society*  
 55  
 56  
 57  
 58  
 59  
 60  
 61  
 62  
 63  
 64  
 65
- 1551 London, 175(6), 934-948.  
 57  
 58  
 59  
 60  
 61  
 62  
 63  
 64  
 65

1553

1  
2  
3  
4  
5  
6  
7  
8  
9  
10  
11  
12  
13  
14  
15  
16  
17  
18  
19  
20  
21  
22  
23  
24  
25  
26  
27  
28  
29  
30  
31  
32  
33  
34  
35  
36  
37  
38  
39  
40  
41  
42  
43  
44  
45  
46  
47  
48  
49  
50  
51  
52  
53  
54  
55  
56  
57  
58  
59  
60  
61  
62  
63  
64  
65

**Provenance of Thal Desert sand: focused erosion in the western Himalayan syntaxis and foreland-basin deposition driven by latest Quaternary climate change**

**ABSTRACT**

As a latest Pleistocene repository of Indus River sand at the entry point to the Himalayan foreland basin, the Thal dune field in northern Pakistan stores crucial information that can be used to reconstruct the erosional evolution of the Himalayan-Karakorum orogen and the changes in the foreland-basin landscape that took place between the Last Glacial Maximum and the early Holocene. This comprehensive provenance study of Thal Desert sand integrates previously existing petrographic, heavy-mineral, mineral-chemical, isotopic, and geochronological databases with original bulk-sediment geochemistry, zircon-age, and Nd-isotope data. Dune sand is low in quartz and rich in feldspars, volcanic, metavolcanic and metabasite grains, contains a very rich transparent heavy-mineral suite including hypersthene and common zircon grains dated as Late Cretaceous to early Paleogene, and is characterized by high Mg, Sc, V, Co, Ni, Cu concentrations and by  $\epsilon_{\text{Nd}}$  values as high as -3.5. Together, these data indicate that ~40% of Thal dune sand was supplied by erosion of the Kohistan arc, a proportion that far exceeds the one assessed for modern Upper Indus sand. Greater detrital supply from the Kohistan arc indicates notably different conditions of sediment generation, during a period in which the sediment-transport capacity of the Upper Indus in the dry lowlands was reduced and volumes of sand were extensively reworked by wind and accumulated in dune fields across the foreland basin. In the early Holocene, the renewed strength of the South Asian monsoon and consequently markedly increased water and sediment discharge led to incision of the Thal and Thar dune fields by the Indus River and its Punjab tributaries draining the Himalayan front directly hit by heavy monsoonal rains.



1  
2  
3  
4 **Provenance of Thal Desert sand: focused erosion in the western**  
5  
6  
7  
8  
9  
10 **Himalayan syntaxis and foreland-basin deposition driven by latest**  
11 **Quaternary climate change**  
12  
13  
14  
15  
16  
17

18 Eduardo Garzanti<sup>1\*</sup>, Wendong Liang<sup>1\*</sup>, Sergio Andò<sup>1</sup>, Peter D. Clift<sup>2</sup>, Alberto  
19 Resentini<sup>1</sup>, Pieter Vermeesch<sup>3</sup>, Giovanni Vezzoli<sup>1</sup>.  
20  
21  
22

23 <sup>1</sup> Laboratory for Provenance Studies, Department of Earth and Environmental Sciences,  
24 University of Milano-Bicocca, Milano 20126, Italy

25 <sup>2</sup> Department of Geology and Geophysics, Louisiana State University, Baton Rouge, LA 70803,  
26 USA

27 <sup>3</sup> London Geochronology Centre, Department of Earth Sciences, University College London,  
28 London, C1E 6BT, UK

29 \* Corresponding authors (e-mail: [eduardo.garzanti@unimib.it](mailto:eduardo.garzanti@unimib.it) and [w.liang@campus.unimib.it](mailto:w.liang@campus.unimib.it))  
30  
31  
32

33 **Keywords:** Sand petrography and geochemistry; Detrital-zircon geochronology; Variability of  
34  $\epsilon_{Nd}$  values; Focused erosion; Himalaya-Karakorum; Kohistan Arc; Indus River, Delta, and Fan.  
35  
36  
37

38 **Highlights:**  
39

40  
41 The Thal Desert is an inland archive of Indus sand from the western Himalaya syntaxis  
42

43 Sand stored in the Thal dunefield reveals major detrital supply from the Kohistan arc  
44

45 High variability of  $\epsilon_{Nd}$  values is controlled by minimal changes in monazite content  
46  
47

48 The Thal Desert formed in a dry landscape between the LGM and the wet early Holocene  
49  
50  
51  
52  
53  
54  
55  
56  
57  
58  
59  
60  
61  
62  
63  
64  
65

**Abstract**

1  
2  
3  
4 As a latest Pleistocene repository of Indus River sand at the entry point to the Himalayan foreland  
5  
6 basin, the Thal dune field in northern Pakistan stores crucial information that can be used to  
7  
8 reconstruct the erosional evolution of the Himalayan-Karakorum orogen and the changes in the  
9  
10 foreland-basin landscape that took place between the Last Glacial Maximum and the early Holocene.  
11  
12 This comprehensive provenance study of Thal Desert sand integrates previously existing petrographic,  
13  
14 heavy-mineral, mineral-chemical, isotopic, and geochronological databases with original bulk-  
15  
16 sediment geochemistry, zircon-age, and Nd-isotope data. Dune sand is low in quartz and rich in  
17  
18 feldspars, volcanic, metavolcanic and metabasite grains, contains a very rich transparent heavy-  
19  
20 mineral suite including hypersthene and common zircon grains dated as Late Cretaceous to early  
21  
22 Paleogene, and is characterized by high Mg, Sc, V, Co, Ni, Cu concentrations and by  $\epsilon_{Nd}$  values as  
23  
24 high as -3.5. Together, these data indicate that ~40% of Thal dune sand was supplied by erosion of the  
25  
26 Kohistan arc, a proportion that far exceeds the one assessed for modern Upper Indus sand. Greater  
27  
28 detrital supply from the Kohistan arc indicates notably different conditions of sediment generation,  
29  
30 during a period in which the sediment-transport capacity of the Upper Indus in the dry lowlands was  
31  
32 reduced and volumes of sand were extensively reworked by wind and accumulated in dune fields  
33  
34 across the foreland basin. In the early Holocene, the renewed strength of the South Asian monsoon  
35  
36 and consequently markedly increased water and sediment discharge led to incision of the Thal and  
37  
38 Thar dune fields by the Indus River and its Punjab tributaries draining the Himalayan front directly hit  
39  
40 by heavy monsoonal rains.  
41  
42  
43  
44  
45  
46  
47  
48  
49  
50  
51  
52  
53  
54  
55  
56  
57  
58  
59  
60  
61  
62  
63  
64  
65

## 1. Introduction

The western Himalaya and Karakorum Ranges (in Sanskrit: *hima* = snow, *alayah* = abode; in Uyghur Turkic: *kara* = black, *korum* = gravel) drained by the Indus River provide a spectacular example of an orogenic belt produced by continental collision (Searle, 2013). Ongoing indentation between the Indian and Asian continents since 60-58 Ma (Garzanti et al., 1987; Beck et al., 1995; Hu et al., 2015; Najman et al., 2017) and accelerated rock uplift associated with ultra-rapid exhumation of crystalline basement rocks since the Neogene (Rolland et al., 2001; Zeitler et al., 2001) resulted in extreme relief and erosion rates around the western Himalayan syntaxis (Burbank et al., 1996a; Shroder and Bishop, 2000).

An important contribution to a better understanding of the tectonic growth and erosional evolution of such a complex orogenic region, where geological processes are so intense, is given by provenance analysis of detritus carried by the precursors of the Indus River and stored through time in adjacent sedimentary basins (Critelli et al., 1990; Garzanti et al., 1996; Qayyum et al., 1997; Clift et al., 2001). Numerous studies of Himalayan foreland-basin strata have been devoted to understanding how the Indus River system has formed and evolved (e.g., Cervený et al., 1989; Critelli and Garzanti, 1994; Najman et al., 2003; Downing and Lindsay 2005; Roddaz et al., 2011; Chirouze et al., 2015; Zhuang et al., 2015). Crucial information is stored in the thick sediment pile accumulated in the Indus Fan, cored so far around its southeastern and western edges during Ocean Drilling Program (ODP) Leg 23 in 1972 (Jipa and Kidd, 1974; Mallik, 1978; Suczek and Ingersoll, 1985) and more recently during International Ocean Discovery Program (IODP) Expedition 355 to the Laxmi Basin in 2014 (Clift et al., 2019). Turbidites of proven Himalayan provenance recovered from both ODP Leg 23 and IODP Expedition 355 are however mostly late Miocene or younger in age, and much thus remains to be understood regarding earlier phases of orogenic erosion (Pandey et al., 1996).

26 While plunging deeper in time, paleogeographic reconstructions have to face an increasing number  
1  
27 of unknowns, not only because of subsequent accretion and exhumation of diverse geological units  
3  
48 but also because repeated modifications of the drainage system have occurred even in the recent  
5  
69 past (e.g., [Burbank et al., 1996b](#); [Clift et al., 2012](#)). Moreover, the compositional fingerprints of  
7  
80 ancient siliciclastic strata reflect a distorted image of the lithological structure of source terranes  
9  
10  
11 because of selective diagenetic dissolution of less durable detrital components ([Garzanti, 2019a](#)).

12  
13  
14 The safest way to proceed is to start from the knowledge of the modern sediment-routing system,  
15  
163 where everything is in principle known or knowable ([Garzanti et al., 2005](#); [Alizai et al., 2011, 2016](#);  
17  
18  
194 [East et al., 2015](#); [Zhuang et al., 2018](#)) and to extend that knowledge to the recent and less recent  
20  
213 past ([Clift et al., 2010](#); [Garzanti et al., 2020](#)). In this regard, a particularly interesting repository of  
22  
2336 clastic sediments is represented by the Thal Desert, a small dune field occupying a dry area just  
24  
25  
267 south of the Salt Range, the Pliocene thrust belt representing the front of the Himalayan orogen in  
27  
2838 central northern Pakistan ([Fig. 1](#)).

29  
30  
3139 Thal Desert dunes consist of wind-reworked sediment entirely supplied by the Indus River upstream  
32  
3340 of the orogenic front (henceforth named “Upper Indus”) that provides us with a precise  
34  
35  
3641 compositional signature of detritus dominantly generated by the rapid erosion of the western  
37  
3842 Himalayan syntaxis in the latest Quaternary. The Jhelum River and other large left-bank tributaries  
39  
40  
4143 draining the southern flank of the Himalaya and flowing across the Punjab plains convey their  
42  
4344 sediments to the Indus River only downstream of the Thal Desert, and their contribution to this  
44  
4545 dune field is negligible, as documented by the peculiar compositional signatures of eolian sands  
46  
47  
4846 ([Liang et al., 2019](#)). On the contrary, it is the Thal dunes that, eroded all along the western side of  
49  
507 the desert, contribute sand to the Jhelum River and to the Panjnad River downstream ([Fig. 2](#);  
51  
52  
5348 [Garzanti et al., 2005](#)).

54  
5549 The Upper Indus compositional signature preserved in the Thal dune field is exempt from any  
56  
57  
5850 anthropic modification that had occurred in the region (e.g., Tarbela Dam) and can be compared  
59  
6051 with sand composition in the Lower Indus River, Delta, and Fan. This allows us to calculate the  
61  
62  
63  
64  
65

52 relative amount of sediment shed from diverse upstream sources around the syntaxis *versus* those  
 1  
 2  
 3  
 4  
 5  
 6  
 7  
 8  
 9  
 10  
 11  
 12  
 13  
 14  
 15  
 16  
 17  
 18  
 19  
 20  
 21  
 22  
 23  
 24  
 25  
 26  
 27  
 28  
 29  
 30  
 31  
 32  
 33  
 34  
 35  
 36  
 37  
 38  
 39  
 40  
 41  
 42  
 43  
 44  
 45  
 46  
 47  
 48  
 49  
 50  
 51  
 52  
 53  
 54  
 55  
 56  
 57  
 58  
 59  
 60  
 61  
 62  
 63  
 64  
 65

11  
 12  
 13  
 14  
 15  
 16  
 17  
 18  
 19  
 20  
 21  
 22  
 23  
 24  
 25  
 26  
 27  
 28  
 29  
 30  
 31  
 32  
 33  
 34  
 35  
 36  
 37  
 38  
 39  
 40  
 41  
 42  
 43  
 44  
 45  
 46  
 47  
 48  
 49  
 50  
 51  
 52  
 53  
 54  
 55  
 56  
 57  
 58  
 59  
 60  
 61  
 62  
 63  
 64  
 65

## 2. The Thal Desert

32  
 33  
 34  
 35  
 36  
 37  
 38  
 39  
 40  
 41  
 42  
 43  
 44  
 45  
 46  
 47  
 48  
 49  
 50  
 51  
 52  
 53  
 54  
 55  
 56  
 57  
 58  
 59  
 60  
 61  
 62  
 63  
 64  
 65

54  
 55  
 56  
 57  
 58  
 59  
 60  
 61  
 62  
 63  
 64  
 65

79 Paleozoic to Eocene strata, Neogene molasse, and deep-water turbidites underlain by ophiolitic  
 80 complexes (Jadoon et al., 1994). The Punjab plains are underlain by up to 450 m of Quaternary  
 81 alluvium and eolian deposits lying over semiconsolidated Cenozoic rocks or directly over  
 82 Precambrian crystalline basement, which crops out in the Kirana Hills straddling the Chenab River  
 83 course and represents the topographic culmination of the NW/SE-trending Delhi-Sargodha ridge  
 84 (Greenman et al., 1967; Kadri, 1995).

## 85 2.1 Geomorphology

86 Different physiographic units can be distinguished in the Thal Desert, which lies at altitudes above  
 87 sea-level decreasing from ~200 m in the north to ~120 m in the south. The piedmont area  
 88 transitional to the Salt Range foothills hosts alluvial fans consisting of detritus reworked and  
 89 deposited during sheet floods, and fining downstream over distances of ~10 km. The desert area to  
 90 the south, covered by low sand dunes or rolling sand plains alternating with narrow valleys of  
 91 cultivable land, is underlain by Quaternary fluvial and eolian deposits more than 350 m-thick in  
 92 southern areas, but even thicker in the central part of the desert (Nickson et al., 2005). The recent  
 93 finding of Mesolithic artefacts at the top of sand dunes indicates that the accumulation of eolian  
 94 sand pre-dates the Holocene (Biagi et al., 2019). The last episode of dune growth may thus be  
 95 related to large sediment fluxes released during glacier retreat following the Last Glacial Maximum  
 96 (LGM) in the latest Pleistocene (Clift and Giosan, 2014).

97 The underlying alluvium mostly consists of laterally continuous bodies of fine to coarse sand, with  
 98 minor gravel and isolated mud lenses. Coarser deposits occur in the north closer to the Salt Range,  
 99 but otherwise the distribution of grain sizes is irregular, largely reflecting original deposition by the  
 100 constantly shifting paleo-Indus and/or adjacent tributaries. The presently active Indus River  
 101 floodplain reaches >20 km in width in the south. The abandoned floodplain is even wider and  
 102 includes areas of higher ground. These bar uplands are actively eroded by the Jhelum River in the

105 northeastern part of the desert, forming up to 10 m-high scarps facing the floodplain ([Greenman et](#)  
 106 [al., 1967](#)).

107

## 108 2.2. *Climate*

109

110 Summers are very hot in the Thal Desert with average temperatures around 35°C in June to July,  
 111 dropping to ~10°C in December to January. Average annual temperatures increase from ~24°C in  
 112 the north and west to ~28°C in the south. Most of the region receives less than 350 mm of rain per  
 113 year. Annual rainfall progressively decreases from the northern (617 mm on average recorded from  
 114 1991 to 2013 in the Mianwali meteorological station; [Shah and Ahmad, 2015](#)) to the southern edges  
 115 of the desert (150 mm; [Greenman et al., 1967](#)). Today, cold dry winds blow from the north in  
 116 winter, whereas hot rain-bearing winds blow from the south in summer, with an average speed of  
 117 several km per hour. Between March and April, hailstorms generated by air turbulence owing to the  
 118 high temperature difference between the warm surface and the cold upper atmosphere may cause  
 119 major damage to crop and buildings ([Gosal, 2004](#)). In the summer, dust storms are fostered by  
 120 unsteady thermal conditions and north/south temperature gradients ([Hussain et al., 2005](#)).

121

## 122 2.3. *Sediment flux*

123

124 The upper course of the Indus River, sourced in the Tibetan Plateau ([Fig. 2](#)), drains the Ladakh arc  
 125 and forearc basin together with the northern side of the Himalaya ([Garzanti and Van Haver, 1988](#);  
 126 [Henderson et al., 2010](#); [Munack et al., 2014](#)). Next, it cuts a deep gorge through the Nanga Parbat  
 127 crystalline massif and receives detritus from the Karakorum Range and Kohistan Arc ([Gaetani et](#)  
 128 [al., 1990](#); [Treloar et al., 1996](#); [Searle et al., 1999](#); [DiPietro and Pogue, 2004](#); [Pêcher et al., 2008](#);  
 129 [Burg, 2011](#)). Further downstream, it flows across the Himalayan belt and Potwar Plateau ([Khan et](#)  
 130 [al., 1997a](#)), where it joins with the Kabul River draining the Hindukush Range ([Hildebrand et al.,](#)  
 131 [2001](#)), crosses the Salt Range to eventually reach the lowlands where it flows southward confined  
 132 between the front of the Sulaiman Range in the west and the Thal Desert in the east ([Fig. 1](#)). After  
 133 closure of the Chashma Dam at the northwestern corner of the Thal Desert in 1971, and of the

134

135

136

137

134 Tarbela Dam ~200 km to the north in 1976, most of the sediment carried by the Indus River has  
 135 been trapped in artificial reservoirs. The suspended sediment flux upstream of Tarbela Dam was  
 136 gauged as between  $176\text{--}200 \cdot 10^6$  t/a (Tate and Farquharson, 2000; Ali and De Boer, 2007, 2008)  
 137 and 218, 235, or  $287 \cdot 10^6$  t/a (Rehman et al., 1997), whereas estimates of total sediment delivery to  
 138 the Arabian Sea before the Anthropocene range widely between  $100 \cdot 10^6$  t/a and  $675 \cdot 10^6$  t/a (Ali  
 139 and De Boer, 2007). Suspended load of the Kabul River was measured as  $36.6 \cdot 10^6$  t/a (i.e.  $17 \pm 3\%$   
 140 that of the Indus upstream of Tarbela Dam; Rehman et al., 1997)

141 The Thal Doab aquifer, consisting of Quaternary alluvial and eolian deposits with local mud lenses,  
 142 is recharged rapidly from river water and rainfall. The Indus River and its Punjab tributaries give  
 143 rise to one of the largest irrigation systems in the world, including the Chashma-Jhelum link canal  
 144 supplied with Indus waters and built between 1967 and 1971. A network of dams, barrages and  
 145 canals aims to convert the Thal Desert, where the water table lies between 9 and 0.5 m from ground  
 146 surface, into cultivable land (Shah and Ahmad, 2016; Hussain et al., 2017).

147 The main tributaries joining the Indus River downstream of the Thal Desert drain the Himalayan  
 148 belt (Fig. 2). Since the 1960 Indus Waters Treaty gave rights to the entire flow of the Indus, Jhelum,  
 149 and Chenab Rivers to Pakistan, and of the Ravi, Beas, and Sutlej Rivers to India, all Himalayan  
 150 tributaries of the Punjab have been dammed and linked by canals to irrigate the arid plains and  
 151 compensate for lost waters in eastern Pakistan. Water discharge dropped sharply from  $\geq 100$  km<sup>3</sup>/a  
 152 to  $\leq 60$  km<sup>3</sup>/a, and flow in the Ravi and Sutlej Rivers ceased except during monsoon floods. The  
 153 Mangla Dam, completed in 1967, has reduced sediment load of the Jhelum River from  $45 \cdot 10^6$  t/a  
 154 to  $< 0.5 \cdot 10^6$  t/a (Milliman et al., 1984; Meadows and Meadows, 1999; Giosan et al., 2006a). The  
 155 main right-bank (western) tributaries of the Indus River draining the Sulaiman Ranges are the  
 156 Gomal River (basin area 36,000 km<sup>2</sup>), characterized by extreme concentration of suspended solids  
 157 (42 g/l) and high sediment load ( $30 \cdot 10^6$  t/a), and the Kurram River ( $3 \cdot 10^6$  t/a; Rehman et al.,  
 158 1997). Other rivers are minor and mostly flow during flash floods.

### 3. Methods



161  
162  
2  
3  
163  
4  
5  
164  
6  
7  
165  
8  
9  
10  
166  
11  
12  
13  
167  
14  
15  
168  
16  
17  
169  
18  
19  
20  
170  
21  
22  
23  
24  
25  
26  
27  
28  
29  
30  
175  
31  
32  
176  
33  
34  
35  
36  
37  
38  
39  
179  
40  
41  
42  
43  
44  
45  
46  
47  
48  
49  
183  
50  
51  
52  
53  
54  
55  
56  
57  
58  
59  
60  
61  
62  
63  
64  
65

This study, focusing on fine-grained sand of eolian dunes sampled in February 2001 from the Thal Desert, provides geochemical and geochronological data on sand collected between 2001 and 2011 from active river bars in tributaries each draining a different geological domain around the western Himalayan syntaxis and on Upper Indus sand collected upstream of the Thal Desert (sampling locations indicated in [Appendix Table A1](#) and *Google Earth* file [Thal & Sources.kmz](#)). Geochemical data are also presented for sand from the Jhelum, Chenab, Ravi and Sutlej Rivers, and from the Lower Indus River and Delta. These new data integrate the extensive petrographic, heavy-mineral, and geochemical datasets built with the same analytical methods in the last 15 years ([Clift et al., 2002, 2010](#); [Garzanti et al., 2005](#); [Liang et al., 2019](#)).

### 3.1. Sand petrography and heavy minerals

A quartered aliquot of each bulk-sand sample of Thal Desert dunes was impregnated with araldite epoxy, cut into a standard thin section stained with alizarine red to distinguish dolomite and calcite, and analysed by counting 400 points by the Gazzi-Dickinson method ([Ingersoll et al., 1984](#)). Sand classification was based on the relative abundance of the three main groups of components (Q = quartz; F = feldspars; L = lithic fragments), considered where exceeding 10%QFL. According to standard use, the less abundant component goes first, the more abundant last (e.g., in a litho-feldspatho-quartzose sand  $Q > F > L > 10\%QFL$ ; [Garzanti, 2019b](#)). Metamorphic grains were classified by protolith composition and metamorphic rank; average rank of rock fragments in each sample was expressed by the metamorphic indices MI and MI\*, ranging respectively from 0 (detritus from sedimentary and volcanic rocks) or 100 (detritus from very low-grade metamorphic rocks) to 500 (detritus from high-grade metamorphic rocks; [Garzanti and Vezzoli, 2003](#)). Median grain size was determined in thin section by ranking the samples from coarsest to finest followed by visual comparison with in-house standards sieved at 0.25  $\phi$  interval.

187 Heavy minerals were separated in sodium polytungstate (density  $\sim 2.90 \text{ g/cm}^3$ ), using the 63-250  $\mu\text{m}$   
 188 fraction obtained by sieving and treated with oxalic and acetic acids. Analyses were carried out first  
 189 by counting 200-225 transparent heavy minerals on grain mounts by the area method ([Mange and](#)  
 190 [Maurer, 1992](#)). Next, in order to obtain an accurate estimate of volume percentages of each dense  
 191 detrital component ([Galehouse, 1971](#)), between 275 and 1300 dense grains per sample (700 on  
 192 average) were point-counted on a polished thin section by semi-automated analysis with a Raman  
 193 spectrometer ([Andò and Garzanti, 2014](#); [Lünsdorf et al., 2019](#)).

194 Transparent heavy-mineral assemblages, called for brevity “tHM suites” throughout the text, are  
 195 defined as the spectrum of detrital extrabasinal minerals with density  $> 2.90 \text{ g/cm}^3$  identifiable under  
 196 a transmitted-light microscope. According to the volume percentage of transparent heavy minerals  
 197 in the sample (tHMC), tHM suites are defined as “poor” (tHMC  $< 1$ ), “moderately poor” ( $1 \leq$   
 198 tHMC  $< 2$ ), “moderately rich” ( $2 \leq$  tHMC  $< 5$ ), “rich” ( $5 \leq$  tHMC  $< 10$ ), “very-rich” ( $10 \leq$  tHMC  $<$   
 199  $20$ ), or “extremely rich” ( $20 \leq$  tHMC  $< 50$ ) ([Garzanti and Andò, 2007, 2019](#)). The sum of zircon,  
 200 tourmaline and rutile over total transparent heavy minerals (ZTR index of [Hubert, 1962](#)) estimates  
 201 the durability of the tHM suite (i.e., extent of recycling; [Garzanti, 2017](#)). Detrital components are  
 202 listed in order of abundance (high to low) throughout the text. The complete petrographic and  
 203 heavy-mineral datasets are provided in [Appendix Tables A2, A3, A4, and A5](#). Further information  
 204 on the chemical composition of detrital amphiboles, garnets, epidote-group minerals, and pyroxenes  
 205 is provided in [Liang et al. \(2019\)](#).

### 207 3.2. U-Pb zircon geochronology

208 Detrital zircons were identified by Automated Phase Mapping ([Vermeesch et al., 2017](#)) with a  
 209 Renishaw inVia<sup>TM</sup> Raman microscope on the heavy-mineral separates of 14 samples (three from the  
 210 Thal Desert, two from the Upper Indus, and nine from diverse end-member sources). U-Pb zircon  
 211 ages were determined at the London Geochronology Centre using an Agilent 7700x LA-ICP-MS  
 212 (laser ablation-inductively coupled plasma-mass spectrometry) system, employing a NewWave  
 213

214 NWR193 Excimer Laser operated at 10 Hz with a 20  $\mu\text{m}$  spot size and  $\sim 2.5 \text{ J/cm}^2$  fluence. No  
 215 cathodo-luminescence imaging was done, and the laser spot was always placed “blindly” in the  
 216 middle of zircon grains in order to treat all samples equally and avoid bias in intersample  
 217 comparison (“blind-dating approach” as discussed in [Garzanti et al., 2018](#)). Data reduction was  
 218 performed using GLITTER 4.4.2 software ([Griffin et al., 2008](#)). We used  $^{206}\text{Pb}/^{238}\text{U}$  and  $^{207}\text{Pb}/^{206}\text{Pb}$   
 219 ages for zircons younger and older than 1100 Ma, respectively. No common Pb correction was  
 220 applied. Grains with  $> +5 / -15\%$  age discordance were discarded, and 1392 concordant ages were  
 221 obtained overall. The full geochronological dataset is provided in [Appendix B](#).

### 222 3.3. Bulk chemistry and Nd isotopes

223 Chemical analyses of 23 sand samples (four from the Thal Desert, eight from diverse end-member  
 224 sources, three from the Upper Indus, four from Punjab tributaries, and four from the Lower Indus  
 225 and Delta) were carried out at Bureau Veritas Mineral Laboratories (Vancouver) on a split aliquot of  
 226 the 63-2000  $\mu\text{m}$  fraction obtained by wet sieving. Major oxides were determined by ICP-ES and  
 227 trace elements by ICP-MS, following a lithium metaborate/tetraborate fusion and nitric acid  
 228 digestion. A separate split was digested in aqua regia and analysed for Mo, Cu, Ag, Au, Zn, Cd, Hg,  
 229 Tl, Pb, As, Sb, Bi and Se, but the concentration of these elements is generally underestimated  
 230 because of incomplete leaching of refractory minerals. For further information on adopted  
 231 procedures, geostandards used, and precision for various elements see <http://acmelab.com> (code  
 232 LF200). The geochemical dataset is provided in [Appendix Table A6](#).

233 For each of the four Thal Desert samples, several grams of the bulk sand were powdered to ensure a  
 234 good average composition. Samples were then dissolved, and the Nd separated using standard  
 235 column extraction techniques. Nd isotopic compositions were determined on VG354 mass  
 236 spectrometer at Woods Hole Oceanographic Institution.  $^{143}\text{Nd}/^{144}\text{Nd}$  values were normalized to  
 237  $^{146}\text{Nd}/^{144}\text{Nd} = 0.7219$  and relative to 0.511847 for the La Jolla standard. We calculated the parameter  
 238  $\epsilon_{\text{Nd}}$  ([DePaolo and Wasserburg, 1976](#)) using a  $^{143}\text{Nd}/^{144}\text{Nd}$  value of 0.512638 for the Chondritic

241 Uniform Reservoir ([Hamilton et al., 1983](#)). Original data and a compilation of literature data are  
 242 provided in [Appendix Tables A7](#) and [A8](#).

243

### 244 3.4. Statistical/graphical displays

245  
 246 Zircon-age data, plotted using the *provenance* package of [Vermeesch et al. \(2016\)](#), are visualized as  
 247 kernel density estimates (KDE) with a nominal bandwidth of 40 Ma ([Vermeesch, 2012](#)). Statistical  
 248 techniques used to illustrate our datasets also include the compositional biplot ([Gabriel, 1971](#)) and  
 249 multidimensional scaling (MDS; [Vermeesch, 2013](#); [Vermeesch and Garzanti, 2015](#)).

250 The biplot, drawn using *CoDaPack* software by [Comas-Cufí and Thió-Henestrosa \(2011\)](#), allows  
 251 discrimination among multivariate observations (points) while shedding light on the mutual  
 252 relationships among variables (rays). The length of each ray is proportional to the variance of the  
 253 corresponding variable in the dataset. If the angle between two rays is close to 0°, 90° or 180°, then  
 254 the corresponding variables are directly correlated, uncorrelated, or inversely correlated,  
 255 respectively.

256 MDS produces a map of points in which the distance among samples is approximately proportional  
 257 to the Kolmogorov-Smirnov dissimilarity of their compositional or chronological signatures. Closest  
 258 and second-closest neighbours are linked by solid and dashed lines, respectively, and the goodness  
 259 of fit is evaluated using the “stress” value of the configuration (0.2 = poor; 0.1 = fair; 0.05 = good;  
 260 [Kruskal, 1964](#); table 1 in [Vermeesch, 2013](#); [2018](#)).

261

## 262 4. Compositional fingerprints of Thal Desert sand

263

### 264 4.1. Petrography and heavy minerals

265  
 266 Three Thal dune samples are litho-feldspatho-quartzose sands and one is quartzo-feldspatho-lithic  
 267 (average composition Q37 F34 L29; [Fig. 3A](#)). Quartz is mostly monocrystalline. K-feldspar and  
 268 plagioclase occur in subequal amounts. The rock-fragment population includes metasedimentary  
 269 (paragneiss, schist, slate, calcschist, phyllite, metasandstone), metabasite (prasinite, chloritoschist,  
 270

271  
 272  
 273  
 274  
 275

270 amphibolite), carbonate (limestone, dolostone), other sedimentary (shale, siltstone, minor chert),  
 271 granitoid, felsic to mafic volcanic and metavolcanic, and minor ultramafic (serpentineschist, cellular  
 272 serpentinite) grains (MI 209-290, MI\* 273-317). A few muscovite and biotite flakes are present.  
 273 The very rich tHM suite is dominated by mainly blue-green amphiboles associated with epidote,  
 274 garnet, green to colourless clinopyroxene, and hypersthene. Titanite, staurolite, kyanite, zircon,  
 275 tourmaline, rutile, sillimanite, olivine, and chloritoid also occur ( $ZTR \leq 4$ ). Detrital amphiboles  
 276 include mainly hornblende, subordinate pargasite, actinolite, hastingsite, and minor tschermakite.  
 277 Detrital garnet is mostly almandine with minor grossular, pyrope, spessartine, and andradite (mostly  
 278 Bi grains with minor Ci, Bii, A, and a few D grains according to the classification of [Mange and](#)  
 279 [Morton, 2007](#)). Epidote-group minerals are mainly clinozoisite and epidote. Detrital pyroxene is  
 280 mainly diopside with common orthopyroxene and minor augite ([Liang et al., 2019](#)).

#### 282 4.2. Detrital-zircon geochronology

283  
 284 The three Thal samples analysed yielded 103 concordant ages overall, including early Miocene (22  
 285 Ma; n=3), Eocene (38-53 Ma; n=15), latest Cretaceous/Paleocene (61-84 Ma; n=19), mid-  
 286 Cretaceous (98-110 Ma; n=10), Orosirian (1.82-1.87 Ga; n=15), and earliest Paleoproterozoic  
 287 clusters (2.32-2.39 Ga; n=4). Other ages are spread in the Mesozoic (n=6), Paleozoic (n=6),  
 288 Neoproterozoic (n=13), late Mesoproterozoic (n=4), Paleoproterozoic (n=4), and earliest  
 289 Paleoproterozoic to late Neoproterozoic (n=4).

#### 290 4.3. Sand geochemistry

291  
 292 Despite their homogenous provenance, local selective-entrainment effects account for a difference  
 293 in heavy-mineral concentration by a factor of two in our Thal Desert sand samples. This  
 294 corresponds to a difference by factors of between 2.5 and 5 of elements preferentially hosted in the  
 295 densest rock-forming minerals such as opaque Fe-Ti-Cr oxides, monazite, zircon, and to a lesser  
 296 extent rutile and garnet (i.e., Fe, Ti, Mn, Y, REE, Th, U, Zr, Hf, V, Nb, Ta and Cr). The europium  
 297 anomaly  $Eu/Eu^*$  varies from 0.74 in the less heavy-mineral rich sample S1474 (Zr 106 ppm) to 0.46  
 298

299 in the sample richest in heavy minerals S1470 (Zr 524 ppm) and is 0.62-0.64 in the other two  
 300 samples S1462 and S1463 (Zr 195-213 ppm). The composition of Thal Desert sand compares  
 301 remarkably well with the Upper Continental Crust standard (UCC; [Taylor and McLennan, 1995](#);  
 302 [Rudnick and Gao, 2003](#)), but with twice as much Th and Cr, ~50% more Ca, Y, REE, and Zr, and  
 303 ~50% less K, Rb, and Ba, differences all largely accounted for by the strong local concentration of  
 304 densest minerals by selective-entrainment effects.

#### 305 4.4. Nd isotopes

306 Neodymium isotope ratios range widely in the studied Thal Desert sand samples. All four samples  
 307 are fine sands, but coarser samples characterized by higher heavy-mineral concentration and more  
 308 volcanic, metavolcanic, and metabasite rock fragments have less negative  $\epsilon_{Nd}$  (2.0-2.2  $\phi$ ; tHMC 18-  
 309 19;  $\epsilon_{Nd}$  -3.5 and -8.7) than finer-grained samples (2.3-2.7  $\phi$ ; tHMC 10-15;  $\epsilon_{Nd}$  -10.9 and -13.2).  
 310 Because their bulk-sediment mineralogy is homogeneous overall, indicating notably constant  
 311 provenance, such a marked variability is dominantly controlled by local factors including grain size  
 312 and concentration of densest minerals by selective entrainment of less dense grains by wind  
 313 deflation.

## 314 5. Compositional fingerprints of sand sources

315 All geological domains drained by the Upper Indus, including the Ladakh and Kohistan arcs, the  
 316 Karakorum and Hindukush Ranges, the Himalayan belt, and the Nanga Parbat massif are detrital  
 317 sources of Thal Desert dunes ([Fig. 4](#)). The mineralogical signatures of modern sand carried by  
 318 tributaries draining each geological domain, summarized here below, are illustrated in detail in  
 319 [Garzanti et al. \(2005\)](#) and [Liang et al. \(2019\)](#).

### 320 5.1. Petrography and heavy minerals

327 Indus tributaries draining the Ladakh arc carry quartzo-feldspathic to feldspar-rich feldspatho-  
 328 quartzose plutoniclastic sand with a rich to very rich tHM suite dominated by amphibole (mostly  
 329 hornblende), with minor epidote, titanite, apatite, and clinopyroxene (mainly diopside).  
 330 Hypersthene or allanite are found locally.

331 River sand from the Kohistan arc ranges in composition from feldspatho-quartzo-lithic to litho-  
 332 quartzo-feldspathic metamorphiclastic with common prasinite and epidote-amphibolite grains and a  
 333 very rich to extremely rich tHM suite dominated by amphibole (mainly hornblende or pargasite  
 334 associated with actinolite or hastingsite and rare tschermakite). Epidote-group minerals (mostly  
 335 clinozoisite) and pyroxene (diopside, pigeonite, augite, and hypersthene) are common, whereas  
 336 mostly Ca-rich or Mg-rich garnet is rare.

337 Indus tributaries draining the Karakorum carry sand ranging in composition from quartzo-  
 338 feldspatho-lithic sedimentaelastic (North Karakorum) to quartzo-feldspathic plutoniclastic (Central  
 339 Karakorum) or litho-feldspatho-quartzose metamorphiclastic with marble grains (South  
 340 Karakorum). Mainly moderately rich tHM suites include mostly amphibole (mainly hornblende  
 341 with pargasite, hastingsite, or actinolite), epidote-group minerals (epidote, clinozoisite, and  
 342 allanite), mostly Bi-type garnet, titanite, mostly diopsidic clinopyroxene, and minor kyanite,  
 343 staurolite and sillimanite. A similar composition characterizes feldspatho-quartzo-lithic  
 344 sedimentaelastic sand of the Kabul River upstream of the Swat confluence.

345 Detritus from the Greater Himalaya, contributed by the Zanskar River and by minor rivers in  
 346 northern Pakistan, is litho-feldspatho-quartzose metamorphiclastic with a moderately rich tHM suite  
 347 including amphibole (pargasite and hornblende with minor hastingsite), mostly Bi-type garnet,  
 348 fibrolitic sillimanite, kyanite, epidote-group minerals (epidote, clinozoisite, minor allanite), and  
 349 pyroxene (diopside, augite, and locally hypersthene).

350 Sand supplied by tributaries draining the Nanga Parbat massif is mainly feldspar-rich feldspatho-  
 351 quartzose with an up to very rich tHM suite dominated by amphibole (mainly hornblende with

352  
353  
354  
355  
356  
357  
358  
359  
360  
361  
362  
363  
364  
365

352 common tschermakite and minor pargasite). Garnet (mainly Ci and minor Bii types), pyroxene  
 353 (diopside with rare augite), epidote, clinozoisite, and sillimanite occur.

354 The Soan River, mostly recycling Cenozoic foreland-basin strata, carries feldspatho-litho-quartzose  
 355 sedimentaelastic sand with a moderately rich, epidote-dominated tHM suite with garnet,  
 356 hornblende, and tourmaline.

357 As far as REE-rich minerals are concerned, allanite is invariably common (2-3 tHM%) in sand  
 358 carried by the Hushe, Braldu, Hispar, and Hunza Rivers draining the Karakorum Range.  
 359 Karakorum-derived sand contains two to five times more allanite than sand shed by the Greater  
 360 Himalaya and Nanga Parbat, and one order of magnitude more allanite than sand shed by the  
 361 Ladakh and Kohistan arcs. Monazite is rarer and was detected in sand derived from the Karakorum  
 362 and in Zanskar sand.

363

## 364 5.2. Detrital-zircon geochronology

### 365 5.2.1. Ladakh and Kohistan arcs

366 Modern river sand derived from the Transhimalayan arcs yielded simple zircon-age spectra (Fig. 5),  
 367 reflecting peaks of magmatic activity in the Ladakh (50-70 Ma, [Weinberg and Dunlap, 2000](#); 58-60  
 368 Ma, [Singh et al., 2007](#); 50-67 Ma, [Ravikant et al., 2009](#); 47-58 Ma, [St-Onge et al., 2010](#)) and  
 369 Kohistan arc (82-99 Ma, [Schaltegger et al., 2002](#); 42-85 Ma, [Jagoutz et al., 2009](#)).

370 Sand of the Domkar stream draining the Ladakh arc shows a dominant Eocene-Paleocene peak (49-  
 371 65 Ma; n=34) with a younger age at 46 Ma and a Late Cretaceous cluster (78-87 Ma; n=7). Kandia  
 372 and Swat sands derived from the Kohistan arc display a Late Cretaceous peak (73-95 Ma; n=54)  
 373 with two younger ages at 56 Ma and 69 Ma and three older ages at 716 Ma, 1086 Ma, and 2545 Ma.  
 374 A younger spectrum, very similar to Domkar sand, was obtained by [Zhuang et al. \(2018\)](#) from Dir  
 375 River sand, which displays a prominent Eocene-Paleocene peak (43-65 Ma; n=76), several  
 376 Cretaceous aged grains (76-118 Ma; n=14), and a few older grains (196-821 Ma; n= 4).

### 377 5.2.2. Karakorum Range

378  
 379  
 380  
 381  
 382  
 383  
 384  
 385



381 The four samples of Karakorum river sand yielded 576 concordant ages overall (Fig. 5), including  
 382  
 383 prominent peaks in the early Miocene/latest Oligocene (16-26 Ma; n=19), late Eocene (35-43 Ma;  
 384 n=51), Paleocene (57-66 Ma; n=10), and mid-Cretaceous (99-130 Ma; n=184), with sparse ages in  
 385 the Rupelian (31 Ma), early Eocene (48 Ma), Campanian (73 Ma and 76 Ma), and Turonian (91-92  
 386 Ma; n=4). Older ages are irregularly spread between the earliest Cretaceous and the Ordovician  
 387 (134-484 Ma; n=47), form a broad cluster ranging between the Cambrian and the latest  
 388 Mesoproterozoic (490-1026 Ma; n=201), are again sparsely spread through the Mesoproterozoic  
 389 and Paleoproterozoic (1050-2448 Ma; n=34), and form a cluster straddling the Proterozoic/Archean  
 390 boundary (2468-2535 Ma; n=15) with a few older Archean grains (2553-3568 Ma; n=7). Most ages  
 391 from our Upper Hunza River sample combined with that from the same site analysed by Zhuang et  
 392 al. (2018) outline two dominant young clusters at 48-74 Ma (n=51) and 101-122 Ma (n=81) with  
 393 other sparse ages at 44 Ma, 82-93 Ma (n=4), 126-130 Ma (n=3), and 239 Ma. All older ages (377-  
 394 893 Ma; n=7) are from our sample.

395 Zircon ages in Karakorum-derived sand correspond closely with the ages of igneous and  
 396 metamorphic rocks exposed in the range. The early Miocene peak found in zircons from Hushe (19-  
 397 26 Ma; n=9/55) and Braldu (16-25 Ma; n=10/124) sands reflects the age of high-grade  
 398 metamorphism, crustal melting and emplacement of the Baltoro granite (21-26 Ma; Schärer, et al.,  
 399 1990; 13-26 Ma, Searle et al., 2010; 15-26 Ma, Mahar et al., 2014). The Eocene peak found in  
 400 Hispar sand (35-42 Ma; n=48/359) reflects the age of upper-amphibolite-facies metamorphism in  
 401 the South Karakorum belt (44-64 Ma, Fraser et al., 2001; 37-55 Ma, Rolland et al., 2001). The  
 402 Lower Cretaceous peak is prominent in all samples (100-125 Ma; n=120/359 in Hispar sand,  
 403 n=29/124 in Braldu sand, and n=15/55 in Hushe sand) and reflects the emplacement age of the  
 404 central Karakorum batholith (95-110 Ma, Debon et al., 1987; 95-115 Ma, Crawford and Searle,  
 405 1992). Whereas earliest Cretaceous to Silurian zircons are few and possibly recycled from  
 406 sedimentary and low-grade metasedimentary rocks, ages between the Ordovician and the latest  
 407 Mesoproterozoic are common in all samples, and reflect the Pan-African orogenic event widely

408 detected in the Himalayas ([Garzanti et al., 1986](#); [DeCelles et al., 2000](#); [Miller et al., 2001](#); [Gehrels](#)  
 409 [et al., 2003](#)). Older zircons, mostly represented in Hispar and Braldu sands with ages clustering  
 410 around 2.5 Ga, may be largely recycled from sedimentary and metasedimentary units.

### 411 5.2.3. Hindukush Range and Kabul River

412 In a sand sample analysed by [Zhuang et al. \(2018\)](#) from the Chitral-Kunar River, which drains both  
 413 Hindukush and Karakorum Ranges, half of the zircon ages are spread between the Cambrian and  
 414 the Tonian (486-976 Ma; n=61/126), whereas minor clusters are documented at 62-70 Ma (n=8),  
 415 102-114 Ma (n=16), 1851-1891 Ma (n=6), and 2467-2515 Ma (n=4).

416 The zircon age-spectrum obtained by [Zhuang et al. \(2018\)](#) on a sand sample from the Kabul River  
 417 downstream is notably different, with a younger peak at 31-38 Ma (n=12), a Cretaceous cluster at  
 418 75-113 Ma (n=39), a small peak at 191-204 Ma (n=10) – a Cimmerian age characteristic of  
 419 Hindukush igneous and metamorphic rocks ([Hildebrand et al., 2001](#)) –, a broad Cambrian-Tonian  
 420 spread (495-986 Ma; n=28), and a few Orosirian (1841-1847 Ma; n=3) and older ages (2074-2592  
 421 Ma; n=7). Ages were recorded also at 46-71 Ma (n=3), 123-179 Ma (n=7), 211-482 Ma (n=7), and  
 422 1011-1419 Ma (n=4).

### 423 5.2.4. Nanga Parbat

424 The Astor River sand derived from the Nanga Parbat massif yielded a unimodal earliest Statherian-  
 425 Orosirian peak at 1787-1941 Ma (n=98) consistent with the age of the gneissic basement (~1850  
 426 Ma; [Zeitler et al., 1993](#); [Whittington et al., 2000](#); [Schneider et al., 2001](#)). This major episode of  
 427 crustal growth is widely recognized in the Lesser Himalaya (e.g., [Miller et al., 2000](#); [Singh et al.,](#)  
 428 [2009](#); [Gehrels et al., 2011](#); “Ulleri-Wangtu” event of [Prasad et al., 2011](#)). Older Paleoproterozoic  
 429 ages (1964-2494 Ma; n=14) and one latest Carboniferous age also occur ([Fig. 5](#)). No grain younger  
 430 than 47 Ma was found, and the few early Eocene to Late Cretaceous zircons (47-88 Ma; n=7) may  
 431 be derived from the Ladakh arc drained in the upper course.

### 432 5.2.5. Greater Himalaya

438  
 439 Nandihar River sand derived from the Greater Himalaya in Pakistan yielded mainly early-middle  
 440 Neoproterozoic ages (740-989 Ma; n=20), with sparse Carboniferous to Ediacaran ages (345-547  
 441 Ma; n=11) and a few younger (105 Ma and 216 Ma) and older grains (1700 Ma, 1803 Ma, and 2400  
 442 Ma) (Fig. 5). A similar spectrum was obtained by Jonell et al. (2017a) from Zanskar River sand,  
 443 with better defined Cryogenian-Tonian (751-856 Ma; n= 44) and Carboniferous-Ordovician clusters  
 444 (337-476 Ma; n=27), and sparse younger (58 Ma, 246 Ma, and 301 Ma) and older ages (1040-3117  
 445 Ma; n=17)

### 446 447 5.3. Sand geochemistry

448  
 449 The provenance-discrimination power of bulk-sediment geochemistry is limited, because the same  
 450 chemical elements are hosted in different minerals found in a wide range of rocks and because  
 451 element concentrations are severely affected by grain-size and hydraulic-sorting effects (Garzanti,  
 452 2016). Nevertheless, some remarkable differences are noted among sands derived from different  
 453 geological domains surrounding the western Himalayan syntaxis (Fig. 6A).

454 Sand derived from the Kohistan arc is enriched 1.5-2 times in Fe, Mg, Ca, Sc, Ti, V and Cr  
 455 relatively to the UCC standard, and depleted by ~50% or more in K, Rb, Ba, LREE, Th, U, Zr, Hf,  
 456 Nb, Ta and Sn, reflecting the mainly intermediate to mafic character of calc-alkaline magmatic  
 457 source-rocks. Domkar sand derived from the Ladakh arc is notably different and much closer to the  
 458 UCC standard, although depleted by 50% or more in Mg, Nb, Ta, Cr and Co, which reflects the  
 459 more felsic character of the largely granodioritic calc-alkaline source rocks.

460 Hispar River sand derived from the Central and South Karakorum is enriched by factors of 2-3  
 461 relative to the UCC standard in REE, U, Zr and Hf, and by factors of 5-10 in Th, W and As. This  
 462 may be ascribed to selective entrainment of less dense detrital components in the river channel and  
 463 consequent concentration of densest minerals probably including monazite and scheelite. Elements  
 464 most depleted relative to the UCC are Mg, V, Co and Ni.

465 Himalayan-derived sand displays overall homogeneous character. Most elements – excepting Si,  
 1  
 466 Ca, LREE and Th – are slightly depleted relatively to the UCC standard, which is typical of sand  
 3  
 467 including detritus recycled from sedimentary and metasedimentary rocks. Large differences in Ca  
 5  
 468 and to a lesser extent Sr reflect varying amounts of carbonate detritus, which is particularly  
 8  
 469 abundant in sand of the Zanskar River cutting across the Tethys Himalaya zone (Blöthe et al., 2014;  
 10  
 470 Jonell et al., 2017a). Zanskar and Astor sands are the closest to UCC composition: Zanskar sand is  
 13  
 471 markedly depleted in V, Cr, Co and Ni, and Astor sand slight enriched in Rb and Th and markedly  
 15  
 472 depleted in Nb, Ta and Ni. Soan sand is more depleted (by ~50%) in Na and other mobile alkalic  
 17  
 473 and alkaline-earth metals excepting Ca and Sr, suggesting weathering inherited from recycling of  
 20  
 474 Cenozoic Himalayan molasse exposed within and around the Potwar Plateau (Garzanti and  
 22  
 475 Resentini, 2016).

#### 476 5.4. Nd isotopes

477 The  $^{143}\text{Nd}/^{144}\text{Nd}$  isotopic ratio provides a useful means to discriminate among different source-rock  
 29  
 478 domains in the Himalayan-Karakorum orogen (e.g., Clift et al., 2002; Chirouze et al., 2015; Zhuang  
 31  
 479 et al., 2015) (Appendix Tables A7 and A8). Juvenile values characterize the Ladakh and Kohistan  
 34  
 480 arcs ( $\epsilon_{\text{Nd}}$  mostly from 0 to +8; Petterson et al., 1993; Khan et al., 1997b; Rolland et al., 2002;  
 36  
 481 Jagoutz et al., 2019), whereas the most radiogenic values identify the gneissic basement of the  
 38  
 482 Nanga Parbat massif ( $\epsilon_{\text{Nd}}$  from -18 to -30; Whittington et al., 1999; Argles et al., 2003). Values are  
 40  
 483 very negative also in Lesser Himalayan rocks ( $\epsilon_{\text{Nd}}$  mainly from -19 to -26), but less negative for the  
 42  
 484 Tethyan and Greater Himalaya ( $\epsilon_{\text{Nd}}$  mainly from -13 to -20; Parrish and Hodges, 1996; Whittington  
 44  
 485 et al., 1999; Ahmad et al., 2000). Values intermediate between the Himalayan belt and  
 46  
 486 Transhimalayan arcs characterize the Karakorum ( $\epsilon_{\text{Nd}}$  mainly from -6 to -12; Schärer et al., 1990;  
 48  
 487 Mahéo et al., 2009).

## 6. Compositional fingerprints of Indus sand from the mountains to the deep sea

### 6.1. Petrography and heavy minerals

The modern Upper Indus River carries feldspatho-litho-quartzose sand to the foreland basin, including a variety of sedimentary and metamorphic rock fragments, and a rich hornblende-dominated tHM suite with epidote, garnet, and minor clinopyroxene, hypersthene, staurolite, titanite, kyanite, and sillimanite (Fig. 3B). In the mid-Miocene, the Burdigalian-Langhian (18-14 Ma) Kamli Formation, exposed in the Potwar Plateau and inferred to have been largely deposited by a paleo-Indus River, contains feldspatho-quartzo-lithic sandstones including sedimentary as well as volcanic, metavolcanic, and metabasite rock fragments (Najman et al., 2003). This may represent the time when a drainage system similar to the present one was first established. The existence and compositional fingerprints of a paleo-Indus at older times remain loosely constrained (Clift et al., 2000; Roddaz et al., 2011; Zhuang et al., 2015).

Himalayan tributaries in the Punjab region carry feldspatho-litho-quartzose sand with varied sedimentary and metamorphic rock fragments and mainly moderately rich epidote-amphibole-garnet tHM suites including dravitic tourmaline, kyanite, fibrolitic sillimanite, and staurolite (Fig. 3C). Right-bank tributaries draining the sedimentary succession of the Sulaiman-Kirthar Ranges – as well as Indian basement rocks of the Spinghar Crystalline (Badhsah et al., 2000) and the Waziristan, Zhob and Muslimbagh ophiolites (Gnos et al., 1997) – carry feldspatho-quartzo-lithic sedimentary to lithic carbonaticlastic sand yielding very poor to moderately rich tHM suites with epidote, amphibole, clinopyroxene, and garnet. Minor ophiolitic detritus includes serpentinite grains, enstatite, olivine, and Cr-spinel.

The Lower Indus River carries feldspatho-litho-quartzose sand with mostly sedimentary and metamorphic rock fragments, and a rich amphibole-epidote-garnet tHM suite with minor clinopyroxene, titanite, tourmaline, kyanite, staurolite, hypersthene, and sillimanite (Fig. 3D). LGM to Holocene Delta sand has a very similar composition (Clift et al., 2010), with differences mostly

518 accounted for by hydraulic-sorting effects (more micas, less heavy minerals, and especially less  
 519 high-density garnet; [Fig. 3E](#)).

520 Plio-Quaternary Indus Fan turbidites reported from ODP Sites 221 and 222 are more feldspathic  
 521 (Q49 F31 L20; [Suczek and Ingersoll, 1985](#)) than modern Lower Indus River (Q48 F21 L31;  
 522 [Garzanti et al., 2005](#)) and LGM to Holocene Delta sands (Q49 F26 L25; [Clift et al., 2010](#)). Recent  
 523 data from upper Miocene to lower Pleistocene Indus Fan turbidites (Q52 F24 L25; [Garzanti et al.,](#)  
 524 [2020](#)), however, indicate that their main composition is quite similar to that of the modern Lower  
 525 Indus River and LGM to Holocene Delta sands ([Fig. 3F](#)), only with more abundant micas in finer-  
 526 grained overbank deposits ([Andò et al., 2019](#)).

## 527 6.2. Detrital-zircon geochronology

528 Zircon ages from two Upper Indus samples collected between the Kabul confluence and the Salt  
 529 Range front, combined with data from one sample analysed by [Zhuang et al. \(2018\)](#), cluster mainly  
 530 between 33 and 124 Ma (n=248). The youngest cluster occurs at 17-21 Ma (n=5) with another  
 531 young age at 30 Ma and older ages spread in the Early Cretaceous to Jurassic (127-170 Ma; n=14),  
 532 Triassic to Permian (205-290 Ma; n=16), and Carboniferous to Ordovician (302-482 Ma; n=17).  
 533 Zircon grains yielded common Cambrian to Neoproterozoic (485-1000 Ma; n=139) and earliest  
 534 Statherian-Orosirian ages (1788-1948; n=39), and fewer Mesoproterozoic to late Statherian (1008-  
 535 1669 Ma; n=24) and earliest Orosirian to late Siderian ages (2018-2441 Ma; n=20). The oldest  
 536 cluster occurs at 2449-2491 Ma (n=9) and several Archean ages were also obtained (2520-3508;  
 537 n=11). Such a composite age spectrum reflects the many distinct geological events that affected the  
 538 diverse source-rock domains. Age spectra do not change significantly downstream of the  
 539 confluence with the Soan River, a minor tributary largely recycling Himalayan molasse exposed  
 540 within and around the Potwar Plateau ([Critelli and Garzanti, 1994](#); [Critelli and Ingersoll, 1994](#)).

541 Sand carried by the Himalayan tributaries of the Punjab (Jhelum, Chenab, Ravi, Beas, and Sutlej  
 542 samples combined; data after [Alizai et al., 2011](#)) include only a few young grains (1 late Oligocene,  
 543

545 7 Lutetian-Ypresian, 13 Mesozoic, 1 Carboniferous) and common mid-early Paleozoic (9 Devonian,  
 546 13 Silurian, 48 Ordovician, 25 Cambrian) and Neoproterozoic zircons (18 Ediacaran, 32  
 547 Cryogenian, 116 Tonian). Mesoproterozoic zircons are much less common (26 Stenian, 7 Ectasian,  
 548 9 Calymmian) than Paleoproterozoic zircons (28 Statherian, 110 Orosirian, 22 Rhyacian, 14  
 549 Siderian), and 15 Neoproterozoic, 4 Mesoarchean, and 3 Paleoproterozoic grains also occur ([Appendix  
 Table A9](#)).

550 Sands in the Lower Indus River, Delta, and Fan display complex zircon-age distributions that reflect  
 551 all components present in the huge catchment. The age spectrum obtained by combining data on  
 552 eight modern fluvial and LGM to Holocene deltaic sands (n=766; [Clift et al., 2004, 2008, 2010](#))  
 553 reveals a marked change in age proportions relative to modern Upper Indus sand. The percentage of  
 554 Eocene-Cretaceous ages is notably lower, whereas a few more Miocene-Oligocene ages and many  
 555 more Silurian-Ordovician, Tonian-Stenian, and mid-Paleoproterozoic ages occur. The age spectrum  
 556 obtained by combining data on five Plio-Quaternary Indus Fan sands (n=624; [Clift et al., 2019](#)) is  
 557 quite similar, with an even lower percentage of Eocene-Cretaceous ages ([Appendix Table A9](#)).

558 Sand in the Indus Delta and Fan contains zircons as young as 11.3-11.7 Ma ([Clift et al., 2010,  
 559 2019](#)), which are notably younger than the youngest zircon grain found so far in the Upper Indus  
 560 catchment (i.e., 15.9 Ma in Braldu sand). Zircon grains even as young as 4.4 Ma have been detected  
 561 in the Indus Canyon ([Li et al., 2019](#)). In this regard, it is noteworthy that such very young grains are  
 562 found only in silt samples with modal grain size  $\leq 40 \mu\text{m}$ , whereas the youngest zircon in the only  
 563 sand sample analysed so far is dated as 14.2 Ma. Because such young ages were never obtained  
 564 from the core of sand-sized zircon grains, it is likely that they correspond to small fragments  
 565 chipped off the rim of zircon grains with an older core. In the same way, the notably greater  
 566 abundance of relatively young lower Mesozoic to upper Paleozoic ages in Indus Canyon samples  
 567 might reflect the greater frequency of zircon rims recording thermal events that followed the Pan-  
 568 African orogeny. The other peculiar features of Indus Canyon zircons (spectrum of 988 ages  
 569 combined from ten medium silts to fine sands deposited in the last 50 ka; [Li et al., 2019](#)) are the



571 much smaller population of Orosirian aged grains and the disappearance of the minor cluster around  
 572 2.5 Ga, which also may be explained by a greater frequency of analysed small grains, originally  
 573 representing younger rims surrounding older crystal cores.

### 574 6.3. Sand geochemistry

576 Upper Indus sand is similar to the UCC standard, apart from a moderate enrichment in elements  
 577 preferentially concentrated in densest minerals such as zircon and monazite (Zr 254-323 ppm,  
 578 Eu/Eu\* 0.51-0.61) and a depletion in Na, K, Rb and Ba preferentially hosted in alkali feldspars.

579 In sand carried by the Himalayan tributaries of the Punjab, most elements – except Si, and Ca in  
 580 Jhelum and Sutlej sands – are depleted relatively to the UCC standard (Fig. 6B), which is typical of  
 581 sand including detritus recycled from sedimentary and metasedimentary rocks. Elements  
 582 preferentially hosted in densest minerals are slightly enriched in the Sutlej (Zr 281 ppm, Eu/Eu\*  
 583 0.43) and Jhelum samples (Zr 230 ppm, Eu/Eu\* 0.60) and slightly depleted in the Chenab sample  
 584 (Zr 123 ppm, Eu/Eu\* 0.72) owing to local differences in heavy-mineral concentration possibly  
 585 caused by moderate selective-entrainment processes.

586 Relatively to Upper Indus sand, Lower Indus sand is depleted in most elements except Si, Ca, and  
 587 P. This reflects major additional contribution from metamorphic and siliciclastic rocks richer in  
 588 quartz. Relatively to Lower Indus River sand, LGM to Holocene deltaic sediments are instead  
 589 enriched in most elements but Si, Y, REE, Zr and Hf, and especially in Al, Fe, Mg, K, Rb, V, Co,  
 590 Ni, Cu, and loss on ignition (Fig. 6B), which is chiefly ascribed to their finer average grain size and  
 591 higher phyllosilicate content.

### 594 6.4. Nd isotopes

596 In modern Indus sand,  $\epsilon_{Nd}$  values have been shown to decrease progressively from -8.4 upstream of  
 597 the western syntaxis to -10.8 upstream of Tarbela Dam, and to -15.0 upstream of the delta,  
 598 documenting a progressive dilution of less radiogenic and unradiogenic sediment generated in the



599 Karakorum and Transhimalayan arcs by more radiogenic sediment derived from the Nanga Parbat  
600 massif and Himalayan belt (Clift et al., 2002). In LGM to Holocene sand of the Indus Delta,  $\epsilon_{Nd}$   
601 varies between -11 and -15 (Clift et al., 2010; Jonell et al., 2018), whereas in turbidites of the Indus  
602 Fan  $\epsilon_{Nd}$  values remained mostly between -8.5 and -11.5 until 5.7 Ma, after which they declined to  
603 between -9 and -12 until 3 Ma and finally to between -11 and -14 thereafter (Clift et al., 2019).

## 605 7. Provenance of Thal Desert sand

606  
607 Based on the detailed compositional information on end-member sources illustrated above, the  
608 relative contributions from each geological domain to eolian sand of the Thal Desert can be  
609 calculated by forward mixing models according to the method illustrated in Garzanti et al. (2012)  
610 and Resentini et al. (2017). These calculations are non-unique and uncertain, being affected by  
611 various sources of error including the imprecise assessment of end-member sources owing to a  
612 limited number of samples and locally significant hydraulic-sorting effects. The calculations also  
613 depend on a variety of premises that are never strictly verified, including the assumption that  
614 selective mechanical or chemical breakdown of detrital components is negligible. The accuracy of  
615 the results thus needs to be increased by performing several independent tests according to different  
616 criteria for each dataset (i.e., petrography and heavy minerals, geochemistry, zircon age spectra, and  
617 Nd isotopes), keeping in mind that each estimate thus obtained refers only to the investigated set of  
618 components and grain-size range (i.e., sand, transparent heavy minerals, zircon, and Nd-rich phases;  
619 Garzanti, 2016). Extrapolating such diverse and not necessarily identical or even similar provenance  
620 budgets to the entire sediment flux, which is a necessary step to calculate sediment yields and  
621 erosion rates in different parts of the catchment, is a challenging endeavour fraught with  
622 uncertainties, which requires careful consideration of mineral fertilities in each source-rock domain  
623 (Malusà et al., 2016).

### 625 7.1. Petrography and heavy minerals

627 The provenance budget based on integrated petrographic and heavy-mineral data from the Upper  
628 Indus catchment and obtained after numerous sets of independent calculations indicated that  
629 bedload sand upstream of Tarbela Dam is predominantly derived from the Karakorum Range  
630 ( $60\pm 6\%$ ), with subordinate and subequal contributions from the Transhimalayan arcs ( $6\pm 4\%$  from  
631 the Ladakh Arc and South Tibet;  $14\pm 4\%$  from the Kohistan Arc) and Himalayan units (Nanga  
632 Parbat  $13\pm 3\%$ ; Tethyan and Greater Himalaya  $6\pm 3\%$ ) (Garzanti et al., 2005 p.296). Sand-budget  
633 estimates are far less precise downstream of Tarbela Dam, because sediment discharge has been  
634 profoundly modified by human activities. Because of effective sediment sequestration in the  
635 Tarbela reservoir, the composition of Indus sand downstream of the Kabul confluence is very close  
636 to Kabul sand, and modern sand at the Salt Range front was estimated to be derived in significant  
637 proportions from the Kabul ( $33\pm 2\%$ ) and Soan Rivers ( $11\pm 2\%$ ) (Garzanti et al., 2005 p.297).  
638 Compared to modern Upper Indus sand, Thal Desert dunes are notably poorer in quartz and  
639 sedimentary to low-rank metasedimentary rock fragments, and richer in feldspars, volcanic,  
640 metavolcanic and metabasite rock fragments, heavy minerals and especially hypersthene,  
641 documenting a significantly greater contribution from the Kohistan arc (Fig. 4). Although precise  
642 estimates are hard to obtain because of strong local selective-entrainment effects caused by wind  
643 deflation and partial overlap among end members, detrital modes of Thal dune sand can be  
644 satisfactorily reproduced as a 36:64 mixture of Kohistan and Upper Indus sand. Thal dune sand is  
645 thus assessed to be derived from the Transhimalayan arcs (40-45%, predominantly from the  
646 Kohistan arc), the Karakorum-Hindukush Ranges (40-50%, at least a third of which *via* the Kabul  
647 River according to suspended-load data of Rehman et al., 1997), the Nanga Parbat massif (< 10%),  
648 and the Himalayan belt (<10%, including detritus recycled by the Soan River).  
649 Further clues are obtained from electron-microprobe mineral-chemical data, which showed that the  
650 Kohistan arc played the principal role as a source of the most common groups of transparent heavy  
651 minerals, especially pyroxene and epidote (Fig. 7). The South Karakorum gneiss domes undergoing  
652 fast exhumation, and to a lesser extent the Nanga Parbat massif, represent important additional

653 sources of amphibole, garnet and zircon, whereas the contribution from other Himalayan domains is  
 654 major only for Lower Indus sand downstream of the Thal Desert (Lee et al., 2003; Alizai et al.,  
 655 2016).

## 656 7.2. Detrital-zircon geochronology

658 In the Upper Indus catchment, Miocene grains were found only in sand of the Braldu and Hushe  
 659 Rivers draining the Baltoro granite. The youngest age population found in Thal Desert (22 Ma; 3%  
 660 of total zircons) and Upper Indus sand (17-21 Ma; 1% of total zircons) are thus most likely derived  
 661 from the Karakorum. Oligocene to Aptian grains (46% of total zircons in both Thal Desert and  
 662 Upper Indus sand) are predominantly derived from the Karakorum Range (peaks at 24-43 Ma and  
 663 99-130 Ma) and Transhimalayan arcs (43-96 Ma). Paleozoic and Neoproterozoic grains (18% and  
 664 30% of total zircons in Thal dunes and Upper Indus sand) are contributed by both Karakorum and  
 665 Himalayan sources, whereas Orosirian grains (peak at 1.85-1.86 Ga; 16% and 7% of total zircons in  
 666 Thal dunes and Upper Indus sand) are chiefly derived from the Nanga Parbat massif (Fig. 5).

667 A set of simple forward mixing calculations based on age groups defined by different criteria and  
 668 choosing different bandwidths indicate that zircons in Thal dune sand are largely derived from the  
 669 Transhimalayan arcs (34-40%), Karakorum-Hindukush Ranges (28-34%), Nanga Parbat massif (20-  
 670 21%), and Himalayan belt (11-12%) (Fig. 8A). Instead, zircon grains in modern Upper Indus sand  
 671 are mostly derived from the Karakorum-Hindukush Ranges (60-66%) and Transhimalayan arcs (17-  
 672 24%), with minor contributions from the Nanga Parbat massif (9%) and the Himalayan belt (7-8%).  
 673 The percentages of zircon grains supplied *via* the Kabul River draining both the Karakorum-  
 674 Hindukush Ranges and the Kohistan arc cannot be estimated accurately, but is most probably  
 675 significant (10-20%), as revealed by the greater percentage of Jurassic/Triassic ages in both Upper  
 676 Indus and Thal Desert sands than in any studied catchment upstream of Tarbela Dam.

## 678 7.3. Sand geochemistry

679  
680  
681  
682  
683  
684  
685

681 The composition of Thal Desert sand compares well with that of modern Upper Indus sand (Fig.  
 682 6A), confirming that they share the same provenance with insignificant supply from the Jhelum  
 683 River or other Himalayan tributaries of the Punjab. Approximate forward mixing calculations based  
 684 on bulk-sediment geochemistry suggest that ~50% of the sand in the Thal dune field may be derived  
 685 from the Karakorum Range, 40% from the Kohistan arc, and only 10% from diverse Himalayan  
 686 sources. This indicates that the Kohistan arc contributed more at those times, and the Himalayan  
 687 belt less, than at present.

#### 689 7.4. Nd isotopes

690 The great intersample variability of  $\epsilon_{Nd}$  values observed in Thal Desert sand – even in samples  
 691 collected less than 30 km apart in the middle of the dune field – cannot be explained by differences  
 692 in provenance. This is thus an exemplary case that highlights the difficulties of decoding the  
 693 provenance signal carried by Nd isotopes, which requires full understanding of the detrital  
 694 components that control the Nd budget as well as of hydraulic-sorting processes (Garçon et al.,  
 695 2014). Moreover, if detritus is derived from multiple tectonic domains with overlapping signatures,  
 696 as it is the case in a large river system such as the Indus draining a complex orogenic belt, then the  
 697 same isotopic ratio can be produced by several different combinations of detrital sources and is  
 698 therefore unable to provide an unequivocal answer (Garzanti, 2016).

699 Based on bulk-sand provenance budgets discussed above in subsections 7.1 and 7.3 and on average  
 700  $\epsilon_{Nd}$  values given in Zhuang et al. (2015) for the Karakorum (-9.6), Ladakh-Kohistan arc (+4.9),  
 701 Greater Himalaya (-14.7) and Nanga Parbat massif (-25; Clift et al., 2002), the expected  $\epsilon_{Nd}$  in Thal  
 702 sand would range between -3.5 and -5.5 (*versus* observed values between -3.5 and -13.2), whereas  
 703 that of Indus sand upstream of Tarbela Dam would be close to -9 (*versus* an observed value of -  
 704 10.8; Clift et al., 2002). Observed values more negative than expected – outside the  $\pm 1$   $\epsilon_{Nd}$   
 705 uncertainty estimated by Jonell et al. (2018) – call for an explanation.

707 Studies of sand generated in the Himalayan orogen have shown that 80-90% of their Nd is  
708 contained in transparent heavy minerals, mostly in allanite and monazite and subordinately in  
709 titanite, apatite, other epidote-group minerals, and amphibole (Garzanti et al., 2010, 2011). The Nd  
710 isotopic signature of orogenic sediment is thus markedly affected by the presence of REE-rich  
711 monazite and allanite grains even where their concentration is very low (Garçon et al., 2014; Jonell  
712 et al., 2018; Garzanti et al., 2019).

713 High-resolution heavy-mineral data obtained with semi-automated Raman spectroscopy (Appendix  
714 Table A4) indicate that REE-rich allanite is most abundant by far in Karakorum-derived sand,  
715 minor in sand from the Greater Himalaya, and rare in sand from the Transhimalayan arcs and  
716 Nanga Parbat massif (Liang et al., 2019), whereas monazite was detected only in sand generated in  
717 the Karakorum and Greater Himalaya. The average  $\epsilon_{Nd}$  value carried by monazite grains is therefore  
718 predicted to be more negative than that carried by allanite. This is corroborated by semi-automated  
719 Raman-point-counting heavy-mineral analysis, which detected significant monazite (0.3 tHM%)  
720 and a little allanite (0.1 tHM%) in sample S1462 yielding the most strongly negative  $\epsilon_{Nd}$  value (-  
721 13.2), a little monazite (0.1 tHM%) and no allanite in sample S1474 yielding the other strongly  
722 negative  $\epsilon_{Nd}$  value (-10.9), and some allanite (0.1 and 0.6 tHM%) but no monazite in samples  
723 S1470 and S1463 yielding the least negative  $\epsilon_{Nd}$  values (-8.7 and -3.5).

724 The results of heavy-mineral point-counting cannot be very precise in this regard, because the  
725 amount of monazite in our sand samples is exceedingly small. Moreover, Nd-bearing minerals may  
726 be present as undetected tiny inclusions in other detrital grains. Nevertheless, because every 100  
727 ppm of monazite hosting  $\sim 10^5$  ppm of Nd contributes  $\sim 10$  ppm of Nd to the bulk sand, our results  
728 suggest that most of the Nd in sample S1462 (containing 30 ppm of Nd overall) and much of the Nd  
729 in sample S1474 (containing only 19 ppm overall) may well be provided by monazite of Greater  
730 Himalayan provenance with an  $\epsilon_{Nd}$  value of  $\sim 15$  (Cottle et al., 2019), thus resulting in unexpectedly  
731 low bulk-sand  $\epsilon_{Nd}$  values of -13.2 and -10.9. A few monazite (or allanite) grains from the Nanga

732 Parbat massif may also be responsible for such a sharp local drop in  $\epsilon_{Nd}$  values. These observations  
 1  
 733 indicate that REE-rich monazite (or allanite) grains carrying a strongly negative  $\epsilon_{Nd}$  fingerprint,  
 3  
 4  
 734 even in amounts so small that seriously challenge the resolution power of current analytical  
 6  
 735 methods, can produce an unexpectedly strong local decrease in  $\epsilon_{Nd}$  values. The uncertainties of  
 8  
 9  
 106 provenance budgets based on bulk-sand Nd isotopes are consequently increased.

## 138 **8. Provenance of Lower Indus, Indus Delta, and Indus Fan sand**

### 180 *8.1. Petrography and heavy minerals*

212 In the Lower Indus catchment, where the sediment flux has been profoundly modified by man,  
 22  
 23  
 243 sediment-budget calculations are affected by large uncertainties. Big dams and link canals, built  
 25  
 264 along both the trunk river and Punjab tributaries since Pakistan's independence in 1947 and  
 27  
 28  
 295 especially after the Indus Waters Treaty in 1960, have greatly hampered sediment transit across the  
 30  
 316 Punjab plains. The entire water discharge of the Ravi and Sutlej Rivers has been retained upstream  
 32  
 33  
 347 in India except during monsoon floods, triggering sediment reworking and erratic mixing and  
 34  
 35  
 368 blurring of provenance signals in Pakistan downstream. All along the eastern edge of the Thal  
 37  
 38  
 399 Desert, changes in composition observed in sand of the Jhelum River and downstream of the  
 39  
 40  
 410 Jhelum–Chenab confluence reveal fluvial reworking of Thal dune sand, which may locally  
 41  
 42  
 431 represent up to more than 20% of river bedload (Garzanti et al., 2005 p.297). Forward mixing  
 44  
 45  
 462 calculations based on the integrated petrographic and mineralogical dataset tentatively indicated a  
 47  
 483 39±4% contribution from the Himalayan tributaries of the Punjab to Lower Indus sand of (15±6%  
 49  
 50  
 514 of which from the Jhelum, 33±7% from the Chenab, 4±4% from the Ravi, 40±8% from the Sutlej,  
 51  
 52  
 535 and 9±3% from reworking of Thal dunes; Garzanti et al., 2005 p.297-298).

54  
 556 Provenance budgets thus suggest relative supply from the Upper Indus and Himalayan tributaries of  
 56  
 57  
 587 the Punjab in proportion 60:40, with very minor additional detritus from the Sulaiman-Kirthar  
 59  
 608 Ranges in the west. These figures are notably similar to what is observed on the eastern side of  
 61  
 62  
 63  
 64  
 65

759 peninsular India, where sediments in the Bengal Delta and Bengal Fan are assessed to be derived  $\geq$   
 760 60% from the Brahmaputra River draining the eastern Himalayan syntaxis and  $\leq$  40% from the  
 761 Ganga River chiefly draining the Himalayan belt, with very minor additional detritus from the Indo-  
 762 Burman Ranges in the east (Lupker et al., 2013; Borromeo et al., 2019; Garzanti et al., 2019). A  
 763 remarkable symmetry in the proportion of sediment generated from the Himalayan belt and carried  
 764 by rivers draining the Himalaya exclusively or dominantly (e.g., Punjab rivers and Ganga) *versus*  
 765 rivers sourced in Tibet and cutting across the western and eastern syntaxes (e.g., Indus and  
 766 Brahmaputra) is thus observed on opposite sides of the India-Asia collision system (figure 5 in  
 767 Garzanti et al., 2005).

768 Given the overall similarity in composition (Fig. 9A), sand budgets based on petrographic and  
 769 heavy-mineral data are not drastically different for the modern Lower Indus, the LGM to Holocene  
 770 Delta, and the early Pleistocene Indus Fan. However, a subtle compositional shift in detrital modes  
 771 from Miocene-Pleistocene deep-sea-fan turbidites to Holocene and modern fluvio-deltaic sands  
 772 points to progressively increasing relative supply from the Himalayan belt (light grey arrow in Fig.  
 773 9B), which is consistent with decreasing  $\epsilon_{Nd}$  values and increasing relative abundance of zircon  
 774 grains older than 300 Ma observed in Indus Fan turbidites since the latest Miocene (Clift et al.,  
 775 2019). At even earlier, mid-Miocene times (18-14 Ma), a sudden influx of volcanic detritus to the  
 776 foreland basin testifies to the onset of rapid exhumation of the Kohistan arc in the western Himalaya  
 777 syntaxis (Kamlial Formation in Fig. 9A; Najman et al., 2003), which is consistent with increasing  
 778  $\epsilon_{Nd}$  values recorded by Indus Fan turbidites from 17 Ma to 9.5 Ma (Clift et al., 2019).

## 8.2. Detrital-zircon geochronology

780 Data from Clift et al. (2004, 2008, 2019) show that zircon grains younger than 125 Ma – which  
 781 account for 47-49% of the zircon population in Upper Indus and Thal Desert sands – are still  
 782 common in LGM to Holocene sand of the Indus Delta (34%) downstream. Young grains are also  
 783 found in the Plio-Quaternary Indus Fan (17%), although they are few in sand carried by Himalayan



786 tributaries of the Punjab (~3%). This indicates that detrital zircon in the modern Lower Indus River,  
 787 LGM to Holocene Delta, and Plio-Quaternary Fan is derived from the Upper Indus and Punjab  
 788 tributaries in roughly similar proportions (Fig. 8B), with notable short-term variations in space and  
 789 time (Clift et al., 2008, 2019; Li et al., 2019). Despite a zircon-age dataset that has been rapidly  
 790 expanded in the last decade, estimates of zircon contributions from various parts of the catchment  
 791 still vary widely. Alizai et al. (2011, their table 7 and figure 12A) estimated that two-thirds of zircon  
 792 grains in the modern delta are supplied by the Himalayan tributaries of the Punjab (two-thirds of  
 793 which by the Sutlej River), which is largely explained by the high zircon fertility of Himalayan  
 794 rocks. Our set of forward mixing calculations, based on age groups defined by diverse criteria,  
 795 suggest that the Upper Indus may have supplied on average 45-48% of detrital zircon to the Plio-  
 796 Quaternary Fan and up to 55-67% of detrital zircon to the LGM-Holocene Delta. Similar, but less  
 797 robust estimates are obtained from Indus Canyon zircon-age data (Li et al., 2019), which is largely  
 798 ascribed to the finer grain-size of the analysed zircons and short timescale variability. The different  
 799 proportions of original cores and rims of zircon grains in samples of markedly different grain size  
 800 may explain the notable variability observed even at the centennial to millennial time scale, which  
 801 may be at least partly caused by the variable grain size of the studied samples rather than by  
 802 provenance changes.

### 8.3. Sand geochemistry

803  
 804 The geochemical composition of modern Lower Indus sand indicates a much higher percentage of  
 805 Himalayan detritus than in Thal Desert and Upper Indus River sands (Fig. 6B). Forward mixing  
 806 calculations, affected by the same uncertainties discussed for the petrographic-mineralogical sand  
 807 budget illustrated in subsection 8.1 above, suggest that the Upper Indus and the Himalayan  
 808 tributaries of the Punjab provide sand in roughly equal amounts to the Lower Indus and LGM to  
 809 Holocene Delta ( $50\pm 8\%$  each).

### 8.4. Nd isotopes



814  
 815 Nd isotopes have long been used to identify sediment sources and to trace erosion patterns in the  
 816 huge Indus drainage basin. In modern Indus River sand, the sharp decrease in  $\epsilon_{Nd}$  values across the  
 817 foreland basin documents the progressive dilution of detritus shed from more juvenile Karakorum  
 818 and Transhimalayan arc sources by more radiogenic Himalayan detritus supplied by the Punjab  
 819 tributaries in the lower course (Clift et al., 2002). Values as negative as -15.4 in the modern delta  
 820 contrast with less negative values measured from Pleistocene Indus Fan sediments cored at ODP  
 821 Site 720 ( $\epsilon_{Nd}$  -12.5 and -14.0; Clift et al., 2001) and IODP Sites U1456 and U1457 ( $\epsilon_{Nd}$  -9.5 and -  
 822 13.0; Clift et al., 2019; Yu et al., 2019). Although this discrepancy may partly result from reduced  
 823 sediment flux from the Upper Indus after the closure of the Tarbela Dam, Indus Delta sediments do  
 824 document a progressive increase of detrital supply from the radiogenic Lesser Himalaya since the  
 825 Last Glacial Maximum (LGM), with relatively reduced contributions from Transhimalayan and  
 826 Karakorum sources. The  $\epsilon_{Nd}$  values decreased from -11 to -12 between the LGM and the beginning  
 827 of the Younger Dryas (~12.7 ka), to reach -15 around -8.7 ka, a change ascribed to enhanced  
 828 erosion along the southern Himalayan front caused by the increasing intensity of summer monsoon  
 829 rains (Clift et al., 2008, 2010).  
 830 Upper Miocene to Pleistocene Indus Fan sediments recently drilled by IODP Expedition 355 to the  
 831 Laxmi Basin also show less radiogenic  $\epsilon_{Nd}$  values than recent sediments in the Indus Delta, with a  
 832 pronounced decline throughout the Pliocene ascribed to an accelerated exhumation of the Lesser  
 833 Himalaya and, to a lesser extent, of the Nanga Parbat massif (Clift et al., 2019). Laxmi Basin  
 834 sediments deposited during the last 600 ka yielded less radiogenic  $\epsilon_{Nd}$  values mostly between -9.5  
 835 and -13.0, which however reflects mixing of sediment supplied not only by the Indus River but also  
 836 by rivers draining Deccan Trap basalts in Peninsular India (Yu et al., 2019), as independently  
 837 documented by heavy-mineral data (Garzanti et al., 2020).

## 9. Climatic control on latest Quaternary erosion patterns

840  
841  
2  
842  
4  
5  
843  
7  
844  
9  
10  
845  
11  
12  
846  
14  
15  
847  
16  
17  
848  
19  
20  
849  
21  
22  
850  
24  
25  
851  
26  
27  
852  
28  
29  
853  
31  
32  
854  
33  
34  
855  
36  
37  
856  
38  
39  
857  
41  
42  
858  
43  
44  
859  
46  
47  
860  
48  
49  
861  
51  
52  
862  
53  
54  
863  
55  
56  
864  
58  
59  
865  
60  
61  
62  
63  
64  
65

In provenance studies, each one of the many different possible approaches adds useful complementary information but hardly ever provides a sharp univocal response. Among bulk-sediment methods, petrographic analysis applies to bedload sand only and geochemistry has limited discrimination power with the notable exception of mafic source rocks. Heavy-mineral suites are strongly affected by hydraulic sorting and selective chemical dissolution during the successive stages of a sedimentary cycle. Age spectra of detrital zircon are strongly distorted by fertility effects and heavily biased in favour of felsic igneous and metaigneous sources; moreover, grains recycled even several times from siliciclastic covers cannot be distinguished from first-cycle grains derived directly from basement rocks. Nd isotopic ratios suffer from overlap among the fingerprints of diverse source-rock domains, are strongly influenced by grain size and hydraulic-sorting effects, and are highly dependent on rare minerals very rich in REE such as monazite, which can control the Nd budget even if present in amounts so small that can hardly be assessed precisely enough by current techniques.

Nevertheless, the evidence provided by these different methods combined, as illustrated in [Sections 4, 5 and 6](#) and discussed in [Sections 7 and 8](#), indicates robustly enough that the Thal dune field was fed entirely by the paleo-Upper Indus at a time when erosion was focused to the north of the Himalayan belt, and specifically in the Kohistan arc and Karakorum Range. All provenance budgets based on integrated petrographic-mineralogical data, bulk-sediment geochemistry, age spectra of detrital zircon, and Nd isotope ratio converge to indicate that Thal Desert sand was originally derived ~40% from erosion of the Kohistan arc, up to 50% from the Karakorum Range, and only in minor amount from diverse Himalayan sources. Instead, ~60% of modern Indus sand upstream of Tarbela Dam is assessed to be derived from the Karakorum, the rest being supplied in subequal amounts by the Transhimalayan arcs and the Himalayan belt.

In Thal Desert sand, the low abundance of quartz and high abundance of feldspars and volcanic, metavolcanic and metabasite rock fragments, the very rich tHM suites including common

866 hypersthene, the common zircon grains of Late Cretaceous to early Paleogene age, and the  $\epsilon_{Nd}$   
 1  
 867 values less negative than those of Upper Indus sand and as high as -3.5 are all clear evidence of  
 3  
 868 major contribution from the Kohistan arc. Notably greater detrital supply from juvenile sources  
 4  
 5  
 6  
 869 lying to the north of the Himalayan belt than in the modern Upper Indus system indicates markedly  
 8  
 870 different conditions of sediment generation at a time when the paleo-Upper Indus delivered to the  
 10  
 11  
 871 foreland basin volumes of sand to be subsequently reworked by wind and accumulated in the Thal  
 12  
 13  
 872 dune field.

### 16 17 18 9.1. Eolian sedimentation in the dry latest Pleistocene

19  
 20  
 21 216 A precise chronology of the evolution of the Thal Desert has not been established yet, whereas  
 22  
 23  
 24  
 25  
 26  
 27  
 28  
 29  
 30  
 31  
 32  
 33  
 34  
 35  
 36  
 37  
 38  
 39  
 40  
 41  
 42  
 43  
 44  
 45  
 46  
 47  
 48  
 49  
 50  
 51  
 52  
 53  
 54  
 55  
 56  
 57  
 58  
 59  
 60  
 61  
 62  
 63  
 64  
 65

217 thermoluminescence dating of eolian sediments in the Thar Desert of southern Pakistan has  
 218 revealed multistep phases of dune accretion through the last 200 ka alternating with precession-  
 219 driven interludes of wetter climate (Singhvi et al., 2010). The last major phase of dune growth in the  
 220 eastern Thar Desert took place under a transitional climate, when SW monsoon winds were being  
 221 re-established following a peak in aridity during the LGM characterized by a very weak SW  
 222 monsoon. Sand aggradation in the eastern desert took place between 17 ka and 14 ka and lasted  
 223 until 9 ka, at the onset of the early Holocene wet stage (Dhir et al., 2010; Singhvi et al., 2010). In  
 224 contrast, the western Thar Desert has been supplied by sediment from the Indus Delta since the  
 225 onset of the wetter Holocene and expanded further west as the climate dried after the mid-Holocene  
 226 (East et al., 2015). The recent finding of Mesolithic artefacts dated as the first millennia of the  
 227 Holocene on top of sand dunes of both Thar and Thal Deserts (Biagi et al., 2019), suggests that a  
 228 chronology similar to the eastern Thar Desert may be extrapolated to the Thal Desert.

229 The compositional fingerprints of Thal dunes indicate that detritus was largely generated by erosion  
 230 in the high Karakorum and Kohistan Ranges in the northern part of the western Himalayan syntaxis  
 231 (Fig. 9A). During deglaciation following the LGM, sediment fluxes were augmented by incision of  
 232 moraines and fluvial terraces in the mountains (Clift and Giosan, 2014; Blöthe et al., 2014; Jonell et

893 [al., 2017b](#)). In this latest Pleistocene period of weak summer monsoonal rains, meltwater fluxes  
 894 from shrinking mountain glaciers were insufficient to guarantee a constant full sediment-transport  
 895 capacity to the paleo-Upper Indus River, fluvial sediments were dumped and extensively reworked  
 896 by wind in the lowlands, and sand blown by progressively strengthening winds accumulated in dune  
 897 fields all across the dry foreland basin ([Fig. 10A](#)).

898 In the Indus Delta, a ravinement surface formed at this time of sea-level rise, as documented by a  
 899 hiatus separating sand deposited during the LGM (radiocarbon ages 28.7 ka and 38.9 ka) from the  
 900 overlying sediments deposited since ~15 ka and documenting sustained progradation since ~12 ka  
 901 ([Clift et al., 2008, 2010](#)). Sediments deposited during and immediately after the LGM carry a  
 902 notably less negative isotopic signature ( $\epsilon_{Nd}$  -11 to -12) than more recent deposits, which confirms a  
 903 greater contribution from juvenile Transhimalayan sources at those times ([Fig. 8B](#)). The  $\epsilon_{Nd}$  values  
 904 started to decrease with the beginning of the Younger Dryas, a consequence of increasingly  
 905 focalized erosion along the southern Himalayan front ([Clift et al., 2010](#)). Changing climatic  
 906 conditions since the LGM have certainly contributed to such a prominent shift in erosion patterns  
 907 and accelerated erosional denudation of the Himalayan belt ([Clift et al., 2008, 2019](#)).

## 909 *9.2. Changing landscapes in the Holocene*

910 Global warming and intensification of the South Asian monsoon led to much wetter conditions in  
 911 the early Holocene, when water and sediment discharge from the Himalayan orogen very markedly  
 912 increased, fuelled by heavier monsoonal rains. This is documented by notably enhanced freshwater  
 913 influx peaking around 10.8 ka, as recorded by low  $\delta^{18}O$  in foraminifera off the coast of Pakistan  
 914 ([Staubwasser et al., 2002](#)) and by progradation of the Indus Delta even at a time of rapid sea-level  
 915 rise, fostered by augmented sediment delivery between 13 ka and 9.5 ka ([Giosan et al., 2006b](#)). On  
 916 the opposite side of Peninsular India, the strengthened early Holocene monsoon is held responsible  
 917 for greatly increased sediment supply to the Bengal Delta between ~11 ka and 7 ka ([Goodbred and](#)  
 918 [Kuehl, 2000](#)). This wet period fostered the formation of lakes in the Thar Desert from ~7 ka to ~5

920 ka (Enzel et al. 1999; Roy et al., 2009). Lakes desiccated at the onset of a new arid phase at ~4 ka  
 1  
 921 (Giosan et al., 2012; Dixit et al., 2014), which was followed by several other wet events of shorter  
 3  
 922 duration and smaller magnitude (Prasad and Enzel, 2006).

6  
 923 The Thal Desert, therefore, testifies to the markedly different landscape that preceded the wet early  
 8  
 924 Holocene, when strongly enhanced water discharge led to incision and reworking of the Thal and  
 10  
 925 Thar dune fields by the Indus and its Punjab tributaries draining the Himalayan front, directly and  
 13  
 926 most strongly hit by the heavy rains brought in by the renewed strength of the South Asian  
 15  
 927 monsoon (Fig. 10B).

## 928 20 929 **10. Conclusions**

22  
 930  
 24  
 931 The distinctive petrographic, heavy-mineral, mineral-chemical, U-Pb zircon-age, geochemical, and  
 25  
 26  
 932 Nd-isotope fingerprints of Thal Desert sand reveal that this dune field was fed entirely by the paleo-  
 28  
 933 Upper Indus at a time when erosion was focused in the Kohistan arc and Karakorum Range to the  
 30  
 934 north of the Himalayan belt. Thermoluminescence chronology and artefacts dated at the first  
 32  
 33  
 935 millennia of the Holocene found on top of sand dunes of both Thal and Thar Deserts indicate that  
 35  
 936 these dune fields expanded in semi-dry climate during the latest Pleistocene. In this period, global  
 37  
 937 warming and glacial retreat following the Last Glacial Maximum fostered enhanced detrital supply  
 40  
 938 from the high Kohistan and Karakorum Ranges of the western Himalayan syntaxis. When  
 42  
 43  
 939 meltwater fluxes from shrinking mountain glaciers were reduced, at a time of weak monsoonal  
 45  
 940 rains, the sediment-transport capacity of the paleo-Upper Indus River was also reduced. Fluvial  
 47  
 941 sediments were dumped and extensively reworked by wind in the lowlands, and sand accumulated  
 50  
 942 in dune fields across the dry foreland basin. Sand stored in the Thal dune field thus testifies to a  
 52  
 943 major change in Himalayan landscape and erosion patterns that took place at a time of rapid  
 54  
 944 climatic transition from dry periglacial settings during the Last Glacial Maximum to wet conditions  
 57  
 945 in the early Holocene, when markedly enhanced river water and sediment discharge was fuelled by  
 59  
 946 intensified monsoonal rainfall.

947  
 948  
 949  
 950  
 951  
 952  
 953  
 954  
 955  
 956  
 957  
 958  
 959  
 960  
 961  
 962  
 963  
 964  
 965  
 966  
 967  
 968  
 969  
 970  
 971  
 972  
 973  
 974  
 975  
 976  
 977  
 978  
 979  
 980  
 981  
 982  
 983  
 984  
 985  
 986  
 987  
 988  
 989  
 990  
 991  
 992  
 993  
 994  
 995  
 996  
 997  
 998  
 999  
 1000

## ACKNOWLEDGMENTS

Heartfelt thanks to Giacomo Ghielmi and Filippo Lazzati, who collected sand samples in the Thal Desert and around the western Himalayan syntaxis, and to Henry Munack and Jan Blöthe who provided samples from Ladakh. The Braldu and Hushe samples were collected and kindly provided by Mike Searle. Guido Pastore helped with several geochronological analyses. This study was supported financially by Projects MIUR-PRIN 2015EC9PJ5 “The subduction and exhumation of the continental lithosphere: their effects on the structure and evolution of the orogens” and MIUR – Dipartimenti di Eccellenza 2018–2022, Department of Earth and Environmental Sciences, University of Milano-Bicocca. We warmly thank ESR Editor Chris Fielding and an anonymous reviewer for their useful comments and constructive advice.

## SUPPLEMENTARY MATERIALS

Supplementary data associated with this article, to be found in the online version at [http://dx.doi.\\_\\_\\_\\_\\_](http://dx.doi._____), include information on sampling sites (Table A1), together with the complete datasets on sand petrography (Table A2), heavy minerals (Table A3), heavy-mineral point-counting by semi-automated Raman spectroscopy (Table A4), percentages of amphibole, garnet, epidote, and pyroxene varieties in each source-rock domain (Table A5), sand geochemistry (Table A6), and Nd isotopes (Table A7). A compilation of Nd isotope values from bedrocks and sediments from the Himalayan-Karakorum orogen is shown in Table A8 and original and literature data on zircon-age distributions are summarized in Table A9, whereas the full original detrital-zircon geochronology dataset is illustrated in Appendix B. The Google-Earth™ map of sampling sites [Thal Review.kmz](#) is also provided.

## 973 FIGURE CAPTIONS

974  
975

976

977

978

979

980

981

982

983

984

985

986

987

988

989

990

991

992

993

994

995

996

997

998

999

1000

1001

1002

1003

1004

1005

1006

1007

1008

1009

1010

1011

1012

1013

1014

1015

1016

1017

1018

1019

1020

1021

1022

1023

1024

1025

1026

1027

1028

1029

1030

1031

1032

1033

**Figure 1.** The Thal Desert is situated where the Upper Indus reaches the foreland basin to the south of the western Himalayan syntaxis (WHS) and to the west of the Punjab plain. Location of the four studied Thal dune samples is indicated by orange stars. Inset shows area enlarged in the Google Earth™ image; the white circle indicates the Indus Canyon, and the white star the location of the Laxmi Basin targeted by IODP Expedition 355. Ga and Br = Ganga and Brahmaputra Rivers.

**Figure 2.** Geological map of the Indus catchment (mod. after [Garzanti et al., 2005](#)) indicating the studied Indus tributaries and sampling sites. Blue stars in the Indus Delta indicate location of the Thatta (T), Jati (J), and Ketu Bandar (K) cores.

**Figure 3.** Sand petrography. Thal Desert sand is enriched in plagioclase, volcanic to metabasite rock fragments, and pyroxenes (**A**; S1462) relative to Upper Indus sand (**B**; S1447). Sand supplied by Punjab tributaries downstream of the Thal Desert includes abundant metasedimentary detritus from the Himalaya (**C**; S1424). Sands in the Lower Indus River (**D**; S1487), Holocene Delta (**E**; sample TH10\_8 in [Clift et al., 2010](#)) and lower Pleistocene Fan (**F**; sample U1456 39F1W130/132, collected during IODP Expedition 355; [Pandey et al., 2016](#)) are notably poorer in feldspars and richer in quartz, metasedimentary rock fragments and micas relatively to Thal dunes. All samples with crossed polarizers; blue bar for scale = 100 μm.

**Figure 4.** Detrital modes of Thal Desert dunes compared with sand carried by the Upper Indus and its tributaries draining the diverse geological domains of the western Himalayan syntaxis (QFL and LmLvLs diagrams after [Ingersoll et al., 1984](#)). Thal dune sand contains more feldspars, more volcanic, metavolcanic, and metabasite rock fragments, more heavy minerals, and more hypersthene than modern Upper Indus sand, indicating greater contribution from the Kohistan arc.



999 Q = quartz; F = feldspar; L = lithic grains (Lm = metamorphic; Lv = volcanic; Ls = sedimentary);  
 1000 other parameters as in [Table 1](#). Data in the LmLvLs and heavy-mineral triangular diagrams are  
 1001 centered to allow better visualization ([von Eynatten et al., 2002](#)).

1002  
 1003 **Figure 5.** U-Pb age spectra of detrital zircons in Thal dunes and in sands carried by the Upper Indus  
 1004 and its tributaries. Zanskar data after [Jonell et al. \(2017a\)](#); Dir and most Upper Hunza ages after  
 1005 [Zhuang et al. \(2018\)](#). Main events of crustal growth in the western Himalayas are indicated. The  
 1006 multimodal spectrum of Thal sand indicates dominant zircon supply from the western Himalayan  
 1007 syntaxis, including the Karakorum Range (Baltoro granite, South Karakorum gneiss domes, and  
 1008 central batholith) and Transhimalayan arcs (ages from 20 to 130 Ma), together with the Nanga  
 1009 Parbat massif (sharp 1.85 Ga peak). Contribution from the Greater and Tethys Himalaya is  
 1010 subordinate (mostly Neoproterozoic ages).

1011  
 1012 **Figure 6.** Sedimentary geochemistry. Elements are arranged following the periodic table group by  
 1013 group and data are normalized to the median composition of average Upper Indus (A) and Lower  
 1014 Indus sand (B) ([Appendix Table A6](#)). **A**) Note: i) similar composition of Thal Desert and Upper  
 1015 Indus sands, which have higher concentration in most chemical elements relatively to Himalayan-  
 1016 derived sand; ii) peculiar composition of Kohistan sand, with high Mg, Sc, V, Co, Ni and Cu, and  
 1017 low Th, U Nb, Ta, and Eu anomaly; iii) low Cr and Ni in Ladakh sand; iv) heavy-mineral  
 1018 enrichment and strongly negative Eu anomaly in Hispar sand, owing to a local selective-  
 1019 entrainment effect. **B**) Note: i) both Thal Desert and Upper Indus sands have higher concentration in  
 1020 most chemical elements than Himalayan-derived sand of Punjab tributaries; ii) high K, Rb, V, Ni  
 1021 and Cu in finer-grained sediments of the LGM to Holocene Indus Delta (data after [Clift et al.,](#)  
 1022 [2010](#)); iii) markedly variable Eu anomaly in both Thal Desert and Punjab tributary sands chiefly  
 1023 controlled by local selective-entrainment effects ([Garzanti et al., 2010](#)).



**Figure 7.** MDS maps based on electron-microprobe chemical analyses of amphibole, garnet, epidote, and pyroxene (mod. after figure 7 in [Liang et al., 2019](#)). The Kohistan arc is indicated as the main supplier of epidote (**A**) and pyroxene (**B**), whereas amphibole (**C**) and garnet (**D**) were largely derived from the Karakorum Range (Hispar River), Nanga Parbat massif, and Himalayan belt.

**Figure 8.** MDS maps based on U-Pb age spectra of detrital zircons highlight focused erosion of the western Himalayan syntaxis at LGM times and increasing contributions from the Himalayan belt in the Holocene. **A**) Thal dunes show a greater affinity with Transhimalayan arcs than Upper Indus sand. Zanskar data after [Jonell et al. \(2017a\)](#); Dir, Kabul, and most Upper Hunza ages after [Zhuang et al. \(2018\)](#). **B**) Sands of the Lower Indus, Thar dunes, and Pleistocene Fan plot close to Himalayan tributaries of the Punjab, showing strong Himalayan influence. Instead, Holocene and especially LGM Delta sands display closer affinity to sands of the Upper Indus, Thal dunes, and Transhimalayan arcs. Data sources: Punjab tributaries and Thar Desert ([Alizai et al., 2011](#)); Lower Indus River ([Clift et al., 2004](#)); LGM to Holocene Indus Delta ([Clift et al., 2008, 2010](#); 4 samples combined from Thatta, Jati, and Keti Bandar cores, age 6.6-9.7 ka, n=288; 2 samples combined from Keti Bandar core, age 28.7 ka, n=229); Indus Canyon ([Li et al., 2019](#); 6 samples combined, age 0.4-6.7 ka, n=507); Indus Fan ([Clift et al., 2019](#); sample U1456A-11H-6 60/69, age 0.9 ka). Eastern Karakorum: Hushe + Braldu samples; western Karakorum: Upper Hunza + Hispar samples.

**Figure 9.** Petrography and heavy minerals in Indus River sands, from the western Himalayan syntaxis to the deep sea. **A**) Quartz increases downstream of the Thal Desert because of major supply from Punjab tributaries draining the Himalayan belt. Rock fragments are dominantly sedimentary in sand from the Kirthar Range but locally include volcanic/metavolcanic and ultramafic types shed by the Waziristan and Zhob ophiolites in sand from the Sulaiman Range. Otherwise, modern sand in the Indus sedimentary system includes a variety of sedimentary and

1051 metamorphic grains with subordinate volcanic/metavolcanic types. Volcanic rock fragments are  
 1052 most abundant in the Kamliyal Formation, reflecting incipient dissection of the Kohistan arc at mid-  
 1053 Miocene times (Najman et al., 2003). **B)** A progressive shift in detrital modes indicates increasing  
 1054 contribution from Himalayan tributaries of the Punjab from Miocene-Pleistocene fan turbidites to  
 1055 Holocene deltaic and modern Lower Indus fluvio-deltaic sands (light grey arrow). Q = quartz; F =  
 1056 feldspar; L = lithic grains; Ky = kyanite; Sil = sillimanite; Sp = Cr-spinel; St = staurolite; other  
 1057 parameters as in Table 1. Data sources: modern sand (Garzanti et al., 2005), LGM to Holocene  
 1058 Delta (Clift et al., 2010), Upper Miocene-Pleistocene Fan, IODP sites U1456 and U1457 (Garzanti  
 1059 et al., 2020).

**Figure 10.** Drastically changing landscapes in the western Himalayan foreland basin driven by  
 latest Quaternary climate change. Pictures in rectangles aim at representing natural sceneries and  
 life conditions at the time, from mountain highlands to the coastal plain. Circles represent rough  
 proportions of detritus contributed by the Upper Indus (orange dots) *versus* the Himalayan  
 tributaries of the Punjab (blue dots). A) In the dry latest Pleistocene, during deglaciation following  
 the LGM, sediment fluxes were largely generated by incision of moraines and fluvial terraces in the  
 high Kohistan and Karakorum Ranges surrounding the western Himalayan syntaxis. B) In the wet  
 early Holocene, water and sediment fluxes were instead largely fuelled by heavy rainfall along the  
 southern front of the Himalayan belt directly hit by humid air masses brought in by the intensified  
 summer monsoon.

**Table 1.** Petrographic and heavy-mineral signatures of Thal Desert sand compared with sands  
 carried by the Indus River and its tributaries draining different source-rock domains. Data sources:  
 Miocene Kamliyal Formation (Najman et al., 2003); Indus Delta cores (Clift et al., 2010); modern  
 Indus sands and Neogene Indus Fan turbidites (Garzanti et al., 2005, 2020). Q = quartz; F =  
 feldspars (KF = K-feldspar; P = plagioclase; L= lithic grains (Lvm = volcanic and metavolcanic; Lc

1077 = carbonate and metacarbonate; Lh = chert; Lsm = shale, siltstone, slate, and metasiltstone; Lmf =  
1078 felsic metamorphic; Lmb = metabasite; Lu = ultramafic); HM = heavy minerals; MI\* =  
1079 Metamorphic Index; tHMC = transparent heavy-mineral concentration. ZTR = zircon + tourmaline  
1080 + rutile; Ttn = titanite; Ep = epidote-group minerals; Grt = garnet; SKS = staurolite + kyanite +  
1081 sillimanite; Amp = amphibole; Px = pyroxene (Cpx = clinopyroxene; Opx = orthopyroxene, mostly  
1082 hypersthene); &tHM = other transparent heavy minerals (apatite, chloritoid, Cr-spinel, olivine,  
1083 prehnite, pumpellyite, brookite, andalusite, barite).

15  
1084  
17  
18  
19  
20  
21  
22  
23  
24  
25  
26  
27  
28  
29  
30  
31  
32  
33  
34  
35  
36  
37  
38  
39  
40  
41  
42  
43  
44  
45  
46  
47  
48  
49  
50  
51  
52  
53  
54  
55  
56  
57  
58  
59  
60  
61  
62  
63  
64  
65

## 1085 REFERENCES

- 1086 Ahmad, T., Harris, N., Bickle, M., Chapman, H., Bunbury, J., Prince, C., 2000. Isotopic constraints  
1087 on the structural relationships between the Lesser Himalayan Series and the High Himalayan  
1088 Crystalline Series, Garhwal Himalaya. *Geological Society of America Bulletin*, 112, 467-477.
- 1089 Ali, K.F., De Boer, D.H., 2007. Spatial patterns and variation of suspended sediment yield in the  
1090 upper Indus River basin, northern Pakistan. *Journal of Hydrology*, 334, 368-387.
- 1091 Ali, K.F., De Boer, D.H., 2008. Factors controlling specific sediment yield in the upper Indus River  
1092 basin, northern Pakistan. *Hydrological Processes*, 22, 3102-3114.
- 1093 Alizai, A., Carter, A., Clift, P.D., Van Laningham, S., Williams, J.C., Kumar, R., 2011. Sediment  
1094 provenance, reworking and transport processes in the Indus River by U–Pb dating of detrital zircon  
1095 grains. *Global and Planetary Change*, 76, 33-55.
- 1096 Alizai, A., Clift, P.D., Still, J., 2016. Indus Basin sediment provenance constrained using garnet  
1097 geochemistry. *Journal of Asian Earth Sciences*, 126, 29-57.
- 1098 Andò, S., Garzanti, E., 2014. Raman spectroscopy in heavy-mineral studies. In: Scott, R.A., Smyth,  
1099 H.R., Morton, A.C., Richardson, N. (Eds.), *Sediment Provenance Studies in Hydrocarbon  
1100 Exploration and Production*. Geological Society: London, UK, Special Publication 386, pp. 395-  
1101 412.
- 1102 Andò, S., Aharonovich, S., Hahn, A., George, S.C., Clift, P.D., Garzanti, E., 2019. Integrating  
1103 heavy-mineral, geochemical, and biomarker analyses of Plio-Pleistocene sandy and silty turbidites:  
1104 a novel approach for provenance studies (Indus Fan, IODP Expedition 355). *Geological Magazine*,  
1105 <https://doi.org/10.1017/S0016756819000773>
- 1106 Argles, T., Foster, G., Whittington, A., Harris, N., George, M., 2003. Isotope studies reveal a  
1107 complete Himalayan section in the Nanga Parbat syntaxis. *Geology*, 31(12), 1109-1112.
- 1108 Badshah, M.S., Gnos, E., Jan, M.Q., Afridi, M.I., 2000. Stratigraphic and tectonic evolution of the  
1109 northwestern Indian plate and Kabul Block. Geological Society, London, Special Publications,  
1110 170, 467-476.
- 1111 Beck, R.A., Burbank, D.W., Sercombe, W.J., Riley, G.W., Barndt, J.K., Berry, J.R., Afzal, J.,  
1112 Khan, A.M., Jurgen, H., Metje, J., Cheema, A., Shafique, N.A., Lawrence, R.D., Khan, M.A.,  
1113 1995. Stratigraphic evidence for an early collision between Northwest India and Asia. *Nature*,  
1114 373 (6509), 55-58.

- 1115 Biagi, P., Starnini, E., Ghauri, Z.S., 2019. Mahi Wala 1 (MW-1): a Mesolithic site in the Thal desert  
 1116 of Punjab (Pakistan). *Asian Archaeology*, <https://doi.org/10.1007/s41826-019-00024-z>.  
 1117
- 1118 Blöthe, J.H., Munack, H., Korup, O., Fülling, A., Garzanti, E., Resentini, A., Kubik, P.W., 2014.  
 1119 Late Quaternary valley infill and dissection in the Indus River, western Tibetan Plateau margin.  
 1120 *Quaternary Science Reviews*, 94, 102-119.  
 1121
- 1122 Borromeo, L., Andò, S., France-Lanord, C., Coletti, G., Hahn, A., Garzanti, E., 2019. Provenance  
 1123 of Bengal Shelf Sediments: 1. Mineralogy and Geochemistry of Silt. *Minerals*, 9, 640,  
 1124 doi:10.3390/min9100640.  
 1125
- 1126 Burbank, D.W., Leland, J., Fielding, E., Anderson, R.S., Brozovic, N., Reid, M.R., Duncan, C.,  
 1127 1996a. Bedrock incision, rock uplift and threshold hillslopes in the northwestern Himalayas.  
 1128 *Nature*, 379, 505-510.  
 1129
- 1130 Burbank, D.W., Beck, R.A., Mulder, T., 1996b. The Himalayan foreland basin. In: Yin, A.,  
 1131 Harrison, T.M. (Eds.), *The Tectonic Evolution of Asia (World and regional geology)*. Cambridge  
 1132 University Press, Cambridge, UK, pp.149-188.  
 1133
- 1134 Burg, J.P., 2011. The Asia–Kohistan–India collision: review and discussion. In: Brown, D., Ryan,  
 1135 P.D. (Eds.), *Arc-Continent Collision, Frontiers in Earth Sciences*, Springer Berlin Heidelberg,  
 1136 pp. 279-309.  
 1137
- 1138 Cervený, P.F., Johnson, N.M., Tahirkheli, R.A.K., Bonis, N.R., 1989. Tectonic and geomorphic  
 1139 implications of Siwalik group heavy minerals, Potwar plateau, Pakistan. In: Malinconico, L.L.,  
 1140 Lillie, R.J. (Eds.), *Tectonics of the Western Himalayas*. Geological Society of America, Special  
 1141 Papers, 232, pp. 129-136.  
 1142
- 1143 Chirouze, F., Huyghe, P., Chauvel, C., van der Beek, P., Bernet, M., Mugnier, J.-L., 2015. Stable  
 1144 drainage pattern and variable exhumation in the Western Himalaya since the Middle Miocene.  
 1145 *The Journal of Geology*, 123, 1-20, doi.org/10.1086/679305.  
 1146
- 1147 Clift, P.D., 2017. Cenozoic sedimentary records of climate-tectonic coupling in the Western  
 1148 Himalaya. *Progress in Earth and Planetary Science*, 4, 39, doi10.1186/s40645-017-0151-8.  
 1149
- 1150 Clift, P.D., Giosan, L., 2014. Sediment fluxes and buffering in the post-glacial Indus Basin. *Basin  
 1151 Research*, 26, 369-386, doi:10.1111/bre.12038.  
 1152

- 1143 Clift, P., Shimizu, N., Layne, G., Gaedicke, C., Schlter, H.U., Clark, M., Amjad, S., 2000. Fifty-five  
1144 million years of Tibetan evolution recorded in the Indus Fan. *Eos, Transactions American*  
1145 *Geophysical Union*, 81, 277-281.  
1146  
1147 Clift, P.D., Shimizu, N., Layne, G., Blusztajn, J.S., Gaedicke, C., Schluter, H.-U., Clark, M.K.,  
1148 Amjad, S., 2001. Development of the Indus Fan and its significance for the erosional history of  
1149 the Western Himalaya and Karakoram. *Geological Society of America Bulletin*, 113, 1039-1051.  
1150  
1151 Clift, P.D., Lee, J.I., Hildebrand, P., Shimizu, N., Layne, G.D., Blusztajn, J., Blum, J.D., Garzanti,  
1152 E., Khan, A.A., 2002. Nd and Pb isotope variability in the Indus River System: implications for  
1153 sediment provenance and crustal heterogeneity in the Western Himalaya. *Earth and Planetary*  
1154 *Science Letters*, 200(1-2), 91-106.  
1155  
1156 Clift, P.D., Campbell, I.H., Pringle, M.S., Carter, A., Zhang, X., Hodges, K.V., Khan, A.A., Allen,  
1157 C.M., 2004. Thermochronology of the modern Indus River bedload: New insight into the  
1158 controls on the marine stratigraphic record. *Tectonics*, 23(5), doi:10.1029/2003TC001559.  
1159  
1160 Clift, P., Giosan, L., Blusztajn, J., Campbell, I.H., Allen, C., Pringle, M., Tabrez, A.R., Danish, M.,  
1161 Rabbani, M.M., Alizai, A., Carter, A., Lückge, A., 2008. Holocene erosion of the Lesser  
1162 Himalaya triggered by intensified summer monsoon. *Geology*, 36, 79-82, doi:  
1163 10.1130/G24315A.1.  
1164  
1165 Clift P.D., Giosan L., Carter A., Garzanti E., Galy V., Tabrez A.R., Pringle M., Campbell I.H.,  
1166 France-Lanord C., Blusztajn J., Allen C., Alizai A., Lückge A., Danish M., Rabbani M.M.,  
1167 2010. Monsoon control over erosion patterns in the Western Himalaya: possible feed-backs into  
1168 the tectonic evolution. In: Clift P.D., Tada R. and Zheng H. (Eds.), *Monsoon evolution and*  
1169 *tectonic-climate linkage in Asia*, Geological Society London, Special Publication 342, pp. 185-  
1170 218.  
1171  
1172 Clift, P.D., Carter, A., Giosan, L., Durcan, J., Duller, G.A., Macklin, M.G., Alizai, A., Tabrez, A.R.,  
1173 Danish, M., Van Laningham, S., Fuller, D.Q., 2012. U-Pb zircon dating evidence for a  
1174 Pleistocene Sarasvati River and capture of the Yamuna River. *Geology*, 40(3), 211-214.  
1175  
1176 Clift, P.D., Zhou, P., Stockli, D.F., Blusztajn, J., 2019. Regional Pliocene exhumation of the Lesser  
1177 Himalaya in the Indus drainage. *Solid Earth*, 10, 647-661.  
1178  
1179 Comas-Cufí, M., Thió-Henestrosa, F.S., 2011. CoDaPack 2.0: a stand-alone, multi-platform  
1180 compositional software.

- 1173 Cottle, J., Lederer, G., Larson, K., 2019. The monazite record of pluton assembly: Mapping  
1174 Manaslu using petrochronology, *Chemical Geology*, 530, 119309,  
1175 <https://doi.org/10.1016/j.chemgeo.2019.119309>.  
1176  
1177 Crawford, M.B., Searle, M.P., 1992. Field relationships and geochemistry of pre-collisional (India-  
1178 Asia) granitoid magmatism in the central Karakoram, northern Pakistan. *Tectonophysics*, 206,  
1179 171-192.  
1180 Critelli, S., Garzanti, E., 1994. Provenance of the Lower Tertiary Murree redbeds (Hazara-Kashmir  
1181 syntaxis, Pakistan) and initial rising of the Himalayas. *Sedimentary Geology*, 89, 265-284.  
1182 Critelli, S., Ingersoll, R.V., 1994. Sandstone petrology and provenance of the Siwalik Group  
1183 (northwestern Pakistan and western-southeastern Nepal). *Journal of Sedimentary Research*, A64,  
1184 815-823.  
1185 Critelli, S., De Rosa, R., Platt, J.P., 1990. Sandstone detrital modes in the Makran accretionary  
1186 wedge, southwest Pakistan: Implications for tectonic setting and long-distance turbidite  
1187 transportation. *Sedimentary Geology*, 68, 241-260.  
1188 Debon, F., Le Fort, P., Dautel, D., Sonet, J., Zimmermann, J.L., 1987. Granites of western  
1189 Karakorum and northern Kohistan (Pakistan): A composite Mid-Cretaceous to upper Cenozoic  
1190 magmatism. *Lithos*, 20(1), 19-40.  
1191 DeCelles, P., Gehrels, G.E., Quade, J., LaReau, B., Spurlin, M., 2000. Tectonic implications of U-  
1192 Pb zircon ages of the Himalayan orogenic belt in Nepal. *Science*, 288, 497-499, doi:  
1193 10.1126/science.288.5465.497.  
1194 DePaolo, D.J., Wasserburg, G.J., 1976. Nd isotopic variations and petrogenetic models.  
1195 *Geophysical Research Letters*, 3, 249-252.  
1196 DiPietro, J.A., Pogue, K.R., 2004. Tectonostratigraphic subdivisions of the Himalaya: A view from  
1197 the west. *Tectonics*, 23, TC5001, doi:10.1029/2003TC001554.  
1198 Dixit, Y., Hodell, D.A., Petrie, C.A., 2014. Abrupt weakening of the summer monsoon in northwest  
1199 India ~4100 yr ago. *Geology*, 42(4), 339-342, doi:10.1130/G35236.1.  
1200 Dhir, R.P., Singhvi, A.K., Andrews, J.E., Kar, A., Sareen, B.K., Tandon, S.K., Kailath, A., Thomas,  
1201 J.V., 2010. Multiple episodes of aggradation and calcrete formation in late Quaternary aeolian  
sands, central Thar Desert, Rajasthan, India. *Journal of Asian Earth Sciences*, 37, 10-16.

- 1202 Downing, K.F., Lindsay, E.H., 2005. Relationship of Chitarwata Formation paleodrainage and  
 1203 paleoenvironments to Himalayan tectonics and Indus River paleogeography. *Palaeontologia*  
 1204 *Electronica*, 8, 1; 20A, 12 p.  
 1205 East, A.E., Clift, P.D., Carter, A., Alizai, A., Van Laningham, S., 2015. Fluvial-eolian interactions  
 1206 in sediment routing and sedimentary signal buffering: an example from the Indus Basin and Thar  
 1207 Desert. *Journal of Sedimentary Research*, 85, 715-728.  
 1208 Enzel, Y., Ely, L.L., Mishra, S., Ramesh, R., Amit, R., Lazar, B., Rajaguru, S.N., Baker, V.R.,  
 1209 Sandler, A., 1999. High-resolution Holocene environmental changes in the Thar Desert,  
 1210 northwestern India. *Science*, 284, 125-128.  
 1211 Fraser, J.E., Searle, M.P., Parrish, R.R., Noble, S.R., 2001. Chronology of deformation,  
 1212 metamorphism, and magmatism in the southern Karakoram Mountains. *Geological Society of*  
 1213 *America Bulletin*, 113 (11), 1443-1455-  
 1214 Gabriel, K.R., 1971. The biplot graphic display of matrices with application to principal component  
 1215 analysis. *Biometrika*, 58, 453-467.  
 1216 Gaetani, M., Garzanti, E., Jadoul, F., Nicora, A., Tintori, A., Pasini, M., Kanwar, S.A.K., 1990, The  
 1217 north Karakorum side of the Central Asia geopuzzle. *Geological Society of America Bulletin*,  
 1218 102, 54-62.  
 1219 Galehouse, J.S., 1971. Point counting, In: Carver, R.E. (ed.), *Procedures in sedimentary petrology*,  
 1220 New York, Wiley, pp. 385-407.  
 1221 Garçon, M., Chauvel, C., France-Lanord, C., Limonta, M., Garzanti, E., 2014. Which minerals  
 1222 control the Nd-Hf-Sr-Pb isotopic compositions of river sediments? *Chemical Geology*, 364, 42-  
 1223 55.  
 1224 Garzanti, E., 2016. From static to dynamic provenance analysis—Sedimentary petrology upgraded.  
 1225 *Sedimentary Geology*, 336, 3-13.  
 1226 Garzanti, E., 2017, The maturity myth in sedimentology and provenance analysis. *Journal of*  
 1227 *Sedimentary Research*, 87, 353-365.  
 1228 Garzanti, E., 2019a. The Himalayan foreland basin from collision onset to the present: a  
 1229 sedimentary-petrology perspective. In: Treloar, P., Searle, M.P. (Eds.), *Himalayan tectonics: a*  
 1230 *modern synthesis*. Geological Society London, Special Publication 483, 65-122, doi.org:  
 1231 10.1144/SP483.17



- 1232 Garzanti, E., 2019b. Petrographic classification of sand and sandstone. *Earth-Science Reviews*, 192,  
1233 545-563.  
2
- 1234 Garzanti, E., Andò, S., 2019. Heavy Minerals for Junior Woodchucks. *Minerals*, 9, 148,  
1235 <https://doi.org/10.3390/min9030148>.  
3  
4  
5  
6  
7
- 1236 Garzanti, E., Resentini, A., 2016. Provenance control on chemical indices of weathering (Taiwan  
1237 river sands). *Sedimentary Geology*, 336, 81-95.  
8  
9  
10  
11
- 1238 Garzanti, E., Van Haver, T., 1988. The Indus clastics: forearc basin sedimentation in the Ladakh  
1239 Himalaya (India). *Sedimentary Geology*, 59(3-4), 237-249.  
12  
13  
14  
15  
16
- 1240 Garzanti, E., Vezzoli, G., 2003. A classification of metamorphic grains in sands based on their  
1241 composition and grade *Journal of Sedimentary Research*, 73, 830-837.  
17  
18  
19  
20  
21
- 1242 Garzanti, E., Casnedi, R., Jadoul, F., 1986. Sedimentary evidence of a Cambro-Ordovician orogenic  
1243 event in the northwestern Himalaya. *Sedimentary Geology*, 48, 237-265.  
22  
23  
24  
25
- 1244 Garzanti, E., Baud, A., Mascle, G., 1987. Sedimentary record of the northward flight of India and  
1245 its collision with Eurasia (Ladakh Himalaya, India). *Geodinamica Acta*, 1, 297-312.  
26  
27  
28  
29  
30
- 1246 Garzanti, E., Critelli, S., Ingersoll, R.V., 1996. Paleogeographic and paleotectonic evolution of the  
1247 Himalayan Range as reflected by detrital modes of Tertiary sandstones and modern sands (Indus  
1248 transect, India and Pakistan). *Geological Society of America Bulletin*, 108, 631-642.  
31  
32  
33  
34  
35  
36
- 1249 Garzanti, E., Vezzoli, G., Andò, S., Paparella, P., Clift, P.D., 2005. Petrology of Indus River sands:  
1250 a key to interpret erosion history of the Western Himalayan Syntaxis. *Earth and Planetary  
1251 Science Letters*, 229, 287-302.  
37  
38  
39  
40  
41  
42
- 1252 Garzanti, E., Andò, S., France-Lanord, C., Vezzoli, G., Najman, Y., 2010. Mineralogical and  
1253 chemical variability of fluvial sediments. 1. Bedload sand (Ganga-Brahmaputra, Bangladesh).  
1254 *Earth Planetary Science Letters*, 299, 368-381.  
43  
44  
45  
46  
47  
48  
49
- 1255 Garzanti, E., Andò, S., France-Lanord, C., Galy, V., Censi, P., Vignola, P., 2011. Mineralogical and  
1256 chemical variability of fluvial sediments. 2. Suspended-load silt (Ganga-Brahmaputra,  
1257 Bangladesh). *Earth and Planetary Science Letters*, 302, 107-120.  
50  
51  
52  
53  
54  
55
- 1258 Garzanti, E., Resentini, A., Vezzoli, G., Andò, S., Malusà, M., Padoan, M., 2012. Forward  
1259 compositional modelling of Alpine orogenic sediments. *Sedimentary Geology*, 280, 149-164.  
56  
57  
58  
59  
60  
61  
62  
63  
64  
65

- 1260 Garzanti, E., Vermeesch, P., Rittner, M. and Simmons, M., 2018. The zircon story of the Nile:  
1261 Time- structure maps of source rocks and discontinuous propagation of detrital signals. *Basin*  
1262 *Research*, 30(6), 1098-1117.
- 1263 Garzanti, E., Andò, S., France-Lanord, C., Limonta, M., Borromeo, L., Vezzoli, G., 2019.  
1264 Provenance of Bengal Shelf Sediments. 2. Petrology of sand. *Minerals*, 9, 642;  
1265 doi:10.3390/min9100642.
- 1266 Garzanti, E., Andò, S., Vezzoli, G., 2020. Provenance of Cenozoic Indus Fan sediments (IODP  
1267 Sites U1456 and U1457). *Journal of Sedimentary Research*, in press.
- 1268 Gehrels, G.E., DeCelles, P.G., Martin, A., Ojha, T.P., Pinhassi, G., Upreti, B.N., 2003. Initiation of  
1269 the Himalayan Orogen as an early Paleozoic thin-skinned thrust belt. *GSA Today*, 13(9), 4-9.
- 1270 Gehrels, G., Kapp, P., DeCelles, P., Pullen, A., Blakey, R., Weislogel, A., Ding, L., Guynn, J.,  
1271 Martin, A., McQuarrie, N., Yin, A., 2011. Detrital zircon geochronology of pre- Tertiary strata  
1272 in the Tibetan- Himalayan orogen. *Tectonics*, 30, TC5016, doi:10.1029/2011TC002868.
- 1273 Giosan, L., Constantinescu, S., Clift, P.D., Tabrez, A.R., Danish, M., Inam, A., 2006a. Recent  
1274 morphodynamics of the Indus delta shore and shelf. *Continental Shelf Research*, 26, 1668-1684.
- 1275 Giosan, L., Clift, P.D., Blusztajn, J., Tabrez, A., Constantinescu, S., Filip, F., 2006b. On the control  
1276 of climate- and human-modulated fluvial sediment delivery on river delta development: The  
1277 Indus. *Eos, Transactions, American Geophysical Union*, 87, AGU Fall Meeting Abstracts,  
1278 OS14A-04.
- 1279 Giosan, L., Clift, P.D., Macklin, M.G., Fuller, D.Q., Constantinescu, S., Durcan, J.A., Stevens, T.,  
1280 Duller, G.A.T., Tabrez, A.R., Gangal, K., Adhikari, R., Alizai, A., Filip, F., Van Laningham, S.,  
1281 Syvitski, J.P.M., 2012. Fluvial landscapes of the Harappan civilization. *Proceedings of the*  
1282 *National Academy of Sciences*, 109, 1688-1694, doi/10.1073/pnas.1112743109.
- 1283 Gnos, E., Immenhauser, A., Peters, T.J., 1997. Late Cretaceous/early Tertiary convergence between  
1284 the Indian and Arabian plates recorded in ophiolites and related sediments. *Tectonophysics*, 271,  
1285 1-19.
- 1286 Goodbred, S.L., Kuehl, S.A., 2000. Enormous Ganges-Brahmaputra sediment discharge during  
1287 strengthened early Holocene monsoon. *Geology*, 28, 1083-1086.
- 1288 Gosal, G., 2004. Physical geography of the Punjab. *Journal of Punjab Studies*, 11, 19-37.

- 1289 Greenman, D.W., Swarzenski, W.V., Bennett, G.D., 1967. Ground-water hydrology of the Punjab,  
 1290 West Pakistan, with emphasis on problems caused by canal irrigation. United States Government  
 1291 Printing Office, Washington, United States Geological Survey, Water-supply paper 1608H, 1-  
 1292 66.
- 1293 Griffin, W.L., Powell, W.J., Pearson, N.J., O'Reilly, S.Y., 2008. GLITTER: data reduction software  
 1294 for laser ablation ICP–MS. In: Sylvester, P. (Ed.), Laser ablation–ICP–MS in the earth sciences:  
 1295 current practices and outstanding issues. Mineralogical Association of Canada, Short Course 40,  
 1296 pp. 204-207.
- 1297 Hamilton, P.J., O'Nions, R.K., Bridgwater, D., Nutman, A.P., 1983. Sm-Nd studies of Archaean  
 1298 metasediments and metavolcanics from west Greenland and their implications for the Earth's  
 1299 early history. *Earth and Planetary Science Letters*, 62, 263-272.
- 1300 Henderson, A.L., Najman, Y., Parrish, R., BouDagher- Fadel, M., Barford, D., Garzanti, E., Andò,  
 1301 S., 2010. Geology of the Cenozoic Indus Basin sedimentary rocks: Paleoenvironmental  
 1302 interpretation of sedimentation from the western Himalaya during the early phases of  
 1303 India- Eurasia collision. *Tectonics*, 29(6), TC6015, doi:10.1029/2009TC002651.
- 1304 Hildebrand, P.R., Noble, S.R., Searle, M.P., Waters, D.J., Parrish, R.R., 2001. Old origin for an  
 1305 active mountain range: Geology and geochronology of the eastern Hindu Kush, Pakistan.  
 1306 *Geological Society of America Bulletin*, 113, 625-639.
- 1307 Hu, X., Garzanti, E., Moore, T., Raffi, I., 2015. Direct stratigraphic dating of India-Asia collision  
 1308 onset at the Selandian (middle Paleocene, 59±1 Ma). *Geology*, 43(10), 859-862.
- 1309 Hubert, J.F., 1962. A zircon–tourmaline–rutile maturity index and the interdependence of the  
 1310 composition of heavy minerals assemblages with the gross composition and texture of  
 1311 sandstones. *Journal of Sedimentary Petrology*, 32, 440-450.
- 1312 Hussain, A., Mir, H., Afzal, M., 2005. Analysis of dust storms frequency over Pakistan during  
 1313 1961-2000. *Pakistan Journal of Meteorology*, 2, 49-68.
- 1314 Hussain, Y., Ullah, S.F., Hussain, M.B., Aslam, A.Q., Akhter, G., Martinez-Carvajal, H., Cárdenas-  
 1315 Soto, M., 2017. Modelling the vulnerability of groundwater to contamination in an unconfined  
 1316 alluvial aquifer in Pakistan. *Environmental Earth Sciences*, 76, 84, doi:10.1007/s12665-017-  
 1317 6391-5.

- 1318 Ingersoll, R.V., Bullard, T.F., Ford, R.L., Grimm, J.P., Pickle, J.D., Sares, S.W., 1984. The effect of  
1319 grain size on detrital modes: a test of the Gazzi-Dickinson point-counting method. *Journal of*  
1320 *Sedimentary Petrology*, 54, 103-116.  
1321
- 1321 Jadoon, I.A., Lawrence, R.D., Lillie, R.J., 1994. Seismic data, geometry, evolution, and shortening  
1322 in the active Sulaiman fold-and-thrust belt of Pakistan, southwest of the Himalayas. *American*  
1323 *Association of Petroleum Geologists Bulletin*, 78, 758-774.  
1324
- 1324 Jagoutz, O.E., Burg, J.P., Hussain, S., Dawood, H., Pettke, T., Iizuka, T., Maruyama, S., 2009.  
1325 Construction of the granitoid crust of an island arc part I: geochronological and geochemical  
1326 constraints from the plutonic Kohistan (NW Pakistan). *Contributions to Mineralogy and*  
1327 *Petrology*, 158, 739-755.  
1328
- 1328 Jagoutz, O., Bouilhol, P., Schaltegger, U., Müntener, O., 2019. The isotopic evolution of the  
1329 Kohistan Ladakh arc from subduction initiation to continent arc collision. In: Treloar, P.J.,  
1330 Searle, M.P. (Eds.), *Himalayan Tectonics: A Modern Synthesis*. Geological Society, London,  
1331 Special Publications, 483, 165-182.  
1332
- 1332 Jipa, D., Kidd, R.B., 1974. Sedimentation of coarser grained interbeds in the Arabian Sea and  
1333 sedimentation processes of the Indus Cone. In: Whitmarsh, R.B., Weser, O.E., Ross, D.A., et  
1334 al. (Eds.), *Initial Report of the Deep Sea Drilling Project 219-230*. Washington, D.C., US  
1335 Government Printing Office, pp. 471-495.  
1336
- 1336 Jonell, T.N., Carter, A., Böning, P., Pahnke, K., Clift, P.D., 2017a. Climatic and glacial impact on  
1337 erosion patterns and sediment provenance in the Himalayan rain shadow, Zaskar River, NW  
1338 India. *Geological Society of America Bulletin*, 129, 820-836.  
1339
- 1339 Jonell, T.N., Owen, L.A., Carter, A., Schwenniger, J. L., Clift, P.D., 2017b. Quantifying episodic  
1340 erosion and transient storage on the western margin of the Tibetan Plateau, upper Indus River.  
1341 *Quaternary Research*, 89(1), 281-306.  
1342
- 1342 Jonell, T.N., Li, Y., Blusztajn, J., Giosan, L., Clift, P.D., 2018. Signal or noise? Isolating grain size  
1343 effects on Nd and Sr isotope variability in Indus delta sediment provenance. *Chemical Geology*,  
1344 485, 56-73.  
1345
- 1345 Kadri, I.B., 1995. *Petroleum Geology of Pakistan*. Pakistan Petroleum Limited (275 pp.).  
1346
- 1346 Khan, I.A., Bridge, J.S., Kappelman, J., Wilson, R., 1997a. Evolution of Miocene fluvial  
1347 environments, eastern Potwar plateau, northern Pakistan. *Sedimentology*, 44, 221-251.  
1348  
1349  
1350  
1351  
1352  
1353  
1354  
1355  
1356  
1357  
1358  
1359  
1360  
1361  
1362  
1363  
1364  
1365

- 1348 Khan, M.A., Stern, R.J., Gribble, R.F., Windley, B.F., 1997b. Geochemical and isotopic constraints  
 1349 on subduction polarity, magma sources and palaeogeography of the Kohistan intra-oceanic arc,  
 1350 northern Pakistan Himalayas. *Journal of the Geological Society, London*, 154, 935-946.  
 1351  
 1352 Kruskal, J., 1964. Multidimensional scaling by optimizing goodness of fit to a nonmetric  
 1353 hypothesis. *Psychometrika*, 29, 1-27.  
 1354  
 1355 Lee, J.I., Clift, P.D., Layne, G., Blum, J., Khan, A.A., 2003. Sediment flux in the modern Indus  
 1356 River inferred from the trace element composition of detrital amphibole grains. *Sedimentary  
 1357 Geology*, 160, 243-257.  
 1358  
 1359 Li, Y., Clift, P.D., O'Sullivan, P., 2019. Millennial and centennial variations in zircon U- Pb ages in  
 1360 the Quaternary Indus submarine canyon. *Basin Research*, 31, 155-170.  
 1361  
 1362 Liang, W., Garzanti, E., Andò, S., Gentile, P., Resentini, A., 2019. Multiminerall fingerprinting of  
 1363 Transhimalayan and Himalayan sources to Indus-derived Thal Desert sand (central Pakistan).  
 1364 *Minerals*, 9, 457, doi:10.3390/min9080457.  
 1365  
 1366 Lünsdorf, N.K., Kalies, J., Ahlers, P., Dunkl, I., von Eynatten, H., 2019. Semi-automated heavy-  
 1367 mineral analysis by Raman spectroscopy. *Minerals*, 9, 385, doi.org/10.3390/min9070385.  
 1368  
 1369 Lupker, M., France-Lanord, C., Galy, V., Lavé, J., Kudrass, H., 2013. Increasing chemical  
 1370 weathering in the Himalayan system since the Last Glacial Maximum. *Earth and Planetary  
 1371 Science Letters*, 365, 243-252.  
 1372  
 1373 Mahar, M.A., Mahéo, G., Goodell, P.C., Pavlis, T.L., 2014. Age and origin of post collision Baltoro  
 1374 granites, south Karakoram, North Pakistan: Insights from in-situ U–Pb, Hf and oxygen isotopic  
 1375 record of zircons. *Lithos*, 205, 341-358.  
 1376  
 1377 Mahéo, G., Blichert-Toft, J., Pin, C., Guillot, S., Pêcher, A., 2009. Partial melting of mantle and  
 1378 crustal sources beneath South Karakorum, Pakistan: Implications for the Miocene geodynamic  
 1379 evolution of the India–Asia convergence zone. *Journal of Petrology*, 50, 427-449.  
 1380  
 1381 Mallik, T.K., 1978, Mineralogy of deep-sea sands of the Indian Ocean. *Marine Geology*, 27, 161-  
 1382 176.  
 1383  
 1384 Malusà, M.G., Resentini, A., Garzanti, E., 2016. Hydraulic sorting and mineral fertility bias in  
 1385 detrital geochronology. *Gondwana Research*, 31, 1-19.  
 1386  
 1387 Mange, M.A., Maurer, H.F.W., 1992, Heavy minerals in colour. Chapman and Hall, London. (147  
 1388 pp.).

- 1378 Mange, M.A., Morton, A.C., 2007. Geochemistry of heavy minerals. In: Mange, M.A., Wright,  
1379 D.T. (Eds.), *Heavy Minerals in Use*. Elsevier, Amsterdam, *Developments in Sedimentology*, 58,  
1380 pp. 345-391.  
4
- 1381 Meadows, A., Meadows, P., 1999. *The Indus River: Biodiversity, Resources, Humankind*. Oxford  
1382 University Press (441 pp.).  
5
- 1383 Miller, C., Klötzli, U., Frank, W., Thöni, M., Grasemann, B., 2000. Proterozoic crustal evolution in  
1384 the NW Himalaya (India) as recorded by circa 1.80 Ga mafic and 1.84 Ga granitic magmatism.  
1385 *Precambrian Research*, 103(3-4), 191-206.  
6
- 1386 Miller, C., Thöni, M., Frank, W., Grasemann, B., Klötzli, U., Guntli, P., Draganits, E., 2001. The  
1387 early Palaeozoic magmatic event in the Northwest Himalaya, India: source, tectonic setting and  
1388 age of emplacement. *Geological Magazine*, 138(3), 237-251.  
7
- 1389 Milliman, J.D., Quraishee, G.S. Beg, M.A.A., 1984. Sediment discharge from the Indus River to the  
1390 ocean: past, present, and future. In: Haq, B.U., Milliman, J.D. (Eds.), *Marine Geology and*  
1391 *Oceanography of the Arabian Sea and Coastal Pakistan*. Van Nostrand Reynolds, New York, pp.  
1392 65-70.  
8
- 1393 Munack, H., Korup, O., Resentini, A., Limonta, M., Garzanti, E., Blöthe, J.H., Scherler, D.,  
1394 Wittmann, H., Kubik, P.W., 2014. Postglacial denudation of western Tibetan Plateau margin  
1395 outpaced by long-term exhumation. *Geological Society of America Bulletin*, 126, 1580-1594.  
9
- 1396 Najman, Y., Garzanti, E., Pringle, M., Bickle, M., Stix, J., Khan, I., 2003. Early-Middle Miocene  
1397 paleodrainage and tectonics in the Pakistan Himalaya. *Geological Society of America Bulletin*,  
1398 115, 1265-1277.  
10
- 1399 Nickson, R.T., McArthur, J.M., Shrestha, B., Kyaw-Myint, T.O., Lowry, D., 2005. Arsenic and  
1400 other drinking water quality issues, Muzaffargarh District, Pakistan. *Applied Geochemistry*, 20,  
1401 55-68.  
11
- 1402 Pandey, D.K., Clift, P.D., Kulhanek, D.K. & Expedition 355 Scientists, 2016. Expedition 355  
1403 summary. *Arabian Sea Monsoon*. In: Pandey, D.K., Clift, P.D., Kulhanek, D.K. & Expedition  
1404 355 Scientists (Eds.), *Expedition 355 Scientific Prospectus: Arabian Sea Monsoon*. Proceedings  
1405 of the International Ocean Discovery Program, Volume 355. International Ocean Discovery  
1406 Program, College Station, TX, 1-32, <https://doi.org/10.14379/iodp.proc.355.101.2016>.  
12

- 1407 Parrish, R.R., Hodges, V., 1996. Isotopic constraints on the age and provenance of the Lesser and  
 1408 Greater Himalayan sequences, Nepalese Himalaya. *Geological Society of America Bulletin*, 108,  
 1409 904-911.  
 1410
- 1410 Pêcher, A., Seeber, L., Guillot, S., Jouanne, F., Kausar, A., Latif, M., Majid, A., Mahéo, G.,  
 1411 Mugnier, J.L., Rolland, Y., van der Beek, P., Van Melle, J., 2008. Stress field evolution in the  
 1412 northwest Himalayan syntaxis, northern Pakistan. *Tectonics*, 27, TC6005,  
 1413 doi:10.1029/2007TC002252.  
 1414
- 1414 Petterson, M.G., M.B. Crawford, B.F. Windley, 1993. Petrogenetic implications of neodymium  
 1415 isotope data from the Kohistan Batholith, North Pakistan, *Journal of the Geological Society*,  
 1416 London, 150, 125-129.  
 1417
- 1417 Prasad, B.R., Klemperer, S.L., Rao, V.V., Tewari, H.C., Khare, P., 2011. Crustal structure beneath  
 1418 the Sub-Himalayan fold–thrust belt, Kangra recess, northwest India, from seismic reflection  
 1419 profiling: Implications for Late Paleoproterozoic orogenesis and modern earthquake hazard.  
 1420 *Earth and Planetary Science Letters*, 308(1-2), 218-228.  
 1421
- 1421 Prasad, S., Enzel, Y., 2006. Holocene palaeoclimates of India. *Quaternary Research*, 66, 442-453.  
 1422
- 1422 Qayyum, M., Lawrence, R.D., Niem, A.R., 1997. Discovery of the palaeo-Indus delta-fan complex.  
 1423 *Journal of the Geological Society London*, 154, 753-756, doi: 10.1144/gsjgs.154.5.0753.  
 1424
- 1424 Ravikant, V., Wu, F.Y., Ji, W.Q., 2009. Zircon U–Pb and Hf isotopic constraints on petrogenesis of  
 1425 the Cretaceous–Tertiary granites in eastern Karakoram and Ladakh, India. *Lithos*, 110(1-4), 153-  
 1426 166.  
 1427
- 1427 Rehman, S.S., Sabir, M.A., Khan, J., 1997. Discharge characteristics and suspended load from  
 1428 rivers of Northern Indus Basin, Pakistan. *Geological Bulletin University of Peshawar*, 30, 325-  
 1429 336.  
 1430
- 1430 Resentini, A., Goren, L., Castelltort, S., Garzanti, E., 2017. Partitioning the sediment flux by  
 1431 provenance and tracing erosion patterns in Taiwan. *Journal Geophysical Research - Earth  
 1432 Surface*, 122, 1430-1454, doi:10.1002/2016JF004026.  
 1433
- 1433 Roddaz, M., Said, A., Guillot, S., Antoine, P.O., Montel, J.M., Martin, F., Darrozes, J., 2011.  
 1434 Provenance of Cenozoic sedimentary rocks from the Sulaiman fold and thrust belt, Pakistan:  
 1435 implications for the palaeogeography of the Indus drainage system. *Journal of the Geological  
 1436 Society*, 168, 499-516.  
 1437

- 1437 Rolland, Y., Mahéo, G., Guillot, S., Pêcher, A., 2001. Tectono-metamorphic evolution of the  
1438 Karakorum metamorphic complex (Dassu-Askole area, NE Pakistan): exhumation of mid-crustal  
2 HT–MP gneisses in a convergent context. *Journal of Metamorphic Geology*, 19, 717-737.  
1439  
4
- 1440 Rolland, Y., Picard, C., Pêcher, A., Lapierre, H., Bosch, D., Keller, F., 2002. The Cretaceous  
1441 Ladakh arc of NW Himalaya—slab melting and melt-mantle interaction during fast northward  
1442 drift of Indian Plate. *Chemical Geology*, 182, 139-178.  
1443  
10
- 1443 Roy, P.D., Nagar, Y.C., Juyal, N., Smykatz-Kloss, W., Singhvi, A.K., 2009. Geochemical  
1444 signatures of Late Holocene paleohydrological changes from Phulera and Pokharan saline playas  
1445 near the eastern and western margins of the Thar Desert, India. *Journal of Asian Earth Sciences*  
1446 34, 275-286.  
1447  
18
- 1447 Rudnick, R.L., Gao, S., 2003. Composition of the continental crust. In: Rudnick, R.L., Holland,  
1448 H.D., Turekian, K.K. (Eds.), *Treatise on Geochemistry, The Crust*. Elsevier Pergamon, Oxford,  
1449 UK, Vol. 3, pp. 1–64.  
1450  
25
- 1450 Schärer, U., Copeland, P., Harrison, T. M., Searle, M.P., 1990. Age, cooling history, and origin of  
1451 post-collisional leucogranites in the Karakoram Batholith; a multi-system isotope study. *The*  
1452 *Journal of Geology*, 98(2), 233-251.  
1453  
31
- 1453 Schaltegger, U., Zeilinger, G., Frank, M., Burg, J.P., 2002. Multiple mantle sources during island  
1454 arc magmatism: U–Pb and Hf isotopic evidence from the Kohistan arc complex, Pakistan. *Terra*  
1455 *Nova*, 14(6), 461-468.  
1456  
37
- 1456 Schneider, D.A., Zeitler, P.K., Kidd, W.S.F., Edwards, M.A., 2001. Geochronologic constraints on  
1457 the tectonic evolution and exhumation of Nanga Parbat, western Himalaya syntaxis, revisited.  
1458 *The Journal of Geology*, 109, 563-583.  
1459  
44
- 1459 Searle, M.P., 2013. *Colliding continents: a geological exploration of the Himalaya, Karakoram, and*  
1460 *Tibet*. Oxford University Press, Oxford UK, 438 p.  
1461  
49
- 1461 Searle, M.P., Khan, M.A., Fraser, J.E., Gough, S.J., Jan, M.Q., 1999. The tectonic evolution of the  
1462 Kohistan- Karakoram collision belt along the Karakoram Highway transect, north Pakistan.  
1463 *Tectonics*, 18, 929-949.  
1464  
55
- 1464 Searle, M.P., Parrish, R.R., Thow, A.V., Noble, S.R., Phillips, R.J., Waters, D.J., 2010. Anatomy,  
1465 age and evolution of a collisional mountain belt: the Baltoro granite batholith and Karakoram  
1466  
59  
60  
61  
62  
63  
64  
65



- 1466 Metamorphic Complex, Pakistani Karakoram. *Journal of the Geological Society London*, 167,  
1467 183-202.  
2  
3
- 1468 Shah, S.M.I., 1977. Stratigraphy of Pakistan. Geological Survey of Pakistan, Memoir, 12, 138 p.  
4  
5
- 1469 Shah, Z.U.H., Ahmad, Z., 2015. Hydrochemical mapping of the Upper Thal Doab (Pakistan) using  
6  
7 the geographic information system. *Environmental Earth Sciences*, 74, 2757-2773.  
8  
9
- 1470  
10  
1471 Shah, Z.U.H., Ahmad, Z., 2016. Hydrogeology and hydrochemistry of the Upper Thal Doab  
11  
12 (Pakistan). *Environmental Earth Sciences*, 75(6), 527, doi: 10.1007/s12665-015-5211-z.  
13  
14
- 1473 Shroder, J.F., Bishop, M.P., 2000. Unroofing of Nanga Parbat Himalaya. In: Khan M.A., Treloar  
15  
16 P.J., Searle M.P., Jan M.Q. (Eds.), *Tectonics of the Nanga Parbat Syntaxis and the Western  
17  
18 Himalaya*. Geological Society, London, Special Publication, 170, pp. 163-179.  
19  
20
- 1475  
21  
1476 Singh, G., Wasson, R.J., Agrawal, D.P., 1990. Vegetational and seasonal climatic changes since the  
22  
23 last full glacial in the Thar Desert, northwestern India. *Review of Palaeobotany and  
24  
25 Palynology*, 64(1-4), 351-358.  
26  
27
- 1479 Singh, S., Kumar, R., Barley, M.E., Jain, A.K., 2007. SHRIMP U–Pb ages and depth of  
28  
29 emplacement of Ladakh Batholith, Eastern Ladakh, India. *Journal of Asian Earth Sciences*, 30(3-  
30  
31 4), 490-503.  
32  
33
- 1482 Singh, S., Jain, A.K., Barley, M.E., 2009. SHRIMP U-Pb c.1860 Ma anorogenic magmatic  
34  
35 signatures from the NW Himalaya: implications for Palaeoproterozoic assembly of the Columbia  
36  
37 Supercontinent. In: Reddy, S.M., Mazumder, R., Evans, D.A.D., Collins, A.S. (Eds.),  
38  
39 *Palaeoproterozoic Supercontinents and Global Evolution*. Geological Society, London, Special  
40  
41 Publications, 323, 283-300.  
42  
43
- 1484  
44  
1487 Singhvi, A. K., Kar, A., 2004. The aeolian sedimentation record of the Thar Desert. *Journal of Earth  
45  
46 System Science*, 113, 371-401.  
47  
48
- 1489 Singhvi, A.K., Williams, M.A.J., Rajaguru, S.N., Misra, V.N., Chawla, S., Stokes, S., Chauhan, N.,  
49  
50 Francis, T., Ganjoo, R.K., Humphreys, G.S., 2010. A ~200 ka record of climatic change and  
51  
52 dune activity in the Thar Desert, India. *Quaternary Science Reviews*, 29, 3095-3105.  
53  
54
- 1492 Staubwasser, M., Sirocko, F., Grootes, P.M., Erlenkeuser, H., 2002. South Asian monsoon climate  
55  
56 change and radiocarbon in the Arabian Sea during early and middle Holocene.  
57  
58 *Paleoceanography*, 17(4), 1063, doi:10.1029/2000PA000608.  
59  
60  
61  
62  
63  
64  
65

- 1495 St-Onge, M.R., Rayner, N., Searle, M.P., 2010. Zircon age determinations for the Ladakh batholith  
1496 at Chumathang (Northwest India): Implications for the age of the India–Asia collision in the  
1497 Ladakh Himalaya. *Tectonophysics*, 495(3-4), 171-183.
- 1498 Suczek, C.A., Ingersoll, R.V., 1985. Petrology and provenance of Cenozoic sand from the Indus  
1499 Cone and the Arabian Basin, DSDP sites 221, 222, and 224. *Journal of Sedimentary  
1500 Petrology*, 55(3), 340-346.
- 1501 Tate, E.L., Farquharson, F.K., 2000. Simulating reservoir management under the threat of  
1502 sedimentation: The case of Tarbela Dam on the River Indus. *Water Resources Management*, 14  
1503 191-208.
- 1504 Taylor, S.R., McLennan, S.M., 1995. The geochemical evolution of the continental crust. *Review of  
1505 Geophysics*, 33, 241–265.
- 1506 Treloar, P.J., Petterson, M.G., Jan, M.Q., Sullivan, M.A., 1996. A re-evaluation of the stratigraphy  
1507 and evolution of the Kohistan arc sequence, Pakistan Himalaya: implications for magmatic and  
1508 tectonic arc-building processes. *Journal of the Geological Society London*, 153, 681-693.
- 1509 Vermeesch, P., 2012. On the visualisation of detrital age distributions. *Chemical Geology*, 312,  
1510 190-194.
- 1511 Vermeesch, P., 2013. Multi-sample comparison of detrital age distributions. *Chemical Geology*,  
1512 341, 140-146.
- 1513 Vermeesch, P., 2018. Dissimilarity measures in detrital geochronology. *Earth-Science Reviews*,  
1514 178, 310-321.
- 1515 Vermeesch, P., Garzanti, E., 2015. Making geological sense of ‘Big Data’ in sedimentary  
1516 provenance analysis. *Chemical Geology*, 409, 20-27.
- 1517 Vermeesch, P., Resentini, A., Garzanti, E., 2016. An R package for statistical provenance analysis.  
1518 *Sedimentary Geology*, 336, 14-25.
- 1519 Vermeesch, P., Rittner, M., Petrou, E., Omma, J., Mattinson, C., Garzanti, E., 2017. High  
1520 throughput petrochronology and sedimentary provenance analysis by automated phase mapping  
1521 and LAICPMS. *Geochemistry, Geophysics, Geosystems*, 18, 4096-4109, doi:  
1522 10.1002/2017GC007109.

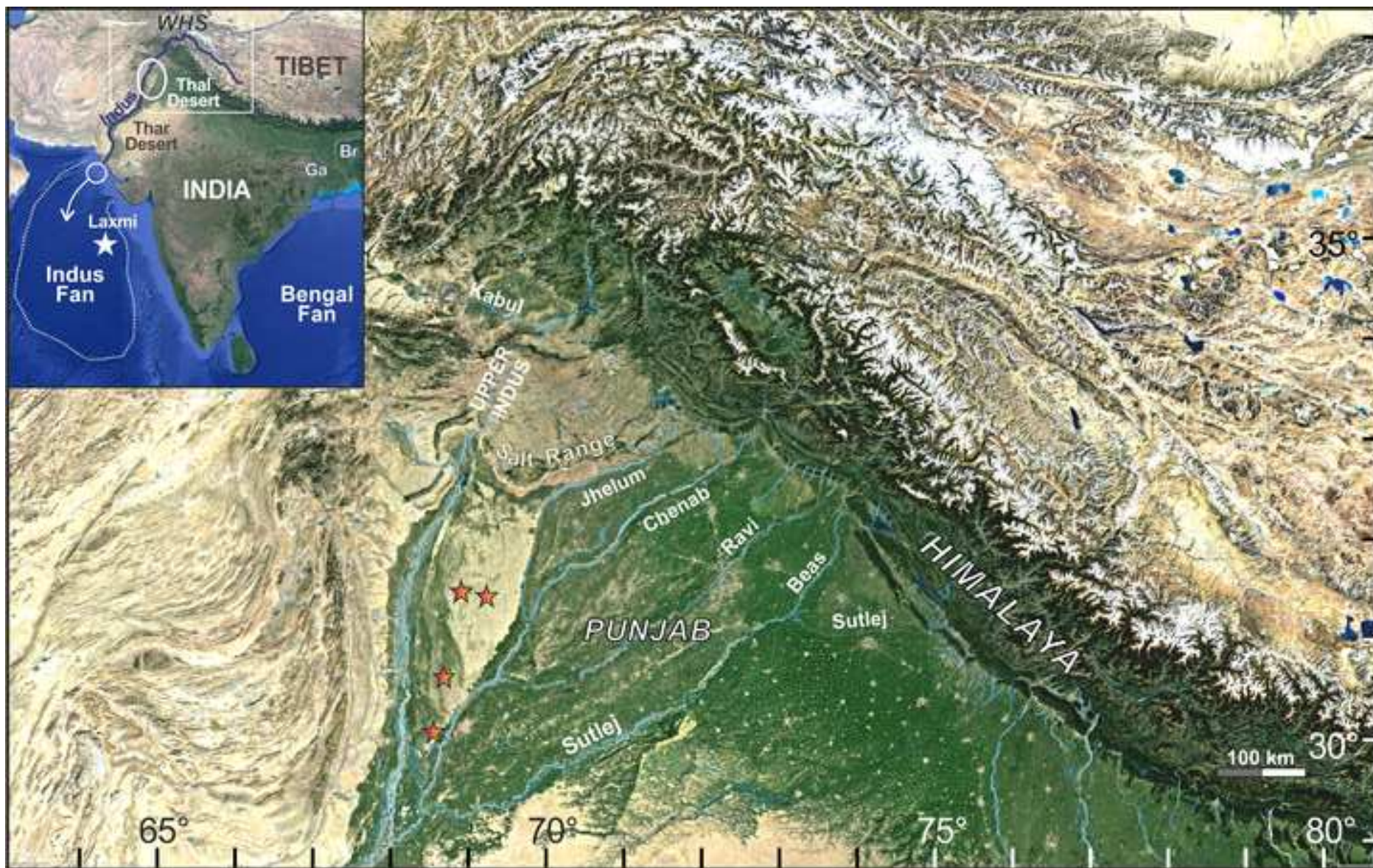
- 1523 Von Eynatten, H., Pawlowsky-Glahn, V., Egozcue, J.J., 2002. Understanding perturbation on the  
1524 simplex: A simple method to better visualize and interpret compositional data in ternary  
2  
1525 diagrams. *Mathematical Geology*, 34(3), 249-257.  
4
- 1526 Weinberg, R.F., Dunlap, W.J., 2000. Growth and deformation of the Ladakh Batholith, Northwest  
5  
1527 Himalayas: implications for timing of continental collision and origin of calc-alkaline batholiths.  
6  
7  
8  
1528 *The Journal of Geology*, 108, 303-320.  
9
- 1529 Whittington, A., Foster, G., Harris, N., Vance, D., Ayres, M., 1999. Lithostratigraphic correlations  
10  
11  
12  
13  
14  
1529 in the western Himalaya; an isotopic approach. *Geology* 27, 585-588.  
15
- 1530 Whittington, A., Harris, N.B.W., Ayres, M.W., Foster, G., 2000. Tracing the origins of the western  
16  
17  
18  
19  
20  
21  
22  
23  
1531 Himalaya: an isotopic comparison of the Nanga Parbat massif and Zaskar Himalaya. In: Khan,  
1532 M.A., Treloar, P.J., Searle, M.P., Jan, M.Q. (Eds.), *Tectonics of the Nanga Parbat Syntaxis and*  
24  
25  
26  
27  
28  
29  
30  
31  
32  
33  
34  
35  
36  
37  
38  
39  
40  
41  
42  
43  
44  
45  
46  
47  
48  
49  
50  
51  
52  
53  
54  
55  
56  
57  
58  
59  
60  
61  
62  
63  
64  
65
- 1535 Yu, Z., Colin, C., Wan, S., Saraswat, R., Song, L., Xu, Z., Clift, P.D., Lu, H., Lyle, M., Kulhanek,  
1536 D., Hahn, A., Tiwari, M., Mishra, R., Miska, S., Kumar, A., 2019. Sea level-controlled sediment  
1537 transport to the eastern Arabian Sea over the past 600 kyr: Clay minerals and SrNd isotopic  
1538 evidence from IODP site U1457. *Quaternary Science Reviews*, 205, 22-34.
- 1539 Zeitler, P.K., Chamberlain, C.P., Smith, H.A., 1993. Synchronous anatexis, metamorphism, and  
1540 rapid denudation at Nanga Parbat (Pakistan Himalaya). *Geology*, 21, 347-350.
- 1541 Zeitler, P.K., Meltzer, A.S., Koons, P.O., Craw, D., Hallet, B., Chamberlain, C.P., Kidd, W.S.,  
1542 Park, S.K., Seeber, L., Bishop, M., Shroder, J., 2001. Erosion, Himalayan geodynamics, and the  
1543 geomorphology of metamorphism. *GSA Today*, 11, 4-9.
- 1544 Zhuang, G., Najman, Y., Guillot, S., Roddaz, M., Antoine, P.O., Métais, G., Carter, A., Marivaux,  
1545 L., Solangi, S.H., 2015. Constraints on the collision and the pre-collision tectonic configuration  
1546 between India and Asia from detrital geochronology, thermochronology, and geochemistry  
1547 studies in the lower Indus basin, Pakistan. *Earth and Planetary Science Letters*, 432, 363-373.
- 1548 Zhuang, G., Najman, Y., Tian, Y., Carter, A., Gemignani, L., Wijbrans, J., Jan, M.Q., Khan, M.A.,  
1549 2018. Insights into the evolution of the Hindu Kush–Kohistan–Karakoram from modern river  
1550 sand detrital geo- and thermochronological studies. *Journal of the Geological Society*  
1551 London, 175(6), 934-948.

1553

1  
2  
3  
4  
5  
6  
7  
8  
9  
10  
11  
12  
13  
14  
15  
16  
17  
18  
19  
20  
21  
22  
23  
24  
25  
26  
27  
28  
29  
30  
31  
32  
33  
34  
35  
36  
37  
38  
39  
40  
41  
42  
43  
44  
45  
46  
47  
48  
49  
50  
51  
52  
53  
54  
55  
56  
57  
58  
59  
60  
61  
62  
63  
64  
65



Figure 1









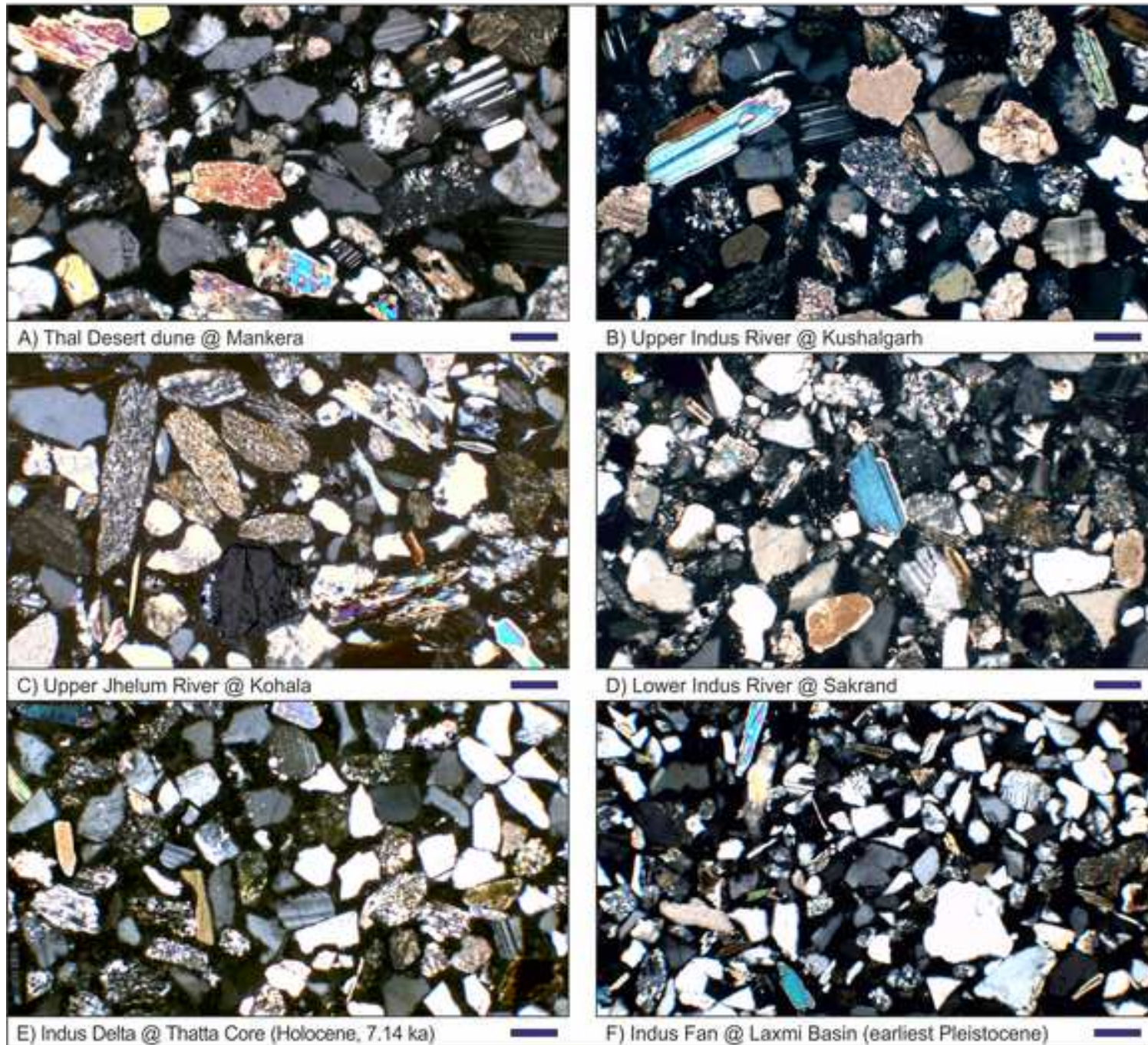




Figure 4

[Click here to access/download;Figure;Figure 4 Thal Review PTHM.jpg](#)

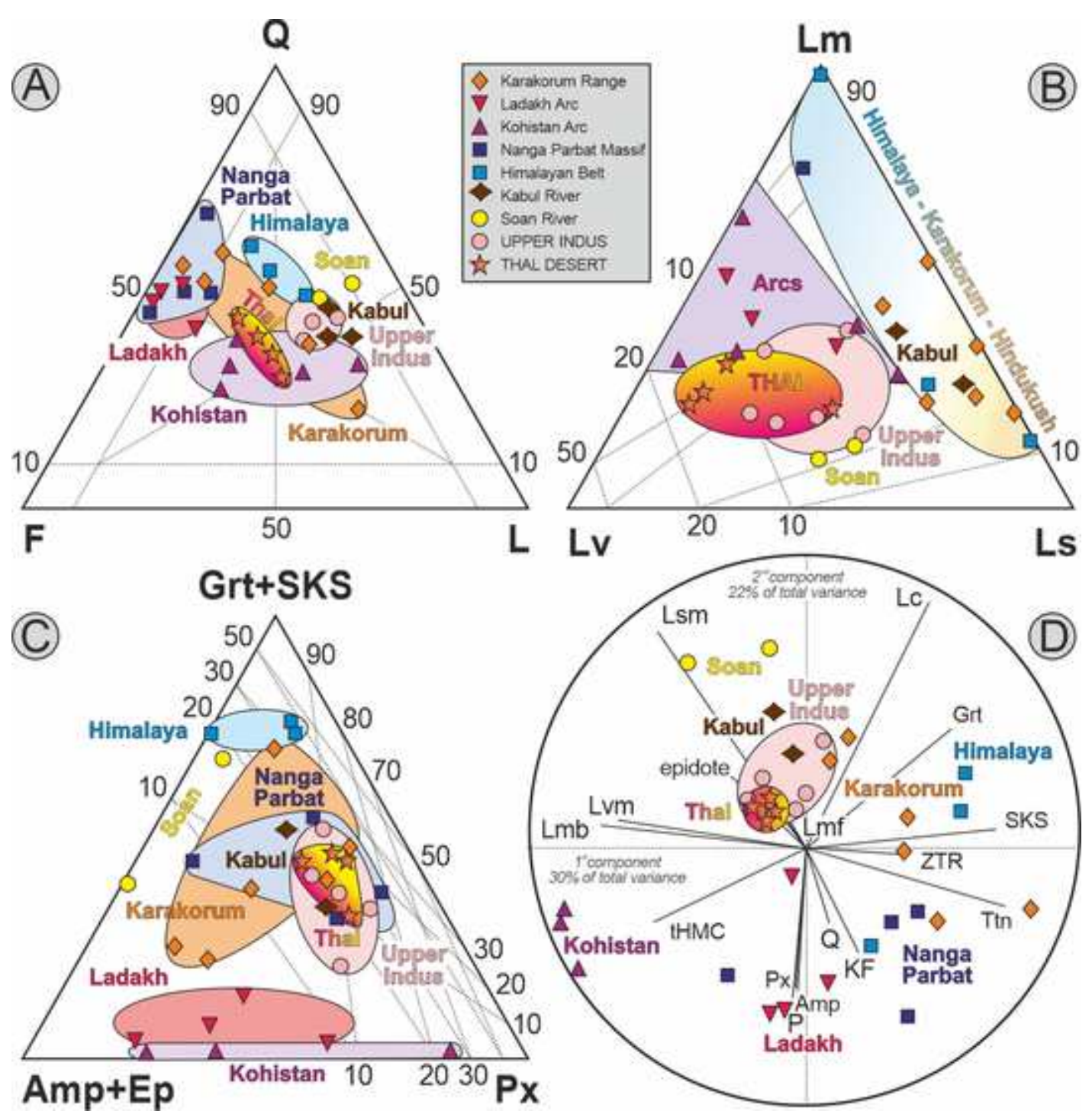
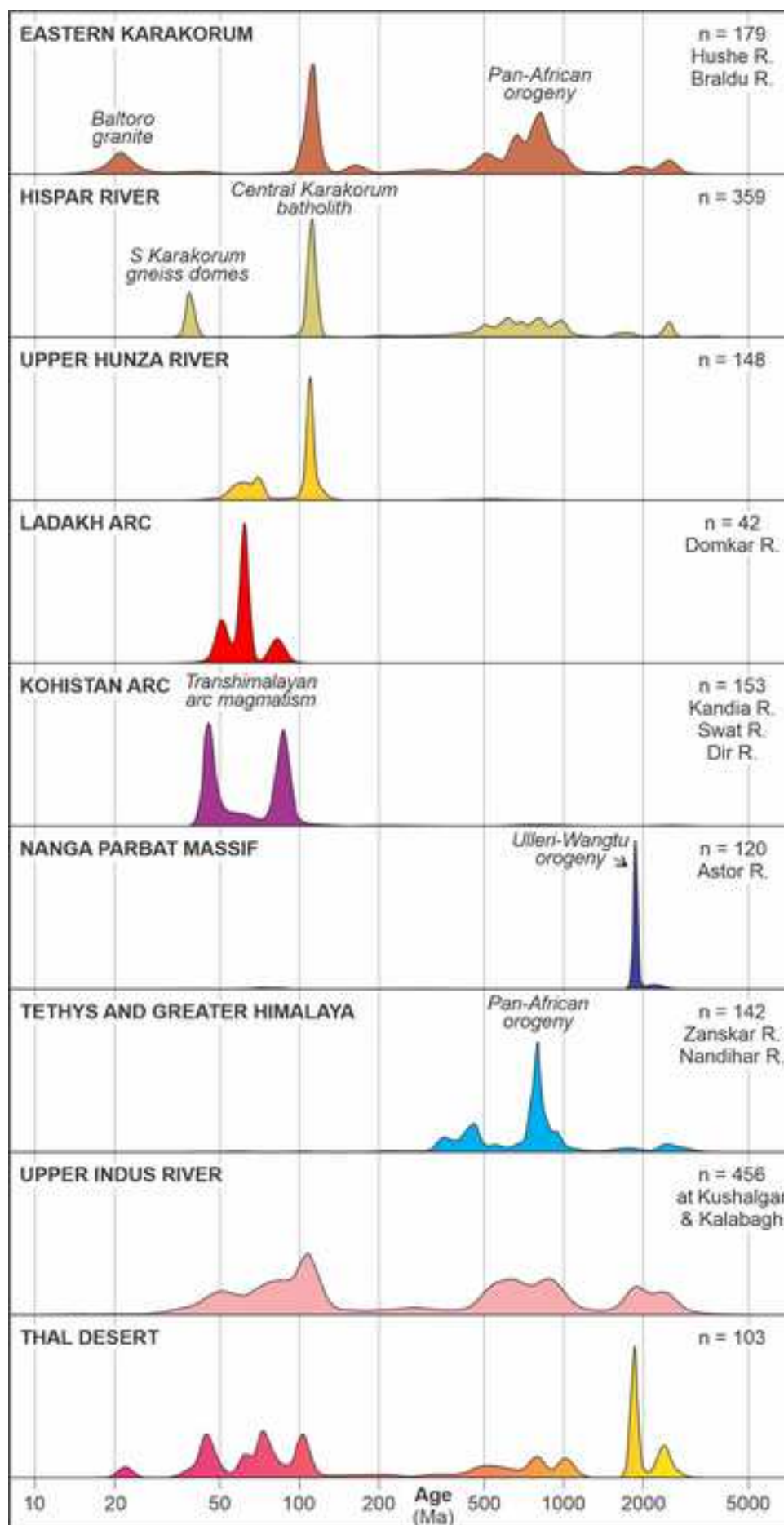




Figure 5

[Click here to access/download;Figure;Figure 5 Thal Review DZ.jpg](#)



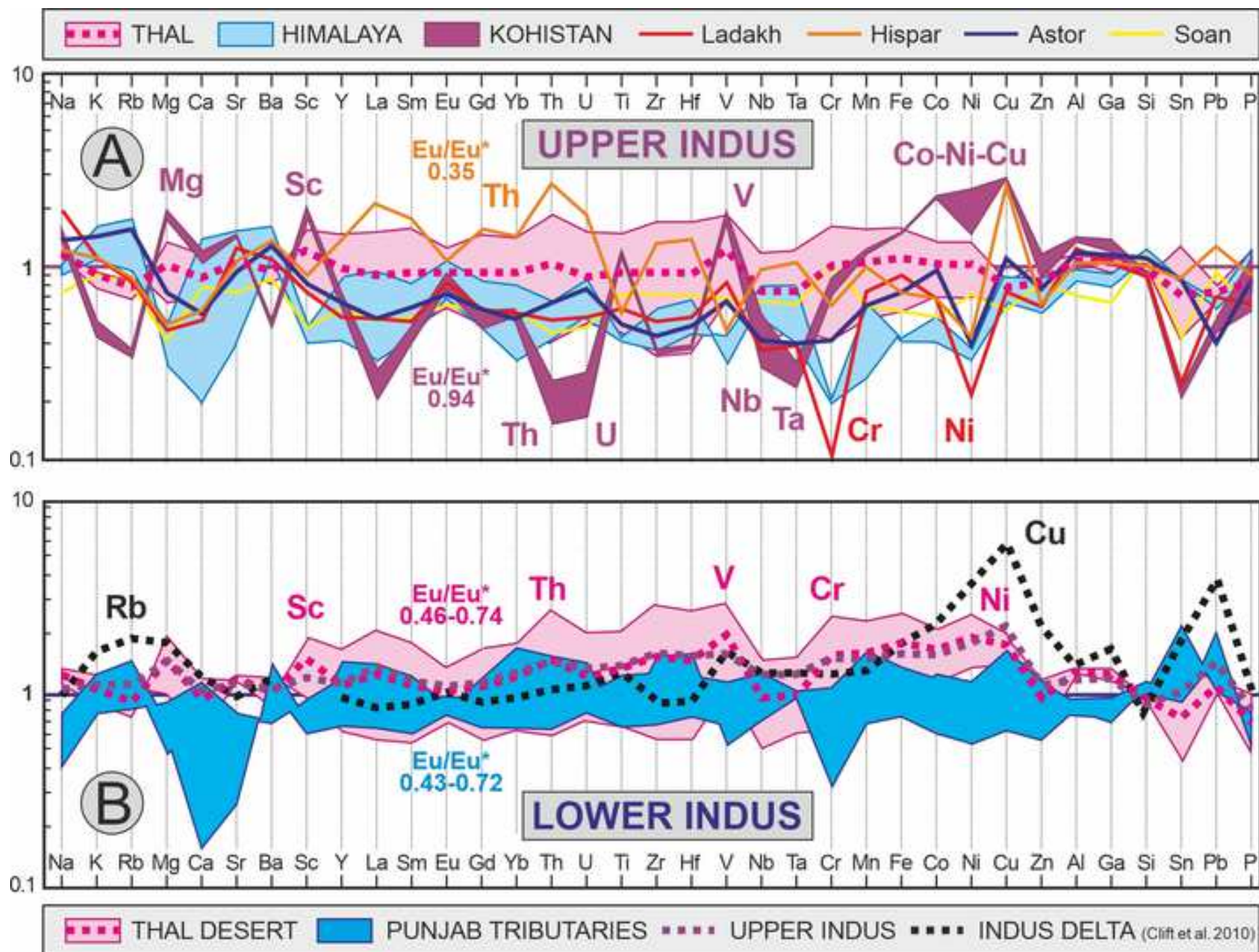


Figure 7

[Click here to access/download;Figure;Figure 7 Thal Review MinerCHI .jpg](#)

